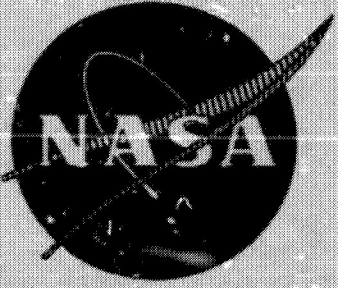


(NASA-CR-120803) SINGLE-STAGE EXPERIMENTAL
EVALUATION OF TANDEM-AIRFOIL ROTOR AND
STATOR BLADING FOR COMPRESSORS. PART 1:
J.A. Brent, et al (Pratt and Whitney
Aircraft) Jun. 1972 118 p

N72-26689 3

Unclas
31374

CSC 21E G3/28



SINGLE-STAGE EXPERIMENTAL EVALUATION OF TANDEM-AIRFOIL ROTOR AND STATOR BLADING FOR COMPRESSORS

PART I - ANALYSIS AND DESIGN OF STAGES A, B, AND C

by J. A. Brent, J. G. Cheatham, and A. W. Nilsen

PRATT & WHITNEY AIRCRAFT
DIVISION OF UNITED AIRCRAFT CORPORATION
FLORIDA RESEARCH AND DEVELOPMENT CENTER

Prepared for
NATIONAL AERONAUTICS AND SPACE ADMINISTRATION

NASA Lewis Research Center
Contract NAS3-11158



1. Report No. NASA CR-120803	2. Government Accession No.	3. Recipient's Catalog No.	
4. Title and Subtitle SINGLE-STAGE EXPERIMENTAL EVALUATION OF TANDEM-AIRFOIL ROTOR AND STATOR BLADING FOR COMPRESSORS, PART 1 - ANALYSIS AND DESIGN OF STAGES A, B, AND C.		5. Report Date June 1972	
		6. Performing Organization Code	
7. Author(s) J. A. Brent, J. G. Cheatham, and A. W. Nilsen		8. Performing Organization Report No. PWA FR-4667	
9. Performing Organization Name and Address Pratt & Whitney Aircraft Division of United Aircraft Corporation Florida Research and Development Center West Palm Beach, Florida 33402		10. Work Unit No.	
		11. Contract or Grant No. NAS3-11158	
12. Sponsoring Agency Name and Address National Aeronautics and Space Administration Washington, D. C. 20546		13. Type of Report and Period Covered Contractor Report	
		14. Sponsoring Agency Code	
15. Supplementary Notes Project Manager, Everett E. Bailey, Fluid System Components Division, NASA-Lewis Research Center Cleveland, Ohio 44135			
16. Abstract A conventional rotor and stator, two dual-airfoil tandem rotors, and one dual-airfoil tandem stator were designed. The two tandem rotors were each designed with different percentages of the overall lift produced by the front airfoil. Velocity diagrams and blade leading and trailing edge metal angles selected for the conventional rotor and stator blading were used in the design of the tandem blading. Rotor inlet hub/tip ratio was 0.8. Design values of rotor tip velocity and stage pressure ratio were 757 ft/sec and 1.30, respectively.			
17. Key Words (Suggested by Author(s)) Tandem Blading Compressor		18. Distribution Statement Unclassified - unlimited	
19. Security Classif. (of this report) Unclassified	20. Security Classif. (of this page) Unclassified	21. No. of Pages 118	22. Price* \$3.00

* For sale by the National Technical Information Service, Springfield, Virginia 22151

PRECEDING PAGE BLANK NOT FILLED

CONTENTS

	PAGE
ILLUSTRATIONS	iv
TABLES	vii
SUMMARY	1
INTRODUCTION	1
DESIGN VECTOR DIAGRAMS	2
AIRFOIL GEOMETRY SELECTION	6
Stage A	6
Tandem-Blade Stages B and C	9
Step 1	10
Step 2	11
MECHANICAL DESIGN	16
Rotor Steady-State Stress Analysis	16
Rotor A	16
Rotor B and Rotor C	16
Rotor Vibratory Analysis	16
Rotor A	16
Rotor B and Rotor C	17
Rotor Flutter Analysis	17
Rotor A	17
Rotor B and Rotor C	18
Rotor Attachment	19
Rotor Disk and Carrier	19
Stator Steady-State Stress Analysis	19
Stator Vibratory Analysis	21
Stator Flutter Analysis	21
Stator Attachment	22
APPENDIX A - Definition of Symbols and Design Variables	103
APPENDIX B - References	107

ILLUSTRATIONS

FIGURE		PAGE
1	Rotor Loss Parameter vs Diffusion Factor, 10% Span From Tip	23
2	Rotor Loss Parameter vs Diffusion Factor, 50% Span.	24
3	Rotor Loss Parameter vs Diffusion Factor, 90% Span From Tip	25
4	Stator Loss Parameter vs Diffusion Factor, 10% Span From Tip	26
5	Stator Loss Parameter vs Diffusion Factor, 50% Span.	27
6	Stator Loss Parameter vs Diffusion Factor, 90% Span From Tip	28
7	Design Flowpath Dimensions for Stages A, B, and C . . .	29
8	Rotor and Stator Loading Distributions	30
9	Rotor and Stator Loss Profile	31
10	Rotor and Stator Exit Pressure Profile	32
11	Rotor Incidence and Deviation Angle	33
12	Rotor Camber Angle	34
13	Stator Incidence and Deviation Angle	35
14	Stator Camber Angle.	36
15	Rotor Inlet Metal Angle Comparison	37
16	Rotor Exit Metal Angle Comparison	38
17	Stator Inlet Metal Angle Comparison	39
18	Stator Exit Metal Angle Comparison	40
19	Rotor A Blade Surface Velocities, 5% Span From Tip . . .	41
20	Rotor A Blade Surface Velocities, 50% Span	42
21	Rotor A Blade Surface Velocities, 95% Span From Tip . .	43
22	Stator A Vane Surface Velocities, 5% Span From Tip . . .	44
23	Stator A Vane Surface Velocities, 50% Span	45
24	Stator A Vane Surface Velocities, 95% Span From Tip . .	46
25	Tandem Airfoil Geometry, Circular-Arc Airfoils	47
26	Tandem Rotor Front Airfoil Meanline Analysis	48
27	Rotor B Camber Angle Distributions	49
28	Rotor C Camber Angle Distributions	50
29	Stator B Front Airfoil Loading Split	51

ILLUSTRATIONS (Continued)

FIGURE		PAGE
30	Stator B Camber Angle Distribution	52
31	Rotor B Static Pressure Coefficient, 5% Span From Tip	53
32	Rotor B Blade Surface Velocities, 5% Span From Tip . .	54
33	Rotor B Static Pressure Coefficient, 25% Span From Tip	55
34	Rotor B Blade Surface Velocities, 25% Span From Tip .	56
35	Rotor B Static Pressure Coefficient, 50% Span	57
36	Rotor B Blade Surface Velocities, 50% Span	58
37	Rotor B Static Pressure Coefficient, 75% Span From Tip	59
38	Rotor B Blade Surface Velocities, 75% Span From Tip	60
39	Rotor B Static Pressure Coefficient, 95% Span From Tip	61
40	Rotor B Blade Surface Velocities, 95% Span From Tip	62
41	Rotor C Static Pressure Coefficient, 5% Span From Tip	63
42	Rotor C Blade Surface Velocities, 5% Span From Tip . .	64
43	Rotor C Static Pressure Coefficient, 25% Span From Tip	65
44	Rotor C Blade Surface Velocities, 25% Span From Tip .	66
45	Rotor C Static Pressure Coefficient, 50% Span	67
46	Rotor C Blade Surface Velocities, 50% Span	68
47	Rotor C Static Pressure Coefficient, 75% Span From Tip	69
48	Rotor C Blade Surface Velocities, 75% Span From Tip .	70
49	Rotor C Static Pressure Coefficient, 95% Span From Tip	71
50	Rotor C Blade Surface Velocities, 95% Span From Tip .	72
51	Stator B Static Pressure Coefficient, 5% Span From Tip	73
52	Stator B Vane Surface Velocities, 5% Span From Tip . .	74
53	Stator B Static Pressure Coefficient, 25% Span From Tip	75

ILLUSTRATIONS (Continued)

FIGURE		PAGE
54	Stator B Vane Surface Velocities, 25% Span From Tip	76
55	Stator B Static Pressure Coefficient, 50% Span	77
56	Stator B Vane Surface Velocities, 50% Span	78
57	Stator B Static Pressure Coefficient, 75% Span From Tip	79
58	Stator B Vane Surface Velocities, 75% Span From Tip	80
59	Stator B Static Pressure Coefficient, 95% Span From Tip	81
60	Stator B Vane Surface Velocities, 95% Span From Tip	82
61	Calculated Rotor A Stress Distribution	83
62	Graphic Description of Tandem Rotor Analytical Model	84
63	Calculated Rotor B Stress Distribution	85
64	Calculated Rotor C Stress Distribution	86
65	Rotor A Resonance Diagram for First Bending and First Torsional Mode Vibration	87
66	Rotor A Goodman Diagram.	88
67	Rotor B Resonance Diagram for First Bending and First Torsional Mode Vibration	89
68	Rotor C Resonance Diagram for First Bending and First Torsional Mode Vibration	90
69	Rotors B and C Goodman Diagram	91
70	Calculated Rotor A First Bending and First Torsional Mode Flutter Characteristics	92
71	Calculated Rotor B First Bending and First Torsional Mode Flutter Characteristics	93
72	Calculated Rotor C First Bending and First Torsional Mode Flutter Characteristics	94
73	Calculated Stator A Stress Distribution	95
74	Calculated Stator B Stress Distribution	96
75	Stator A Resonance Diagram for First Bending and First Torsional Mode Vibration	97
76	Stator B Resonance Diagram for First Bending and First Torsional Mode Vibration	98
77	Stator A Goodman Diagram	99

ILLUSTRATIONS (Continued)

FIGURE		PAGE
78	Stator B Goodman Diagram	100
79	Calculated Stator A First Torsional Mode Flutter Characteristics	101
80	Calculated Stator B First Torsional Mode Flutter Characteristics	102

TABLES

TABLE		PAGE
I	Design Guidelines	2
IIa	Rotor Vector Diagram Calculation Results	4
IIb	Stator Vector Diagram Calculation Results	5
III	Rotor and Stator A Airfoil Geometry Data	7
IV	Velocity Ratios (V_{max}/V_{te})	8
V	Design Requirements for Rotor B, Stator B, and Rotor C	10
VI	Tandem Airfoil Geometry Data	14
VII	Tandem Airfoil Design Summary	15
VIII	Blade Attachment Stress	20
IX	Disk and Carrier Stress	21

SUMMARY

A rotor and stator having conventional blading, and two rotors and a stator having tandem blading (comprised of two airfoils in tandem), were designed for a comparative experimental evaluation in an 0.8 hub/tip ratio single-stage compressor. Velocity diagrams and blade leading and trailing edge metal angles selected for the conventional rotor and stator blading were used in the design of the tandem blading.

The tandem-blade rotors differed by the loading split between the two airfoils in tandem. Loading was defined as the tangential lift produced by the airfoil. Therefore, a 20%-80% loading split indicated that 20% of the overall tangential lift would be produced by the front airfoil. One rotor was designed with a 20%-80% loading split, and the other rotor was designed with a 50%-50% loading split. The tandem-blade stator, intended for use behind each of the tandem-blade rotors, was designed with a 20%-80% loading split.

The rotors were designed to produce a pressure ratio of 1.32 at a rotor tip velocity of 757 ft/sec. The design stage pressure ratio was 1.30. The predicted rotor and stage adiabatic efficiencies were 90.8% and 85.4%, respectively.

Stress analyses were performed for the selected blading. These included analysis of blade attachment and disk stresses, vibratory stresses, and flutter. Materials that would provide adequate stress margins were selected for blade fabrication.

INTRODUCTION

Advanced aircraft turbojet propulsion systems will require lightweight, highly loaded axial flow compressors capable of achieving high efficiency over a wide range of operating conditions. Axial flow blower experience has indicated that tandem blading can be successfully employed to extend the efficient operating range of compressors. In 1955, H. F. Sheets (Reference 1) reported excellent efficiencies for a highly loaded axial flow blower comprised of a tandem-blade rotor. More recently, favorable results were reported by H. Linnemann (Reference 2) based on a series of axial flow blower tests involving both tandem-blade rotors and stators. The results for the tandem blading indicated a better efficiency at a higher pressure ratio than that achieved with equivalent conventional blading.

In principle, tandem blading offers improved performance over conventional blading by distributing the overall blade row aerodynamic loading between the airfoils in tandem. The front airfoil may also provide control of the inlet air angle to the rear airfoil at off-design conditions, which should reduce the overall total pressure loss and possibly delay wall stall.

The first objective of this program is to investigate the potential of tandem blading for extending the loading limit and stable operating range of a stage representative of a middle stage of an advanced high pressure compressor. The second objective is to determine the effect, if any, of loading split on the performance of tandem blading. The aerodynamic and mechanical design of a

conventional rotor and stator, two dual-airfoil tandem rotors with differing loading splits, and a dual-airfoil tandem stator are the subjects of this report. The conventional single airfoil rotor and stator have been designated Rotor A and Stator A. One tandem-blade rotor with decreased loading on the front airfoil and increased loading on the rear airfoil has been designated Rotor B, and the other tandem-blade rotor with equal loading on each airfoil has been designated Rotor C. The tandem-blade stator, intended for use behind each of the tandem-blade rotors, has been designated Stator B and is designed for decreased loading on the front airfoil and increased loading on the rear airfoil.

DESIGN VECTOR DIAGRAMS

The selection of the design vector diagrams was accomplished within the range of the design guidelines given in table I.

Table I. Design Guidelines

Rotor Tip Diameter	30 in. (minimum)
Hub-Tip Ratio	0.7 to 0.8
Rotor Tip Speed	800 fps (maximum)
Rotor Tip Diffusion Factor	Less than 0.55
Rotor Tip Solidity	1.4 to 1.5
Stator Hub Diffusion Factor	Less than 0.60
Stator Hub Solidity	1.5 or greater

In addition to the guidelines specified in table I, the following criteria were specified for the design:

1. No inlet guide vanes (axial inlet flow)
2. Constant rotor exit total pressure
3. Axial stator discharge flow
4. Common flowpath geometries for all stages
5. Double circular arc blade sections.

To ensure a valid comparison between the conventional Stage A and the tandem-blade stages, the vector diagrams selected for Rotor and Stator A were used to design the tandem blading.

The initial phase of the design was the correlation of loss data from NASA-sponsored programs (References 3 to 10). Loss parameter and diffusion factor data for rotors and stators were plotted for three span locations (10, 50, and 90% span). Although the data from References 3 through 10 are for Series 65 blade sections, the data presented in Reference 11 indicate that a single correlation of loss parameter vs diffusion factor can be used for both Series 65 and double-circular-arc blade sections. Minimum loss data were used whenever a minimum value was clearly defined. Where a minimum loss was not clearly defined, the point corresponding to the midpoint of incidence angles tested was selected.

A design curve was selected to represent the data at each percent span. Cross-plots were made of loss parameter vs percent span at constant diffusion factor values of 0.4, 0.5, and 0.6 to check the spanwise loss gradient at constant diffusion factor. The selected design loss curves are shown in figures 1 through 6. The two-dimensional cascade data from figure 149 of Reference 11 and the range of compressor data shown in figure 192 of Reference 11 are shown for comparison with the selected loss curves.

The vector diagrams were selected by means of an iteration using an axisymmetric flow field calculation and the loss correlations shown in figures 1 through 6. The calculation procedure solved the continuity, energy, and radial equilibrium equations, which included the effects of streamline curvature and radial gradients of enthalpy and entropy.

The flowpath used for this investigation is shown in figure 7. The flowpath selection was governed by existing hardware. For the design vector diagram calculations, blockage allowances of 2%, 5%, and 5% of local annulus area were assumed at the rotor inlet, rotor exit, and stator exit, respectively, to account for boundary layer growth on the flowpath walls. A rotor tip inlet Mach number of 0.8 and a specific flow of 33 lb/sec-ft² were selected to be generally representative of current design practice for compressor middle stages. A summary of the vector diagram calculation results along the design streamlines, which were selected to pass through 5, 10, 15, 30, 50, 70, 85, 90, and 95% span at the rotor exit instrumentation station, is presented in tables IIa and IIb for the rotors and stators, respectively. The diffusion factor, loss coefficient, and exit total pressure distributions are also presented in figures 8 through 10. The predicted rotor pressure ratio and adiabatic efficiency are 1.32 and 90.8%, respectively, at a design rotor tip speed of 757 ft/sec. The predicted pressure ratio and efficiency for the stage at design rotor speed are 1.30 and 85.4%, respectively.

Table IIa. Rotor Vector Diagram Calculation Results

Equivalent Rotor Speed = 4210 rpm		Equivalent Weight Flow = 110 lb/sec												
Percent Span From Tip		V_{le}	V_{zle}	$V_{\theta le}$	β'_{le}	U_{le}	V'_{te}	V_{zte}	$V_{\theta te}$	β'_{te}	U_{te}	α		
Leading Edge	Trailing Edge	(ft/sec)	(ft/sec)	(ft/sec)	(deg)	(ft/sec)	(ft/sec)	(ft/sec)	(ft/sec)	(deg)	(ft/sec)	(deg)		
Hub	96.5	778.0	484.5	608.8	51.49	608.8	483.8	463.4	138.9	16.69	610.5	1.08		
	91.5	784.0	484.4	616.5	51.84	616.5	492.2	467.0	155.5	18.42	617.6	0.50		
	86.4	790.1	484.3	624.2	52.19	624.2	500.2	469.8	171.6	20.07	624.7	-0.08		
	70.9	808.5	483.8	647.8	53.24	647.8	523.3	476.7	215.9	24.36	645.9	-1.78		
	50.0	833.5	482.6	679.6	54.62	679.6	548.2	486.2	264.3	28.83	674.2	-3.95		
	29.1	858.7	480.8	711.5	55.95	711.5	562.1	474.0	307.2	32.53	702.6	-6.03		
	13.6	877.4	479.0	735.1	56.91	735.1	566.1	463.1	325.6	35.11	723.8	-7.52		
	8.5	883.5	478.4	742.8	57.22	742.8	566.0	458.6	331.8	35.88	730.9	-8.00		
Tip	3.5	889.6	477.7	750.5	57.52	750.5	565.0	453.8	336.6	36.56	738.0	-8.48		
Percent Span from Tip														
Leading Edge	Trailing Edge	M'_{le}	D	$\bar{\omega}'$	Loss Parameter	P_{le}	T_{le}	P_{te}	T_{te}					
Hub	95.0	0.7102	0.5533	0.11341	0.03154	14.694	518.7	19.368	566.63					
	90.0	0.7152	0.5447	0.10314	0.02876	14.694	518.7	19.369	566.20					
	85.0	0.7212	0.5370	0.09446	0.02637	14.694	518.7	19.366	565.81					
	70.9	0.7380	0.5171	0.07363	0.02067	14.694	518.7	19.367	565.94					
	50.0	0.7608	0.5028	0.06131	0.01732	14.694	518.7	19.395	564.71					
	29.1	0.7836	0.5057	0.07348	0.02085	14.694	518.7	19.395	565.53					
	13.6	0.8005	0.5167	0.09534	0.02713	14.694	518.7	19.366	566.69					
	8.5	0.8061	0.5224	0.10505	0.02988	14.694	518.7	19.363	567.28					
Tip	3.5	0.8116	0.5296	0.11647	0.03318	14.694	518.7	19.363	568.04					

Note: $\beta_{le} = 0$ and is constant with radius.

Table IIb. Stator Vector Diagram Calculation Results

Equivalent Weight Flow = 110 lb/sec											
Equivalent Rotor Speed = 4210 rpm											
Percent Span From Tip											
	Leading Edge	Trailing Edge	V_{le} (ft/sec)	V_{zle} (ft/sec)	$V\theta_{le}$ (ft/sec)	β_{le} (deg)	V_{te} (ft/sec)	V_{zte} ft/sec	$V\theta_{te}$ (ft/sec)	β_{te} (deg)	α (deg)
Hub	95.0	95.0	667.2	471.9	471.7	44.99	477.0	480.0	0.0	0.0	-0.05
	90.0	90.1	663.0	475.4	462.2	44.20	481.9	481.9	0.0	0.0	-0.10
	85.0	85.2	658.9	478.2	453.3	43.47	483.6	483.6	0.0	0.0	-0.15
	70.0	70.1	648.6	485.1	430.5	41.58	488.8	488.8	0.0	0.0	-0.28
	50.0	50.0	638.6	489.2	410.5	40.00	494.4	494.4	0.0	0.0	-0.47
	30.0	29.8	628.6	483.9	401.1	39.66	494.7	494.6	0.0	0.0	-0.63
	15.0	14.8	619.8	474.1	399.2	40.09	492.2	492.0	0.0	0.0	-0.77
	10.0	9.9	617.4	470.1	400.2	40.40	491.4	491.4	0.0	0.0	-0.80
Tip	5.0	4.9	615.6	465.8	402.5	40.84	491.2	491.2	0.0	0.0	-0.85

Percent Span from Tip										
	Leading Edge	Trailing Edge	M_{le}	D	$\bar{\omega}$	Loss Parameter	P_{te} (psia)			
Hub	95.0	95.0	0.5915	0.5183	0.09619	0.03242	18.975			
	90.0	90.1	0.5878	0.5106	0.09171	0.03125	18.999			
	85.0	85.2	0.5840	0.5035	0.08721	0.03004	19.017			
	70.0	70.1	0.5747	0.4840	0.07636	0.02717	19.070			
	50.0	50.0	0.5655	0.4672	0.07100	0.02634	19.126			
	30.0	29.8	0.5556	0.4649	0.07570	0.02926	19.116			
	15.0	14.8	0.5468	0.4695	0.08253	0.03276	19.072			
	10.0	9.9	0.5442	0.4722	0.08632	0.03457	19.057			
Tip	5.0	4.9	0.5422	0.4755	0.08920	0.03603	19.050			

AIRFOIL GEOMETRY SELECTION

Stage A

Double circular-arc constant chord length airfoils were selected for the rotor and stator. A design thickness-to-chord ratio distribution was selected consistent with current design practice, and the rotor tip and stator hub chord lengths, number of blades, and number of vanes were selected to satisfy the solidity requirements of table I.

Airfoil camber, incidence, and deviation angles were calculated along design streamlines for the rotor and stator using equations 286, 287, and 288 presented in Reference 11, except that the three-dimensional corrections for incidence and deviation angles were omitted. The double circular arc airfoil sections selected for the rotor and stator were positioned on planes tangent to conic surfaces, which approximated design streamlines of revolution. The rotor and stator geometry on planes tangent to these conic surfaces is summarized in table III. The resultant radial distributions of airfoil camber, incidence, and deviation angles are shown in figures 11 through 14. For manufacturing purposes, the selected airfoil sections were redefined on planes tangent to cylindrical surfaces by simply rotating the sections about an axis. This axis was defined by the intersection of two planes: one plane tangent to the cylindrical surface and the second plane normal to the compressor centerline. This second plane was located midway between the blade row leading and trailing edges. The rotated airfoil sections for Rotor A were further positioned so that their centers of gravity were on a radial line. The rotated airfoil sections for Stator A were further positioned so that the center points of the trailing edge radii were on a radial line. The simplified method of rotating the selected airfoil sections onto planes tangent to cylindrical surfaces results in blade geometry that is slightly different than the design intent. However, because the cone angles are small (see α in table II), it was concluded that the geometry differences would be small. A comparison of the radial distributions of the design inlet and exit airfoil angles and the airfoil angle distributions that resulted after the airfoil sections were rotated are shown for the rotors and stators in figures 15 through 18. As shown in figures 15 through 18, the maximum difference between the actual design airfoil angles and the airfoil angles that resulted when the airfoil sections were rotated onto planes tangent to cylindrical surfaces was less than 1 deg. Since 1 deg is of the same order of magnitude as the manufacturing tolerance for the required airfoils, the airfoil geometry defined using the simplified technique was considered adequate. However, prior to accepting the resulting airfoil geometry, the ratio of maximum suction surface velocity to exit velocity was estimated for the hub, mean, and tip sections of the rotor and stator to ensure that they were not significantly greater than 2.0. According to the results presented in Reference 12, a velocity ratio in excess of 2.0 may lead to a possible rapid increase in the airfoil boundary layer momentum thickness with a corresponding increase in loss.

The surface velocity distributions were estimated for the rotated airfoil sections assuming two-dimensional, incompressible, inviscid potential flow. The potential flow solution involved a computer program that calculated the velocity field of an infinite cascade as governed by Laplace's equation:

$$\nabla^2 \phi = 0$$

Table III. Rotor and Stator A Airfoil Geometry Data*

ROTOR A												
Airfoil: Circular Arc		No. of Blades: 70		Chord Length: 2.57 inches								
Percent Span From Tip		Leading Edge	Trailing Edge	κ_{le} (deg)	κ_{te} (deg)	ϕ (deg)	γ° (deg)	σ	t/c	i_c (deg)	δ° (deg)	
Hub	96.5	95.0	51.84	7.75	44.09	29.708	1.7241	0.0783	-0.354	8.937		
	91.5	90.0	52.28	9.30	42.98	30.705	1.7036	0.0763	-0.439	9.121		
	86.4	85.0	52.69	10.92	41.77	31.724	1.6835	0.0743	-0.499	9.149		
	70.9	70.0	54.06	15.70	38.36	34.826	1.6250	0.0682	-0.813	8.665		
	50.0	50.0	56.05	20.67	35.39	38.359	1.5528	0.0600	-1.430	8.164		
	29.1	30.0	58.03	24.82	33.22	41.443	1.4868	0.0518	-2.078	7.709		
	13.6	15.0	59.40	27.48	31.92	43.446	1.4409	0.0457	-2.485	7.635		
	8.5	10.0	59.83	28.05	31.77	43.960	1.4265	0.0437	-2.606	7.831		
Tip	3.5	5.0	60.60	28.78	31.82	44.696	1.4122	0.0417	-3.076	7.778		

STATOR A												
Airfoil: Circular Arc		No. of Vanes: 66		Chord Length: 2.35 inches								
Percent Span From Tip		Leading Edge	Trailing Edge	κ_{le} (deg)	κ_{te} (deg)	ϕ (deg)	γ° (deg)	σ	t/c	i_c (deg)	δ° (deg)	
Hub	95.0	95.0	46.97	-13.03	60.00	16.972	1.4850	0.09	-1.982	13.031		
	90.0	90.1	46.20	-12.85	59.06	16.768	1.4689	0.09	-2.003	12.854		
	85.0	85.2	45.47	-12.73	58.20	16.375	1.4531	0.09	-2.001	12.734		
	70.0	70.1	43.67	-12.33	56.00	15.673	1.4073	0.09	-2.086	12.354		
	50.0	50.0	42.23	-12.12	54.35	15.055	1.3504	0.09	-2.228	12.120		
	30.0	29.8	42.35	-12.71	55.06	14.825	1.2980	0.09	-2.697	12.708		
	15.0	14.8	43.30	-13.51	56.81	14.902	1.2614	0.09	-3.211	13.510		
	10.0	9.9	43.85	-13.81	57.66	15.027	1.2497	0.09	-3.450	13.808		
Tip	5.0	4.9	44.45	-14.15	58.61	15.153	1.2382	0.09	-3.619	14.152		

*Information included in Table III is defined on planes tangent to the conic surfaces which approximate design streamlines of revolution.

where ϕ is the velocity potential. Solutions were obtained for zero angle of attack, 90 deg angle of attack, and circulatory flow and the results superimposed in such a way that the correct angle of attack was obtained and the Kutta condition satisfied. The method of solution, described in Reference 13, utilizes a distribution of sources on the airfoil surface and solves a set of linear algebraic equations for the source distribution that forces the total velocity normal to the airfoil surface to be zero. The total velocity is the sum of two velocities: the onset velocity, defined as the velocity field in which the body is immersed and the disturbance velocity, defined as the velocity field caused by the source distribution. The velocity distributions thus obtained were corrected for compressibility by means of the Karman-Tsien equation, and the results are shown in figures 19 through 24 for the hub, mean, and tip sections of the rotor and stator.

As shown in figures 19 through 24, the mean exit velocity for the potential flow calculations is lower than the exit velocity for the vector diagram calculations. This difference in the exit velocities results because the potential flow solution did not consider (1) the change in the streamtube radius through the blade row, (2) the convergence in the streamtube area through the blade row, and (3) the small differences in incidence and deviation angle resulting from the rotation of the airfoil sections (as described above). The radius change and streamtube convergence are associated with the flowpath shape and the blade total pressure losses. Prior to calculating the ratio of the maximum suction surface velocity to exit velocity, the maximum velocity on the suction surface was increased to reflect the convergence in the streamtube area through the blade row. The amount of increase was the local difference between linear distributions of velocity from the inlet value to the exit values obtained from (1) the vector diagram calculations and (2) the potential flow calculations, as illustrated in figures 19 through 24. The local correction applied as described above is indicated as LC on each figure. The velocity ratio of interest was the corrected maximum suction surface velocity divided by the exit velocity obtained in the vector diagram calculations. Velocity ratios calculated in this manner were compared with the results obtained for the same blade geometries using the NASA compressible flow solution that assumes that the streamtube area converges linearly through the blade row (Reference 14); very good agreement was obtained. The aforementioned technique for correcting the maximum suction surface velocities for compressibility and streamtube convergence was therefore considered valid. The resulting velocity ratios for the rotor and stator are shown in table IV.

Table IV. Velocity Ratios (V_{max}/V_{te})

Percent Span From Tip	Rotor A	Stator A
5	1.96	1.77
50	1.94	1.79
95	2.10	1.88

The velocity ratio slightly in excess of 2.0 for Rotor A at 95% span is not considered detrimental to the stage design since a rotor diffusion factor level of 0.5533, shown in table IIa for 95% span, is considered reasonable for an advanced compressor design. Therefore, the rotor and stator airfoil geometry that resulted by rotating airfoil sections defined on planes tangent to the conic (table III) to planes tangent to a cylindrical surface and the associated radial distributions of incidence and deviation angles were considered satisfactory.

Tandem-Blade Stages B and C

In keeping with the program objectives, airfoil geometry was selected for the first tandem rotor and stator, designated Rotor B and Stator B, so that the front airfoil would be more lightly loaded than the rear airfoil. For the second tandem rotor, designated Rotor C, airfoil geometry was selected so that an approximately equal distribution of loading occurred between the front and rear airfoils. It was decided that a second tandem stator would not be designed, but that tandem Rotor C would be tested with Stator B. The airfoil geometry for each tandem blade row was selected to satisfy the overall vector diagram requirements given in table II.

To ensure interchangeability with Stage A, the radial distributions of overall axial chord (figure 25) were maintained equal to the distribution selected for the Stage A blading. To minimize the number of variables to be investigated in selecting tandem airfoil geometry, the individual airfoil maximum thickness-to-chord ratio for each of the airfoils of the tandem blading was also maintained equal to the value selected for the Stage A blading. Double circular-arc sections were selected for both airfoils of the tandem blading to be consistent with an in-house analytical study conducted for NASA-Lewis Research Center (Reference 15). The individual chords for the tandem blades were arbitrarily set equal and the individual airfoils were defined on planes tangent to a cylindrical surface and positioned according to the following criteria.

1. The leading edge airfoil angle of the front airfoil and the trailing edge airfoil angle for the rear airfoil were maintained equal to the leading and trailing edge airfoil angles, respectively, selected for Stage A.
2. The passage width between the blades was maintained at approximately 10% of the front airfoil chord. This selection was based on the results of a NASA in-house analytical study of tandem blading described in Reference 15.
3. Zero axial overlap of the front and rear airfoils was maintained for ease of fabrication; however, this selection is consistent with the cascade results presented in Reference 16 and the rotor results in Reference 2, and yielded a blade passage area ratio in the same range indicated as favorable in the NASA studies (Reference 15).

For Rotors B and C, the tandem airfoil sections were stacked radially so that the centers of gravity of the combined sections were on a radial line. For Stator B, the airfoil sections were stacked radially so that the center points of the trailing edge radii of the rear airfoil were on a radial line.

The selection of the front and rear airfoil camber angles was accomplished in two steps. The first step involved an iterative process, using the potential flow calculation procedure described on pages 6 and 8, to select the front and rear airfoil camber angles that satisfied the loading split and maximum suction surface-to-exit velocity ratio requirements given in table V.

Table V. Design Requirements for Rotor B, Stator B, and Rotor C

Blade Row	Design Requirements
Rotor B	Maximum differential in loading between the front and rear airfoils without exceeding a rear airfoil suction surface maximum-to-exit velocity ratio of 1.9.
Stator B	Maximum differential in loading between the front and rear airfoils without exceeding a rear airfoil suction surface maximum-to-exit velocity ratio of 1.8.
Rotor C	Approximately an equal distribution of loading between the front and rear airfoils.

The second step involved checking the results of the potential flow analysis using the independent axisymmetric flow field calculation procedure discussed on page 3. This check was made to determine if the potential flow solution (which used a generalized compressibility correction and did not account for total pressure losses, streamtube radius changes, or streamtube convergence) accurately predicted the loading split between the two airfoils in tandem. A detailed description of the two steps used in the airfoil geometry selection procedure is included in the following paragraphs.

Step 1

The following iterative process was used during the first step of the design procedure to select the front and rear airfoil camber angles at 5, 25, 50, 75, and 95% span:

1. Initial values of camber angle were assumed for the front and rear airfoils. These camber angles were selected so that the passage between the blades would be slightly convergent (inlet-to-exit area ratio greater than one), thus avoiding undue velocity peaks or deceleration in the passage between the airfoils.

2. Blade surface pressure and velocity distributions were calculated by means of the technique described on pages 6 and 8.
3. The areas enclosed by surface pressure distributions were integrated to determine the loading (tangential lift) split between the two airfoils in tandem. The surface pressure distributions were corrected for compressibility; however, no corrections for streamtube radius changes or convergence through the blade row were applied.
4. The maximum suction surface-to-exit velocity ratio for each airfoil was calculated. The maximum suction surface velocity included the corrections for compressibility, streamtube convergence, etc., as discussed on page 8.
5. The loading split between the front and rear airfoils and the maximum suction surface-to-exit velocity ratio were compared to the design requirements given in table V.
6. If the design requirements were not satisfied, the camber angles were changed and the procedure repeated until the desired blade surface velocity ratio and loading split were obtained.

Step 2

The second step in the airfoil geometry selection procedure was to check the results of the potential flow analysis by using an independent axisymmetric flow field analysis similar to that used for the selection of the vector diagrams (page 3). As previously stated, this check was made to determine if the potential flow solution resulted in an accurate prediction of the loading split and therefore the energy input distribution through the blade row. The initial results of axisymmetric flow analysis showed a shift in the loading (relative to that calculated by the potential flow analysis) to the rear airfoil. In fact, the front airfoil of Rotor B had a pressure ratio of less than one and a diffusion factor of less than zero. This loading shift and reduced front airfoil loading were attributed to the acceleration (i.e., $V_{z_{te}}/V_{z_{le}} > 1.0$) of the flow through the front blade row that resulted from the combination of the reduced energy input and the wall convergence through the blade row. However, this analysis treated the front and rear airfoils as independent blade rows and neglected any effect that the pressure distribution around the rear airfoil might have on the front airfoil turning.

To obtain an understanding of the front and rear airfoil-to-airfoil interactions when accompanied by acceleration of the flow through the blade row, the axisymmetric flow calculation procedure was used to calculate (1) the ratio of the change in the meanline tangential velocity through the front airfoil to the total change in the meanline tangential velocity across the blade row and (2) the front airfoil pressure ratio as a function of front airfoil camber and deviation angle. During this analysis, the radial distribution of the front airfoil camber angle selected for Rotor B was maintained, and the level adjusted by a constant value across the entire span to provide the desired camber angle at midspan. Since the spanwise variation in front airfoil camber angle for Rotors B and C was less than 4 deg, camber distribution should have a very small effect on calculated change in meanline tangential velocity through the front airfoil, and

the results should be valid for both Rotors B and C. The camber angle for the rear airfoil was not varied during this analysis because the axisymmetric flow calculation procedure treats the front and rear airfoils as independent blade rows. If the small changes in streamtube radius through the blade row are neglected and the flow is assumed to be steady, Newton's law of motion can be used to show that the ratio of change in tangential velocity through the front airfoil to the total change in tangential velocity is equal to the percentage of overall tangential lift produced by the front airfoil. The change in tangential velocity across the tandem blade rows was assumed equal to the change in tangential velocity across Rotor A because all three rotors were designed to produce identical inlet and exit vector diagrams. The results of the study to estimate front and rear airfoil-to-airfoil interactions in terms of (1) percentage of overall tangential lift produced by the front airfoil and (2) front airfoil pressure ratio as functions of front airfoil camber angle for three values of percent cascade deviation angle are shown in figure 26.

The axisymmetric flow field analysis assuming 50% cascade deviation at midspan was chosen for selection of the final camber angles for the front airfoils of Rotors B and C. This technique was selected as it attempts to account for both front and rear airfoil-to-airfoil interaction and acceleration of the flow through the blade row. The potential flow analysis performed during step 1 of the airfoil selection process indicated that a 20%-80% loading split between the front and rear airfoil could be achieved for Rotor B without exceeding the velocity ratio requirements. A front camber angle of 5 deg was indicated for this analysis. Using a 20%-80% loading split and 50% cascade deviation, the axisymmetric flow analysis indicates 6.6 deg of camber required in the front airfoil at the meanline. Thus, the camber angle of Rotor B was increased 1.6 deg across the entire span. The rear airfoil camber angle for Rotor B was decreased so that the passage between the blades would be slightly convergent when the two airfoils were positioned with a zero axial overlap and a interblade passage width of approximately 10% of front airfoil chord. The leading edge airfoil angle for the front airfoil and the trailing edge airfoil angle for the rear airfoil were not changed since these values were initially selected to be equal to the leading and trailing edge airfoil angles, respectively, of Rotor A. The final Rotor B front and rear airfoil camber distributions and the camber distributions selected from the potential flow analysis are compared in figure 27.

The potential flow and axisymmetric analysis indicated 12.0 deg and 12.5 deg, respectively, for Rotor C front airfoil camber angle. Since the 0.5 deg difference is within the accuracy of the calculation techniques, the camber angles for Rotor C were not changed. The Rotor C front and rear airfoil camber angle distributions are presented in figure 28.

As a result of the axisymmetric flow calculations for Rotor B, Stator B was also processed through the axisymmetric flow calculation procedure to determine a loading split based on the ratio of the change in the meanline tangential velocity through the front airfoil to the total change in the meanline tangential velocity across the blade row. The results of this analysis are presented in terms of the percentage of the overall tangential lift produced by the front airfoil vs percent cascade deviation angle for the front airfoil in figure 29. As indicated, if it is again assumed that the front airfoil deviation angle will be reduced by 50% because of the rear airfoil pressure distribution, the resulting loading split between the front and rear airfoils is 20%-80%. Although this

loading split is significantly different from the 30%-70% loading split calculated from the results of the potential flow analysis, the camber for Stator B was not changed since the primary design requirement for Stator B was to obtain the maximum differential in loading between the front and rear airfoils without exceeding a rear airfoil maximum suction surface-to-exit velocity ratio of 1.8. The stator B spanwise camber distribution is shown in figure 30.

The Rotor B, Rotor C, and Stator B airfoil geometries are summarized in table VI. The chord lengths calculated for the front and rear airfoils of Rotor B, Rotor C, and Stator B actually varied slightly from hub to tip. However, since the variation in chord length was less than 3% of the individual airfoil chord, the average value was selected and assumed not to vary with radius.

The loading splits, camber ratios, airfoil maximum suction surface-to-exit velocity ratios, blade passage overlaps, blade passage gaps, and blade passage convergences are given in table VII for the final selected tandem-airfoil configurations at 5, 25, 50, 75, and 95% span. The blade surface static pressure coefficient distributions and the corrected maximum suction surface velocities used to calculate loading splits and maximum suction surface-to-exit velocity ratios are shown in figures 31 through 60. The corrected maximum suction surface velocities shown on the appropriate figures were corrected using the technique described on page 8. Although this technique is not correct when the axial velocity does not vary linearly through the blade passage, the error associated with the nonlinearity in the axial velocity through Rotor B and Stator B is considered minimal since the maximum suction surface-to-exit velocity ratios for these blade rows would increase by less than 5% if it was assumed that all of the acceleration of the flow occurs through the front airfoil.

Since the tandem airfoil sections were originally defined on plane surfaces normal to a radial line, it was not necessary to redefine the surface coordinates for manufacturing purposes.

Table VI. Tandem Airfoil Geometry Data*

Percent Span From Tip**	Front Body				Rear Body			Front and Rear Bodies	
	ϕ (deg)	κ_{le} (deg)	κ_{te} (deg)	γ° (deg)	ϕ (deg)	κ_{le} (deg)	κ_{te} (deg)	γ° (deg)	σ t/c
Tandem Rotor B - Airfoils: Circular Arc									
5	8.6	60.60	51.99	56.29	26.50	55.28	28.78	42.03	0.7962 0.0417
25	7.3	58.49	51.18	54.83	29.25	55.13	25.88	40.50	0.8294 0.0498
50	6.6	56.05	49.47	52.77	33.50	54.17	20.67	37.42	0.8751 0.0600
75	6.6	53.64	47.04	50.34	37.00	51.14	14.14	32.64	0.9264 0.0701
95	8.6	51.84	43.25	47.55	37.50	45.25	7.75	26.50	0.9721 0.0783
Tandem Rotor C - Airfoils: Circular Arc									
5	13.0	60.60	47.59	54.51	25.00	53.78	28.78	41.93	0.7526 0.0417
25	12.0	58.48	46.48	52.48	23.80	49.68	25.88	37.78	0.7840 0.0498
50	12.0	56.05	44.07	50.07	26.00	46.67	20.67	33.67	0.8271 0.0600
75	13.3	53.64	40.34	46.99	30.50	44.64	14.14	29.39	0.8756 0.0701
95	15.0	51.84	36.85	44.35	35.00	42.75	7.75	25.25	0.9188 0.0783
Tandem Stator B - Airfoils: Circular Arc									
5	12.0	44.45	32.45	38.45	53.00	38.85	-14.15	12.35	0.6850 0.0900
25	10.6	42.67	32.07	37.73	50.80	37.87	-12.93	12.47	0.7113 0.0900
50	10.0	42.23	32.23	37.23	50.00	37.88	-12.12	12.88	0.7472 0.0900
75	10.6	44.27	33.67	38.97	50.80	38.42	-12.38	13.02	0.7867 0.0900
95	12.0	46.97	34.97	40.97	52.73	39.70	-13.03	13.23	0.8215 0.0900

*Information is defined on conical surfaces that approximate the design streamlines of revolution.

**Percent spans for rotors are at trailing edge, whereas the percent spans for the stator are at the leading edge.

Table VII. Tandem Airfoil Design Summary*

Percent Span From Tip**	Camber Ratio	Convergence (F)	Gap (G/C)	Overlap (L/C)	Loading Split (Potential Flow)		Velocity Ratio		
					Front	Rear	Front	Rear	
Tandem Rotor B - Loading Split***: 20%-80%									
5	3.08	1.01	0.098	0.151	36.2	63.8	1.156	1.755	
25	4.01	1.05	0.101	0.156	34.1	65.9	1.162	1.786	
50	5.08	1.06	0.099	0.145	32.1	67.9	1.176	1.791	
75	5.61	1.01	0.097	0.129	31.4	68.6	1.212	1.833	
95	4.36	1.00	0.100	0.114	35.7	64.3	1.221	1.859	
Tandem Rotor C - Loading Split***: 50%-50%									
5	1.92	1.09	0.100	0.147	50.2	49.8	1.385	1.586	
25	1.98	1.03	0.100	0.132	48.8	51.2	1.331	1.582	
50	2.17	1.01	0.102	0.124	49.0	51.0	1.326	1.598	
75	2.29	1.03	0.102	0.117	49.6	50.4	1.414	1.645	
95	2.33	1.06	0.101	0.105	50.0	50.0	1.467	1.699	
Tandem Rotor B - Loading Split***: 20%-80%									
5	4.42	1.06	0.094	0.083	33.3	66.7	1.238	1.828	
25	4.79	1.03	0.098	0.084	29.5	70.5	1.218	1.806	
50	5.00	1.05	0.101	0.082	29.7	70.3	1.212	1.808	
75	4.79	1.02	0.098	0.086	30.6	69.4	1.211	1.803	
95	4.42	1.04	0.097	0.091	32.1	67.9	1.248	1.830	

*Information is defined on conical surfaces that approximate the design streamlines of revolution.
 **Percent spans for rotors are at trailing edge, whereas the percent spans for the stator are at the leading edge.

***AFCC Meanline Analysis With 50% Reduction in Front Body Deviation

MECHANICAL DESIGN

Rotor Steady-State Stress Analysis

Rotor A

The stresses due to centrifugal loads and/or gas bending loads were calculated at thirteen radial locations for a Rotor A airfoil fabricated from AMS 5616 (stainless steel). The reduction of gas bending stress due to centrifugal load was considered and the resulting net gas bending stress and centrifugal tensile stress were added to yield the total blade stress at each radial location. The results of this analysis are presented in figure 61. The maximum stress for Rotor A was 14,200 psi at the trailing edge of the hub section. This calculated stress is well within the 0.2% yield strength of 110,000 psi for AMS 5616.

Rotor B and Rotor C

Preliminary analysis of the front and rear airfoil natural frequencies for Rotors B and C indicated that a bridge connecting the two airfoils in tandem was required to increase frequency and stiffness (thus reducing susceptibility to flutter, as will be discussed on page 18) and to ensure dimensional stability during operation. Rotors B and C, with a 0.030-in. thick interblade bridge at 30% span, were analyzed to determine airfoil and interblade bridge stress due to centrifugal and/or gas bending loads. To minimize centrifugal force stress, titanium (AMS 4973) was selected as the blade material in preference to stainless steel (AMS 5616). An analytical model comprised of statically loaded elastic structures represented by slender prismatic beam members was used to determine tandem blade stress. Figure 62 presents a graphic description of the analytical model. The front and rear airfoils of Rotors B and C were each divided into ten elements and the interblade bridge was divided into three elements. The beam members or elements were represented by their centroidal axis and analyzed as line elements. Centrifugal and aerodynamic loads were then applied to each element to yield reactions and displacements of the element or the element end, i. e., joint. These values were then used to calculate the total stress values shown in figures 63 and 64 for Rotors B and C, respectively. Maximum stress in each blade occurred in the leading edge of the front airfoil at the hub. These stresses were 23,000 psi for Rotor B and 26,000 psi for Rotor C. The maximum interblade bridge stresses were 11,200 psi and 15,000 psi for Rotors B and C, respectively. These calculated steady-state blade element stresses are well within the 0.2% yield strength of 104,000 psi for titanium (AMS 4973).

Rotor Vibratory Analysis

Rotor A

Bending and torsional vibratory frequencies were calculated for Rotor A and the results presented in terms of frequency vs rotor speed in figure 65. At design equivalent rotor speed the calculated bending and torsional vibratory frequencies were 680 cps and 1450 cps, respectively. Lines representing multiples of rotor frequency (E) are shown in figure 65 to permit identification of resonant operating conditions that might possibly be encountered during testing, due to upstream bearing support struts, rotating stall zones, or upstream

instrumentation. Because of the relatively high resonant frequencies shown in figure 65 and the large vibratory stress margin available (as indicated by the Goodman diagram of figure 66, i. e. , 55,000 psi based on the smooth fatigue strength and 19,000 psi based on the notched fatigue strength), no Rotor A vibratory problem is anticipated.

Rotor B and Rotor C

Bending vibratory frequencies were calculated for the individual front and rear airfoils and the bridged airfoil configurations of tandem Rotors B and C, and the results are shown in terms of frequency vs rotor speed in figures 67 and 68. The calculated frequencies for the front and rear airfoils of Rotor B at design equivalent rotor speed were 290 and 380 cps. The corresponding values for Rotor C are 285 and 340 cps. The bridged blade bending frequencies were determined by restraining the front and rear airfoils at the bridge location such that bending vibratory motion was permitted in one plane, i. e. , at one shroud angle. The shroud angle was then varied until both the front and rear airfoils achieved the same frequency, or theoretically vibrated together. The frequencies so calculated for tandem Rotors B and C at design equivalent rotor speed were approximately 550 and 420 cps, respectively. Since the Rotor B bending frequency, shown in figure 67, does not intersect the lines representing multiples of rotor frequency (E) at the required operating speeds (i. e. , 50, 70, 90, 100, and 110% of design speed), no resonance problem is anticipated for this rotor. As can be seen in figure 68, the first bending mode for Rotor C does intersect the 6E line at design equivalent rotor speed. This indicates a potential resonance condition because there are six inlet struts. However, no resonance condition is expected because the unequally spaced struts ($t/c = 0.12$) are located three chord lengths upstream of the rotor, and their wakes are substantially dissipated at the rotor inlet.

Torsional vibratory frequencies calculated for the front and rear airfoils of Rotors B and C at design equivalent rotor speed were 1215 and 1280 cps and 1210 and 1270 cps, respectively. Torsional frequencies for bridged blade configurations were not calculated since the individual airfoil frequencies were well above the 6E excitation frequency, as shown in figures 67 and 68. To illustrate the vibratory stress margin present in the design of Rotors B and C, a Goodman diagram for AMS 4973 is presented in figure 69. As shown in figure 69, allowable vibratory stress to failure for Rotors B and C are 44,000 and 42,000 psi, respectively, based on the smooth fatigue strength and 28,000 and 26,500 psi, respectively, based on the notched fatigue strength. Neither configuration indicated a vibratory fatigue problem.

Rotor Flutter Analysis

Rotor A

Values of the reduced velocity and incidence parameters were calculated for Rotor A at the design operating conditions and for the estimated negative and positive incidence operating limits and compared to correlated flutter data for

the first bending and first torsional vibratory frequencies (figure 70). The reduced velocity parameter is defined as:

$$K = \frac{12V}{\pi c \omega}$$

and the incidence parameter is defined as:

$$f(i_m) = \frac{i_m - i_{m_{ref}}}{\text{low-loss incidence range}}$$

where V , c , $i_{m_{ref}}$, and low-loss incidence range are the values for airfoil sections located at 25% span from the tip. The low-loss incidence range and $i_{m_{ref}}$ were determined from an unpublished P&WA cascade data correlation. The bending and torsional mode flutter calculations were made at Mach numbers of 0.4 and 0.6, respectively, so that the values obtained could be compared with the correlated data. As indicated by the operating envelopes shown in figure 70, no bending or torsional flutter problems are anticipated for Rotor A.

Rotor B and Rotor C

Values of the reduced velocity and incidence parameters were calculated for the individual front and rear airfoils of Rotors B and C at the design operating conditions and the results are compared to correlated flutter data in figures 71 and 72. Based on the narrow safe operating ranges associated with the high reduced velocity parameters for the individual airfoils, a 0.060-in. thick interblade bridge was added to both Rotors B and C at 30% span to increase the blade natural frequencies.

The reduced velocities and incidence parameters for the bridged blades were calculated using the overall chord dimensions and the front airfoil incidence angles and velocities. This was done because the front airfoil of the tandem configuration is subjected to incidence angle variations, while the incidence angle variations on the rear airfoil are expected to be small because of the small variations in exit air angle from the front airfoil. The overall chord was used because the bridged blades will move together in the immediate bridge region. The Rotor B and Rotor C reduced velocity parameters for bending operating ranges were based on the calculated bridged blade frequencies. However, since the bridged blade torsional frequencies were not available, the rear airfoil frequencies were used to calculate the torsional reduced velocity parameter. Because individual airfoil frequencies are expected to be less than the bridged blade frequencies, any conclusion based on the individual airfoil should be conservative. Values of the reduced velocity and incidence parameters for tandem Rotors B and C at the design operating conditions and the estimated negative and positive incidence limits are shown in relation to correlated flutter data in figures 71 and 72. As indicated by the operating envelopes shown in figures 71 and 72, no bending or torsional flutter problems are anticipated for either Rotor B or Rotor C.

Rotor Attachment

Blade spindle tensile, bending, shear, and bearing stresses were calculated considering the airfoil centrifugal forces and gas bending stresses due to aerodynamic loading. The calculations were performed at a rotor speed of 6000 rpm, which is approximately 140% of design speed. The results of the stress calculations for Rotors A, B, and C are presented in table VIII. The combined tensile and bending spindle stresses calculated for Rotor A and Rotors B and C were 67,700 and 30,200 psi, respectively. These calculated stresses are well within the 0.2% yield strengths of 114,000 and 104,000 psi of the stainless steel (AMS 5616) and titanium (AMS 4973) selected for Rotor A and Rotors B and C, respectively. Similarly, calculated shear and bearing stresses of 12,900 and 84,000 psi for Rotor A and 5,760 and 37,500 psi for Rotors B and C, respectively, did not exceed the specified material limitation shown in table VIII (i. e., allowable shear stress equals 55% of material ultimate tensile strength and allowable bearing stress equals 120% of material 0.2% yield strength). Consequently, no blade attachment stress problems are anticipated.

Rotor Disk and Carrier

The average tangential stress for the AMS 6415 (low alloy steel) rotor disk and carrier was determined through the use of a computer disk analysis program and found to be well within design practice for AMS 6415 (0.2% yield strength of 140,000 psi). The results of this analysis are presented in table IX.

Stator Steady-State Stress Analysis

The gas bending stresses in the leading and trailing edge and on the concave surface at the point of maximum thickness were calculated for Stator A and the front and rear airfoils of Stator B. Calculations were made assuming (1) the vanes would be fabricated from AMS 5613, a stainless steel that has a 0.2% yield strength of 110,000 psi and (2) the vanes were beams that would deflect as guided cantilevers about the tip. The guided cantilever about the tip condition was selected, even though the stator vanes are attached to the shrouds by trunions at both the hub and tip, to provide a conservative estimate of the vane stresses. Some movement of the vane at the hub is possible. These stress values are shown in figure 73 for Stator A and in figure 74 for Stator B. The maximum bending stress of 2650 psi occurred in the trailing edge tip of Stator A. A maximum Stator B front airfoil bending stress of 4000 psi (compressive) was calculated for the convex surface at the tip. The maximum rear airfoil stress was 12,000 psi and occurred in both the leading and trailing edges at the tip. None of the calculated stator stresses were prohibitive because of the high yield strength of the vane material and no stress problem is anticipated.

Table VIII. Blade Attachment Stress

(6000 rpm)

Type Stress, psi	Tensile	Bending	Combined Tensile and Bending	Shear	Bearing
Rotor A AMS 5616 Stainless Steel	37,000	30,700	67,700	12,900	84,000
Maximum Allowable Stress for AMS 5616 at 200 °F	114,000*	114,000*	114,000*	75,000**	136,000***
Rotor B and Rotor C AMS 4973 Titanium	16,500	13,700	30,200	5,760	37,500
Maximum Allowable Stress for AMS 4973 at 200 °F	104,000*	104,000*	104,000*	65,000**	124,000***

*0.2% Yield Strength at 200 °F

**Allowable Shear Stress = 0.55 x Ultimate Tensile Strength at 200 °F

***Allowable Bearing Stress = 1.2 x 0.2% Yield Strength at 200 °F

Table IX. Disk and Carrier Stress
(6000 rpm)

Configuration	Rotor A	Rotor B and Rotor C
Disk (AMS 6415) Stress, psi	94,000	42,000
Carrier (AMS 6415) Stress, psi	62,000	27,700
0.2% Yield Strength of AMS 6415 at 100°F, psi	140,000	140,000

Stator Vibratory Analysis

Bending and torsional vibratory frequencies were calculated for Stator A and Stator B front and rear airfoils and the results presented in terms of frequency vs rotor speed in figures 75 and 76. The vibratory analysis was made assuming the stators to be beams with both ends fixed (fixed-fixed mode). This assumption was permissible because stator hub and tip trunions are held in inner and outer diameter shrouds. Lines representing multiples of rotor passing frequency (70E) are shown in the figures to permit the identification of any excitation frequencies within the operating range. Stator A bending and torsional frequencies in the fixed-fixed mode were 2200 cps and 2500 cps, respectively. Stator B front and rear airfoil bending frequencies were 810 cps and 1220 cps, respectively, while the torsional frequency of both the front and rear airfoils was 2500 cps. No vibratory fatigue problems are anticipated for either Stator A or Stator B. Because of the low steady-state stress present in these vanes, a large vibratory stress margin is available, as indicated by the Goodman diagram of figure 77 for Stator A and figure 78 for Stator B. As shown in figure 77, Stator A can withstand 56,000 psi vibratory stress based on the smooth fatigue strength and 21,000 psi based on the notched fatigue strength. Similarly shown in figure 78, Stator B front and rear airfoils can withstand 55,000 and 51,000 psi vibratory stress, respectively, based on the smooth fatigue strength; and 20,600 and 19,000 psi, respectively, based on the notched fatigue strength.

Stator Flutter Analysis

Stator A and Stator B front and rear airfoil torsional stall flutter characteristics were calculated and presented for comparison with correlated flutter data in figures 79 and 80. The flutter variables are a reduced velocity parameter K, as defined in the rotor flutter analysis section, page 18, and an average row pressure ratio, defined as:

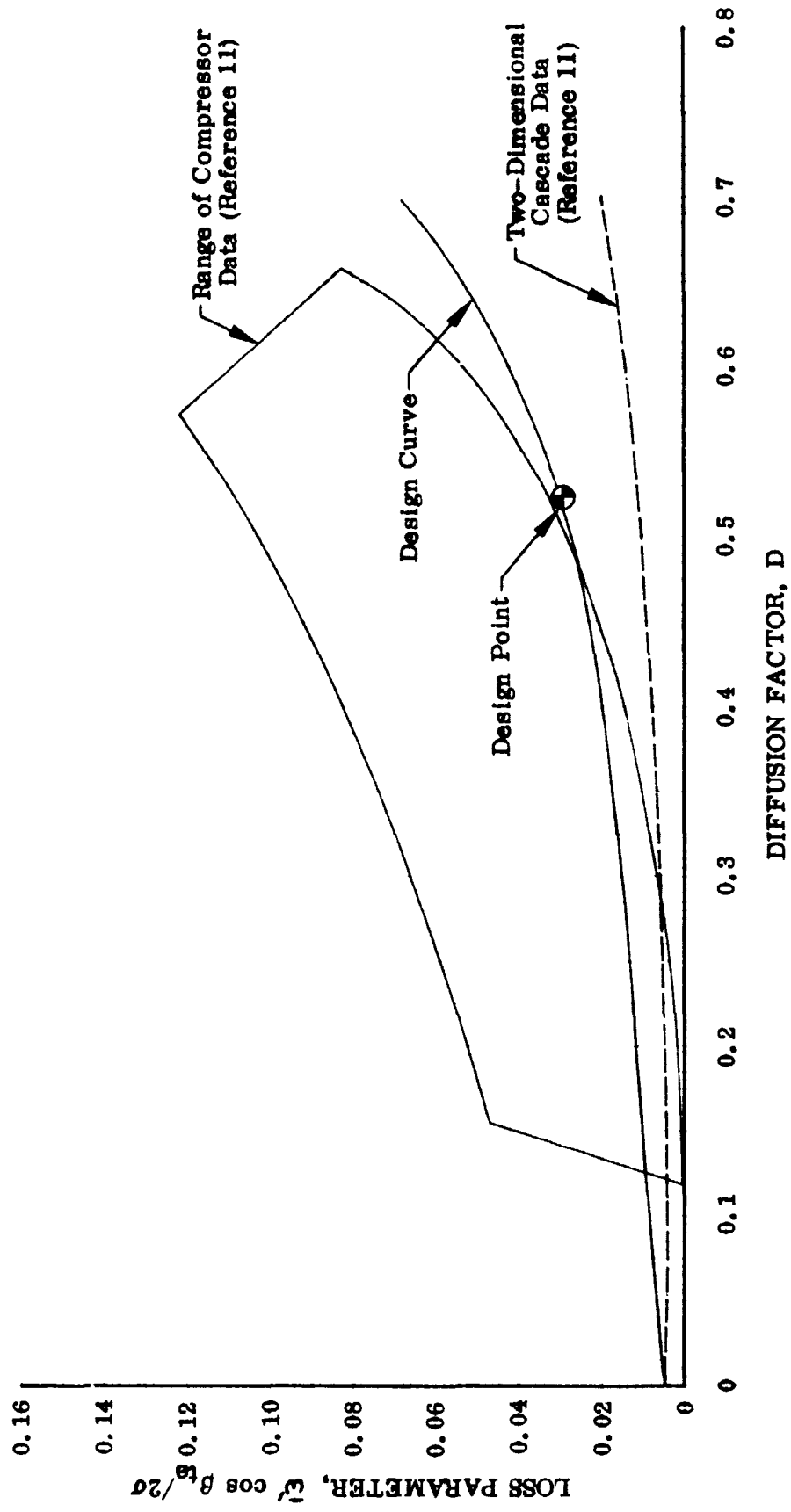
$$\frac{\frac{P_{1e} + P_{te}}{2}}{P_{1e}}$$

The values of velocity and chord used to calculate the stator reduced velocity parameter are the values at 50% span. Torsional frequencies for the

stators in a fixed-fixed configuration were used in the calculations. As shown in figures 79 and 80, no flutter problems are anticipated for Stator A or the front and rear airfoils of Stator B.

Stator Attachment

Stator assembly is achieved by tack welding the cylindrical trunions at each end of the vane into the inner and outer diameter shrouds. The cross section of primary interest for stator stress evaluation is the junction of the airfoils and trunion. For this cross sectional area of Stator A, the calculated bending stress was 13,400 psi. For Stator B front and rear airfoils, this stress was 11,300 psi and 47,000 psi. These trunion-airfoil stress values are well within the 0.2% yield strength of 110,000 psi for the AMS 5613 stainless steel material selected for stator fabrication, and no stress problems are anticipated.



83 Figure 1. Rotor Loss Parameter vs Diffusion Factor, 10% Span From Tip

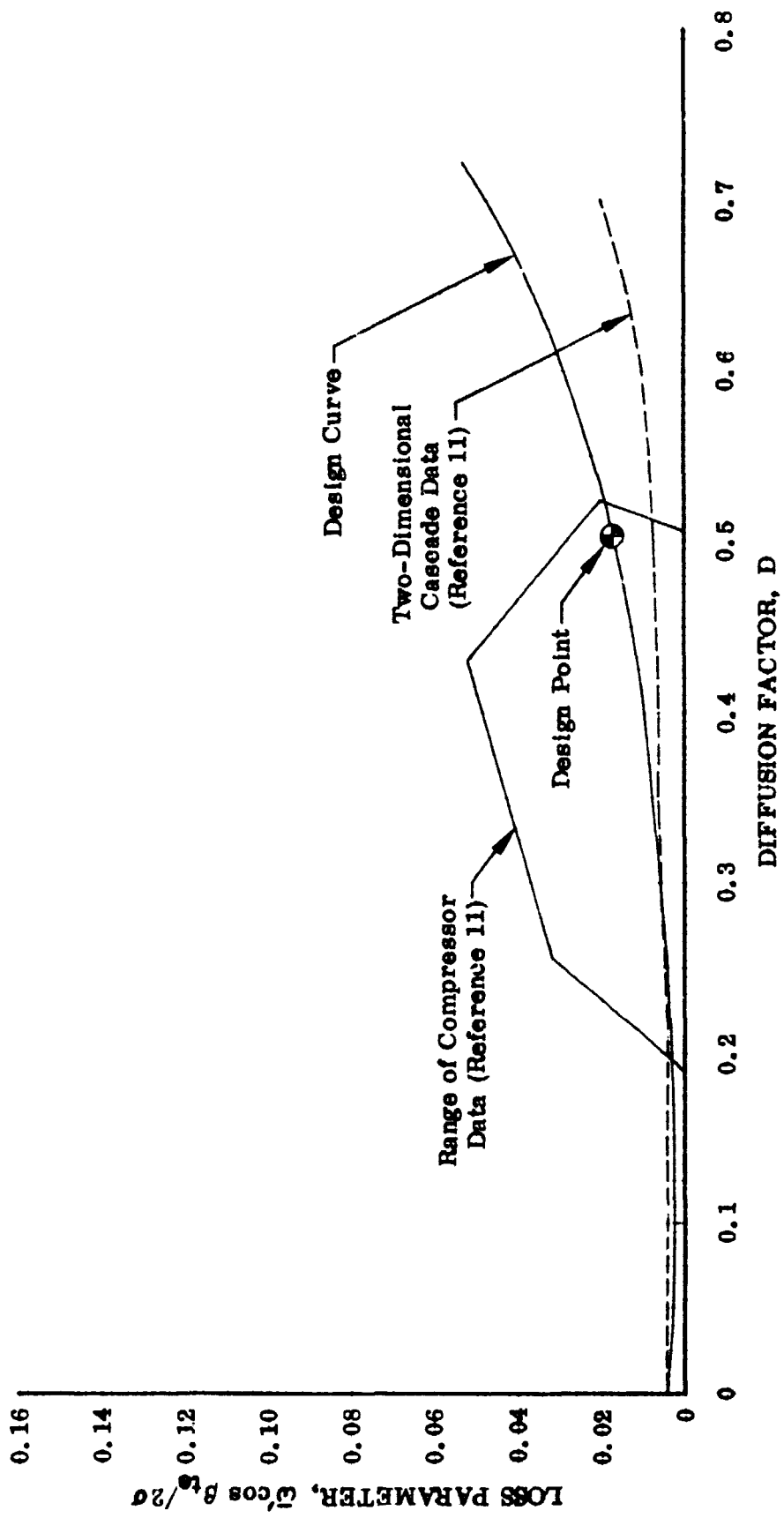
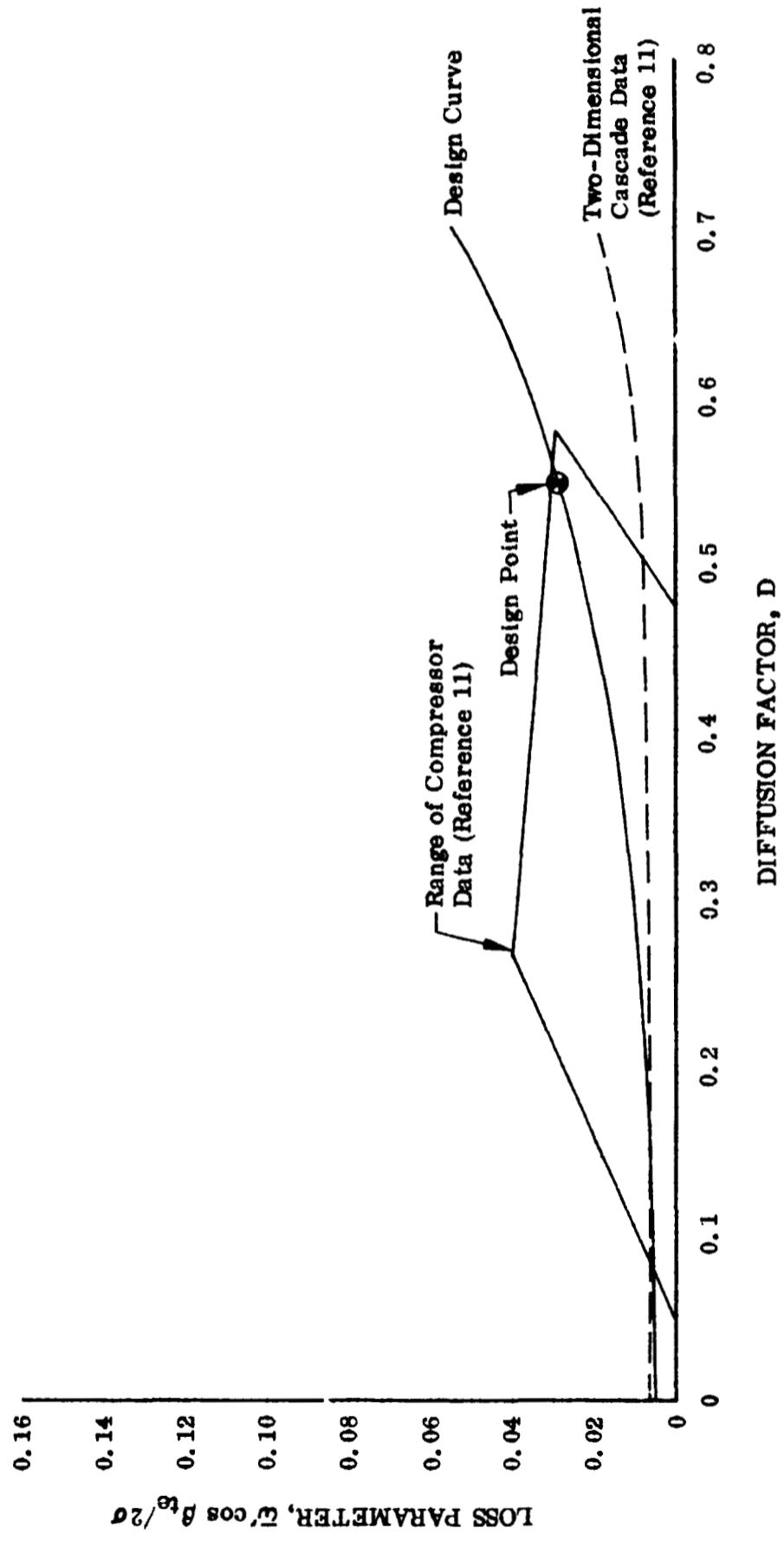


Figure 2. Rotor Loss Parameter vs Diffusion Factor, 50% Span

DF 90560



2 Figure 3. Rotor Loss Parameter vs Diffusion Factor, 90% Span From Tip

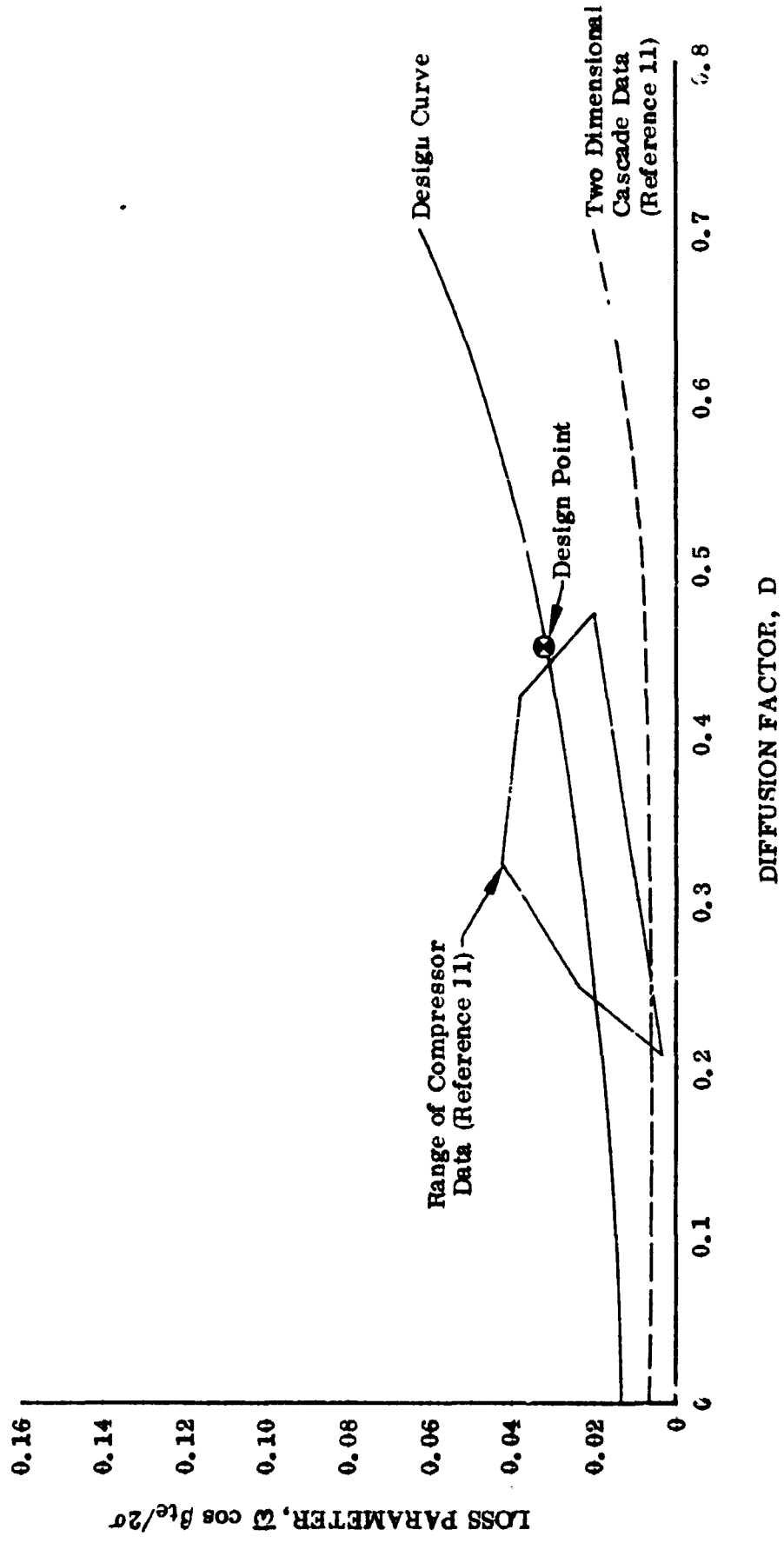
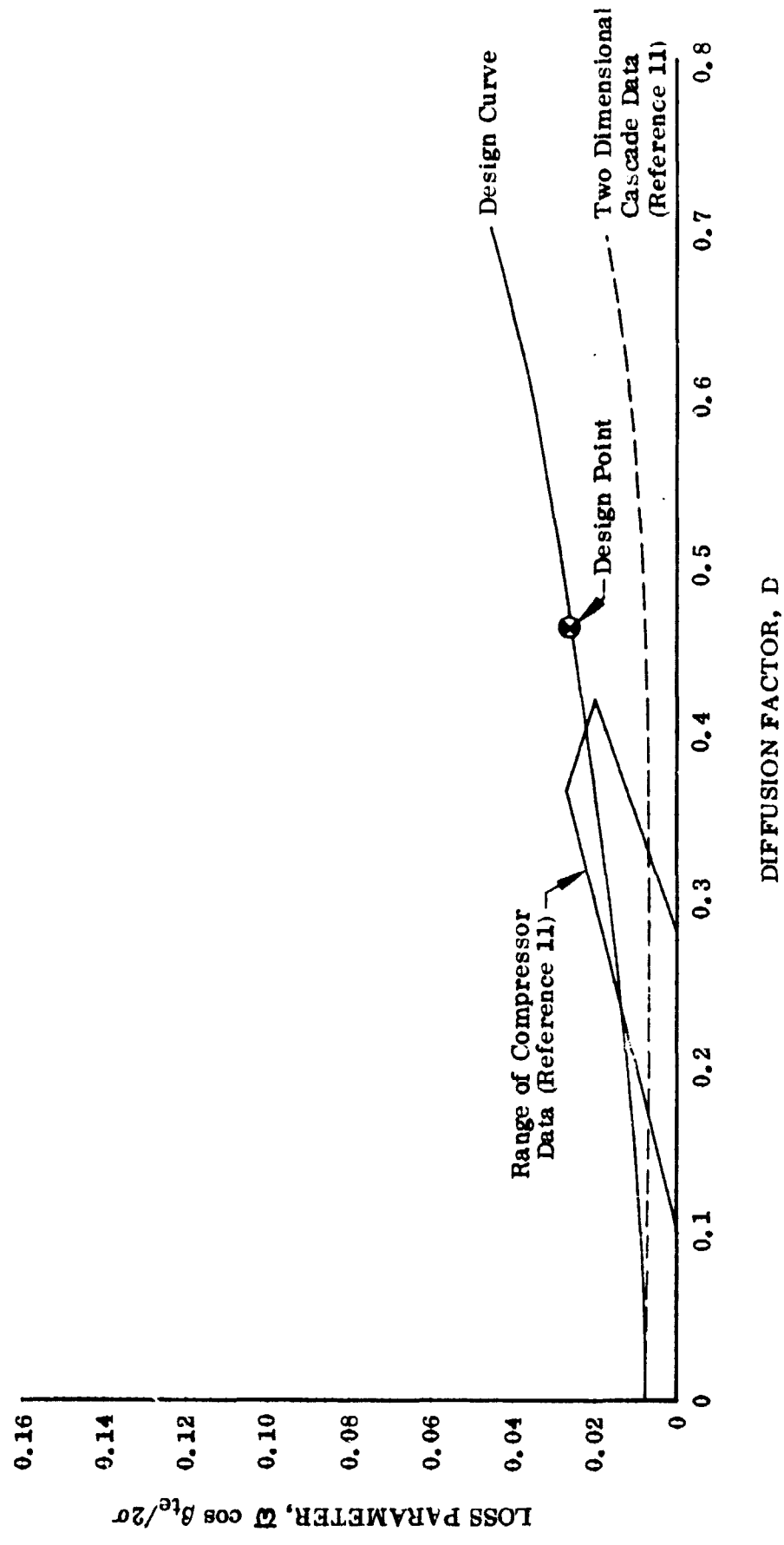


Figure 4. Stator Loss Parameter vs Diffusion Factor, 10% Span From Tip

DF 70562



27 Figure 5. Stator Loss Parameter vs Diffusion Factor, 50% Span

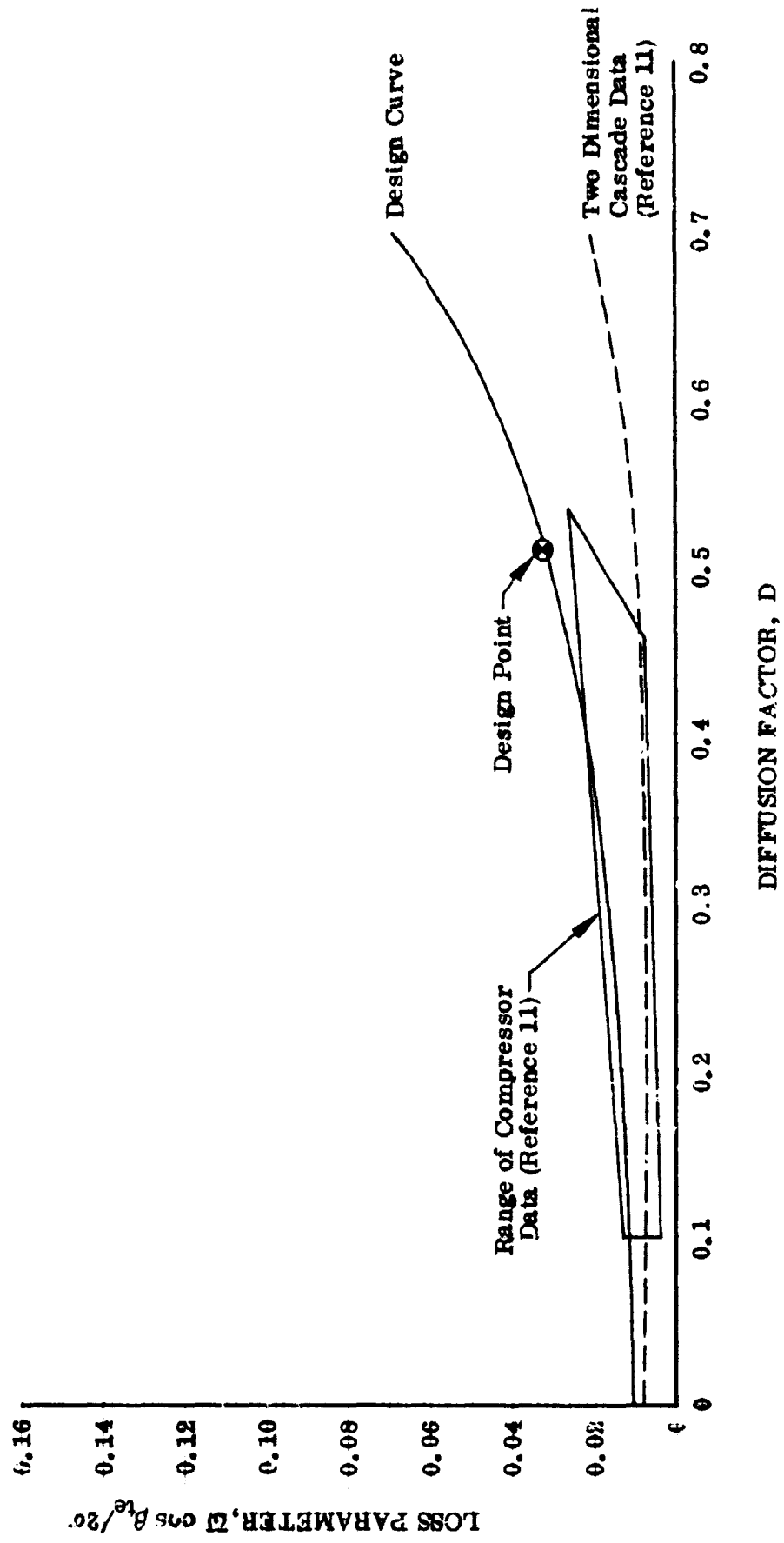
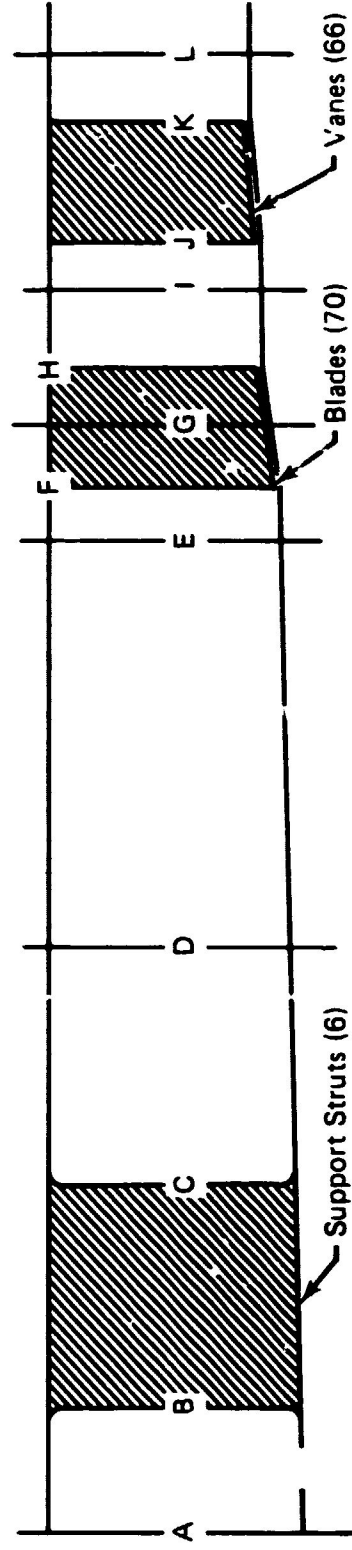


Figure 6. Stator Loss Parameter vs Diffusion Factor, 90% Span From Tip



Flow Path Location	Location Description	Inner Diameter	Outer Diameter	Axial Distance From Reference Plane
A	Reference Plane	32.850	41.790	0.0
B	Support Strut Leading Edge	32.850	41.744	2.440
C	Support Strut Trailing Edge	32.850	41.444	6.265
D	Instrumentation Station 1	32.850	41.340	10.248
E	Instrumentation Station 2	32.850	41.226	17.188
F	Rotor Inlet Station	32.850	41.145	18.061
G	Rotor Stacking Line	32.850	40.854	19.188
H	Rotor Exit Station	32.850	40.562	20.315
I	Instrumentation Station 1	32.850	40.520	21.368
J	Stator Leading Edge	32.850	40.450	22.163
K	Stator Trailing Edge and Stacking Line	32.850	39.990	24.468
L	Instrumentation Station 2A	32.850	39.990	25.418

Note: All Dimensions Are In Inches

Figure 7. Design Flowpath Dimensions for Stages A, B, and C

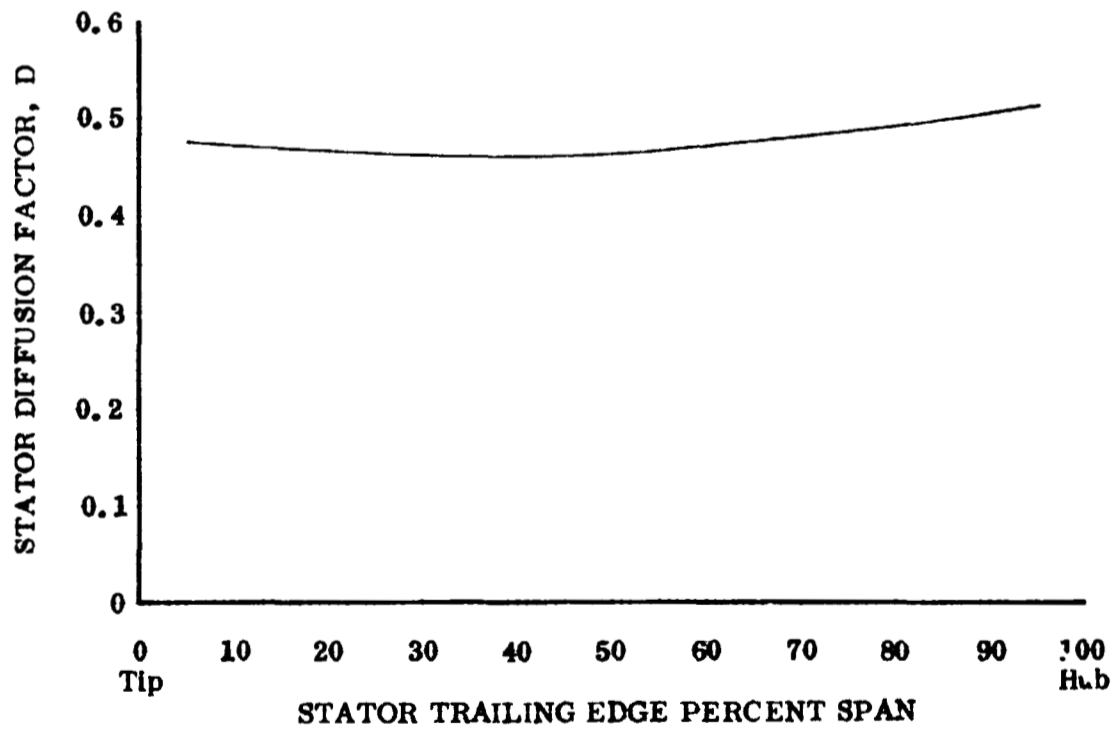
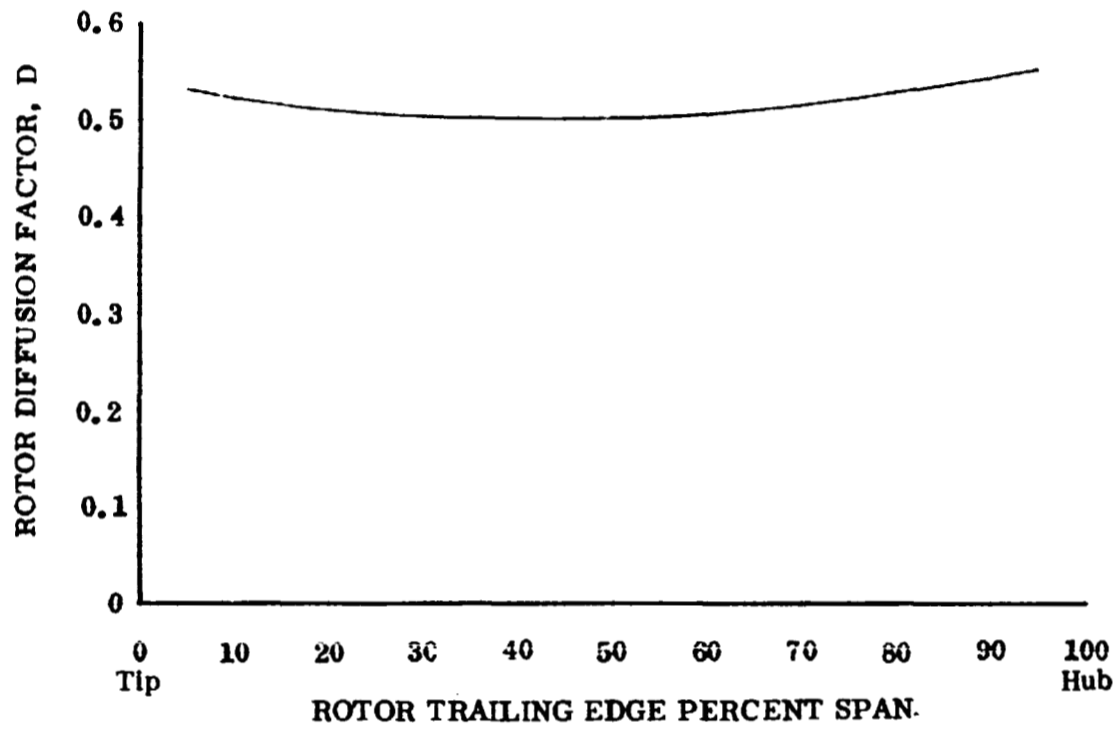


Figure 8. Rotor and Stator Loading Distributions

DF 90565

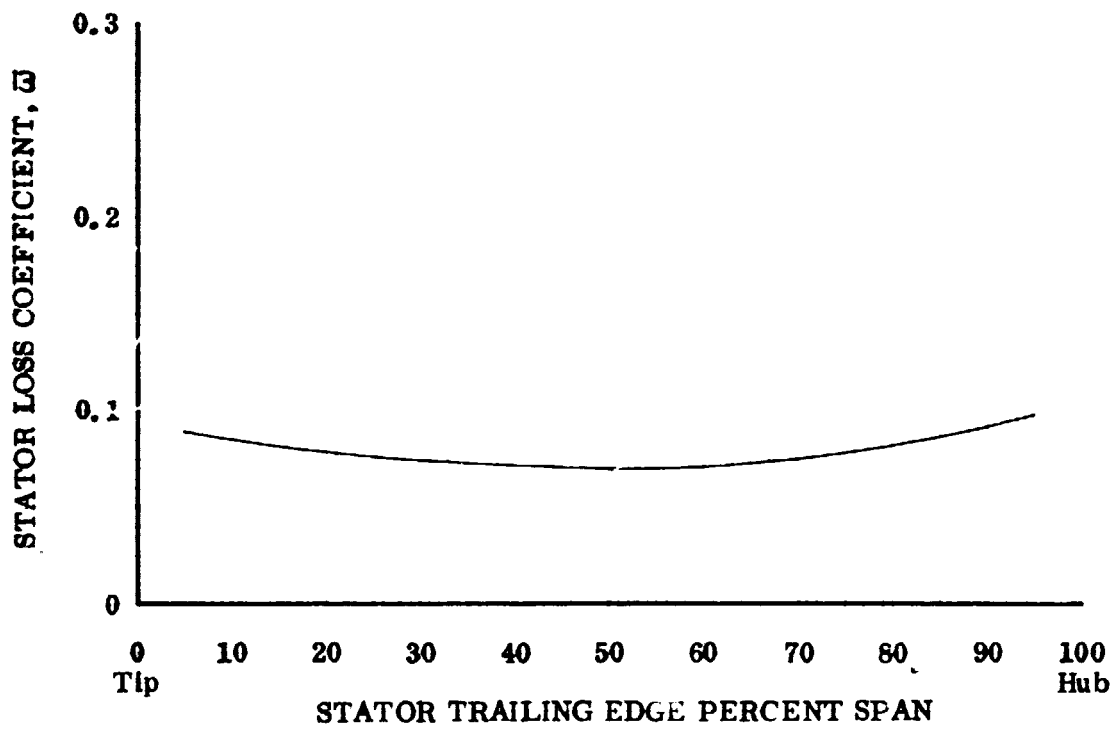
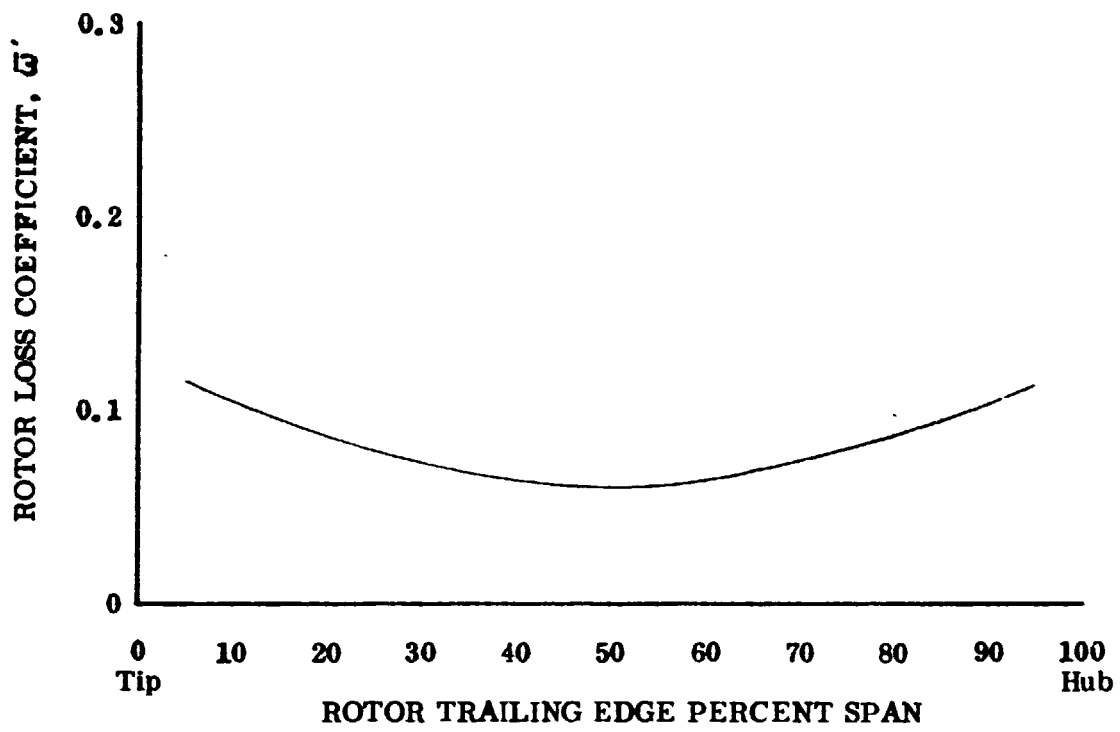


Figure 9. Rotor and Stator Loss Profile

DF 90566

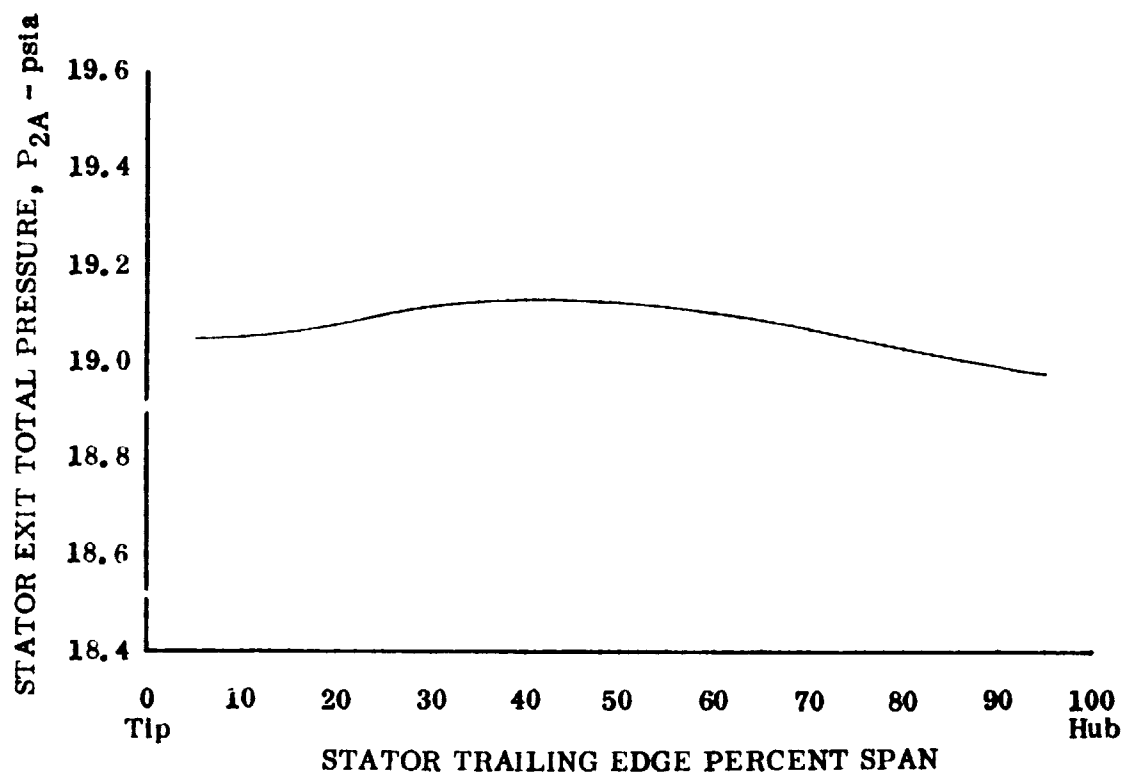
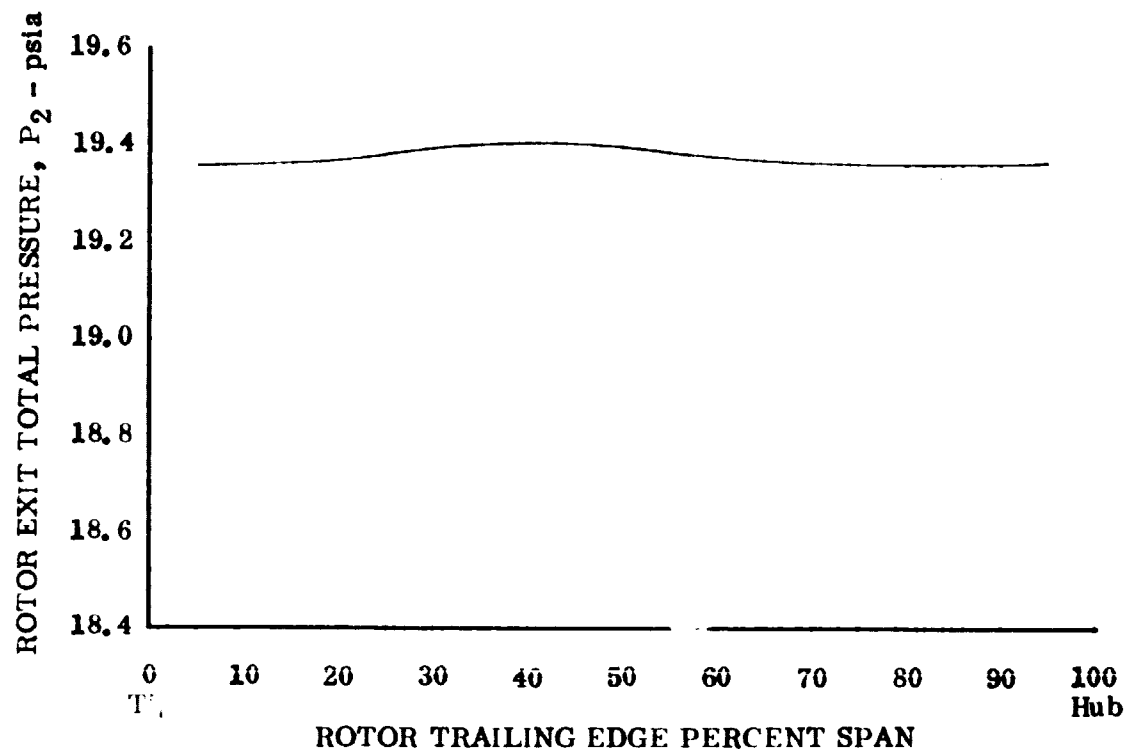


Figure 10. Rotor and Stator Exit Pressure Profile DF 90567

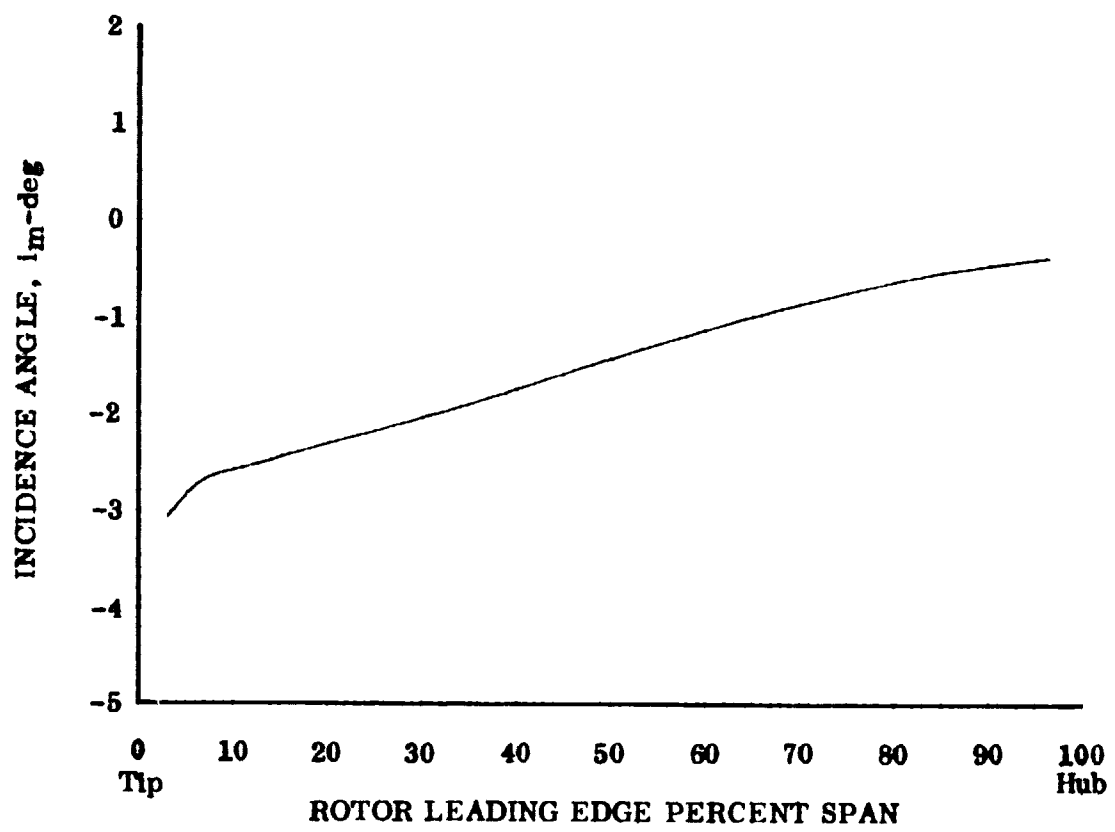
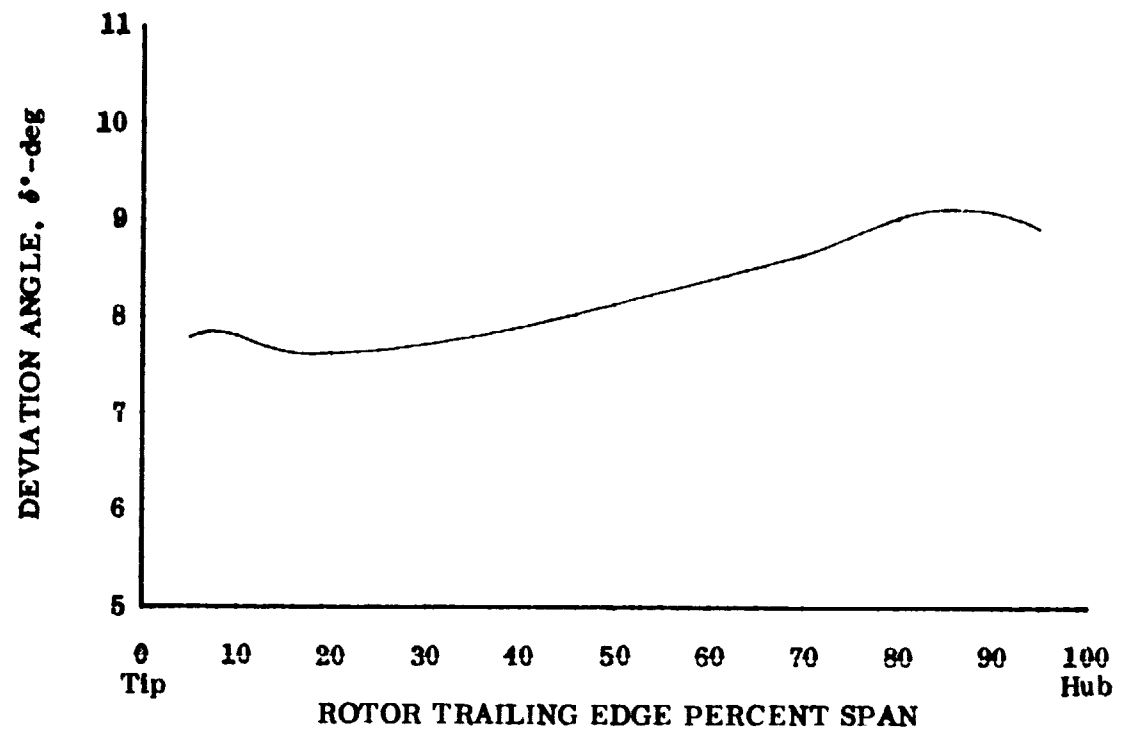


Figure 11. Rotor Incidence and Deviation Angle

DF 90568

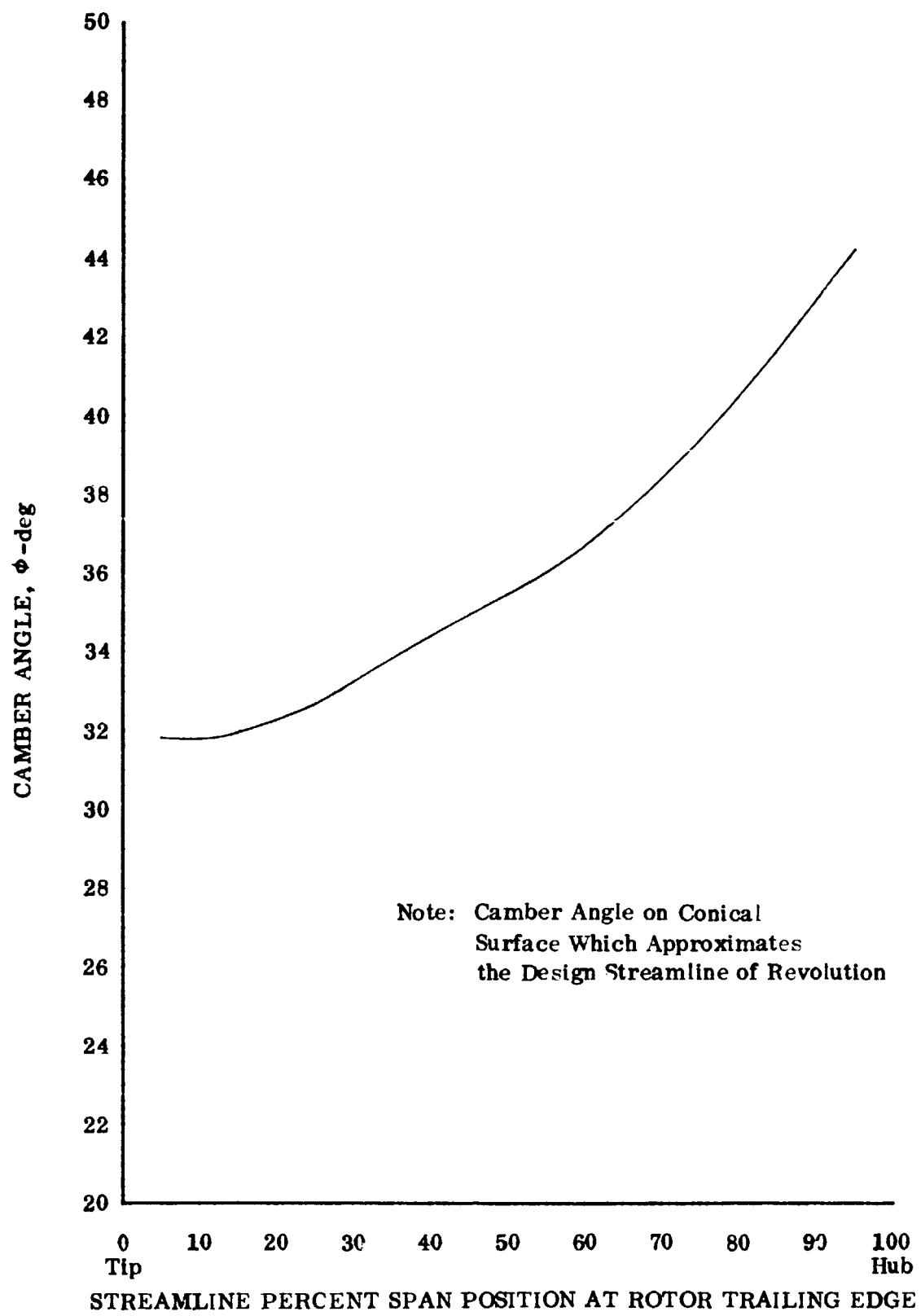


Figure 12. Rotor Camber Angle

DF 90569

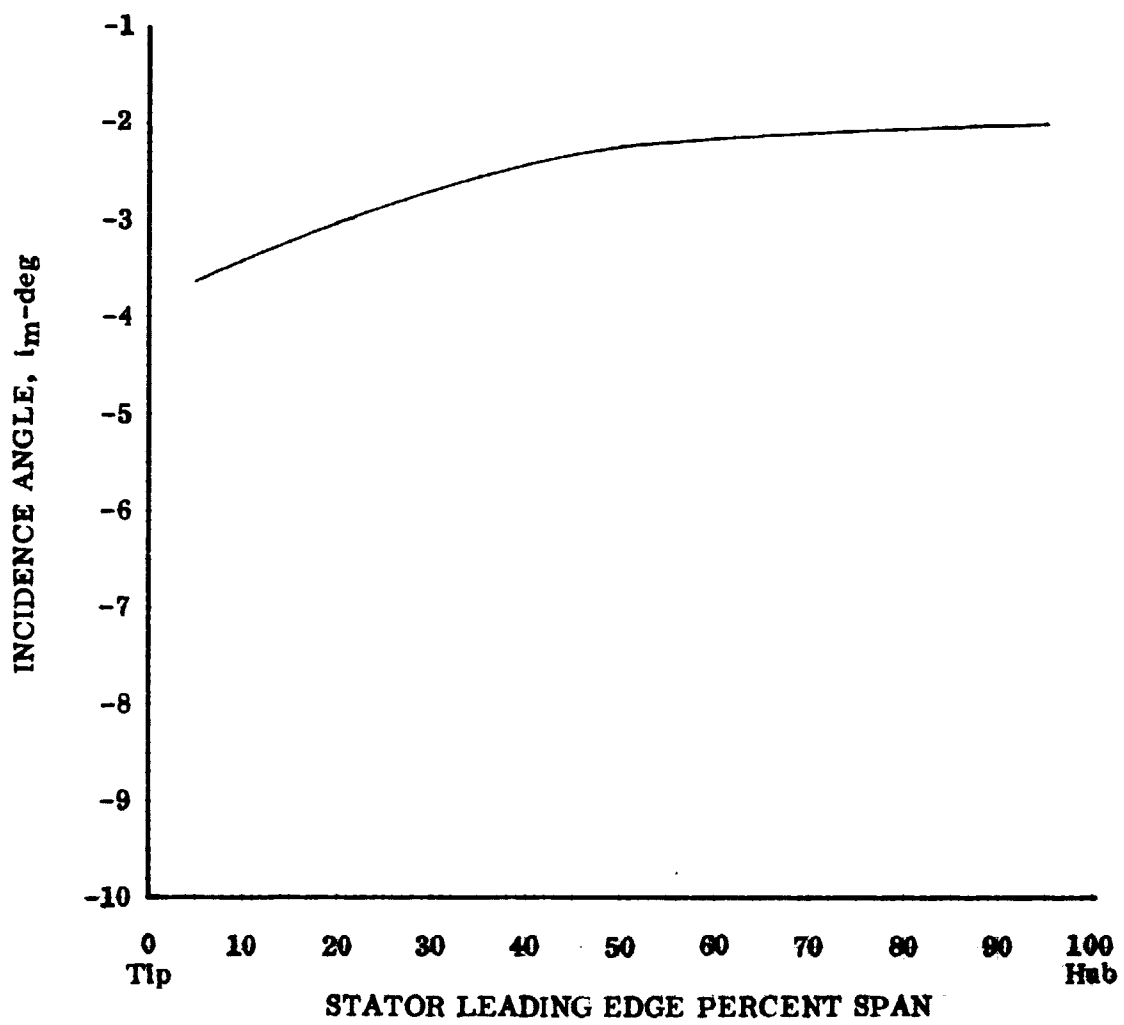
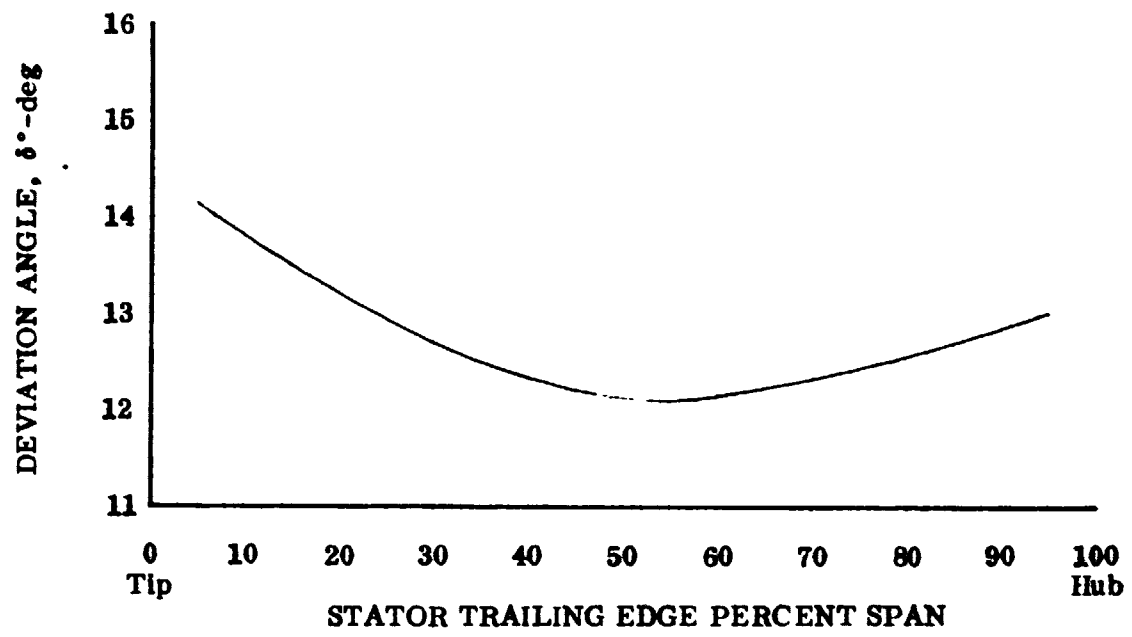


Figure 13. Stator Incidence and Deviation Angle

DF 90570

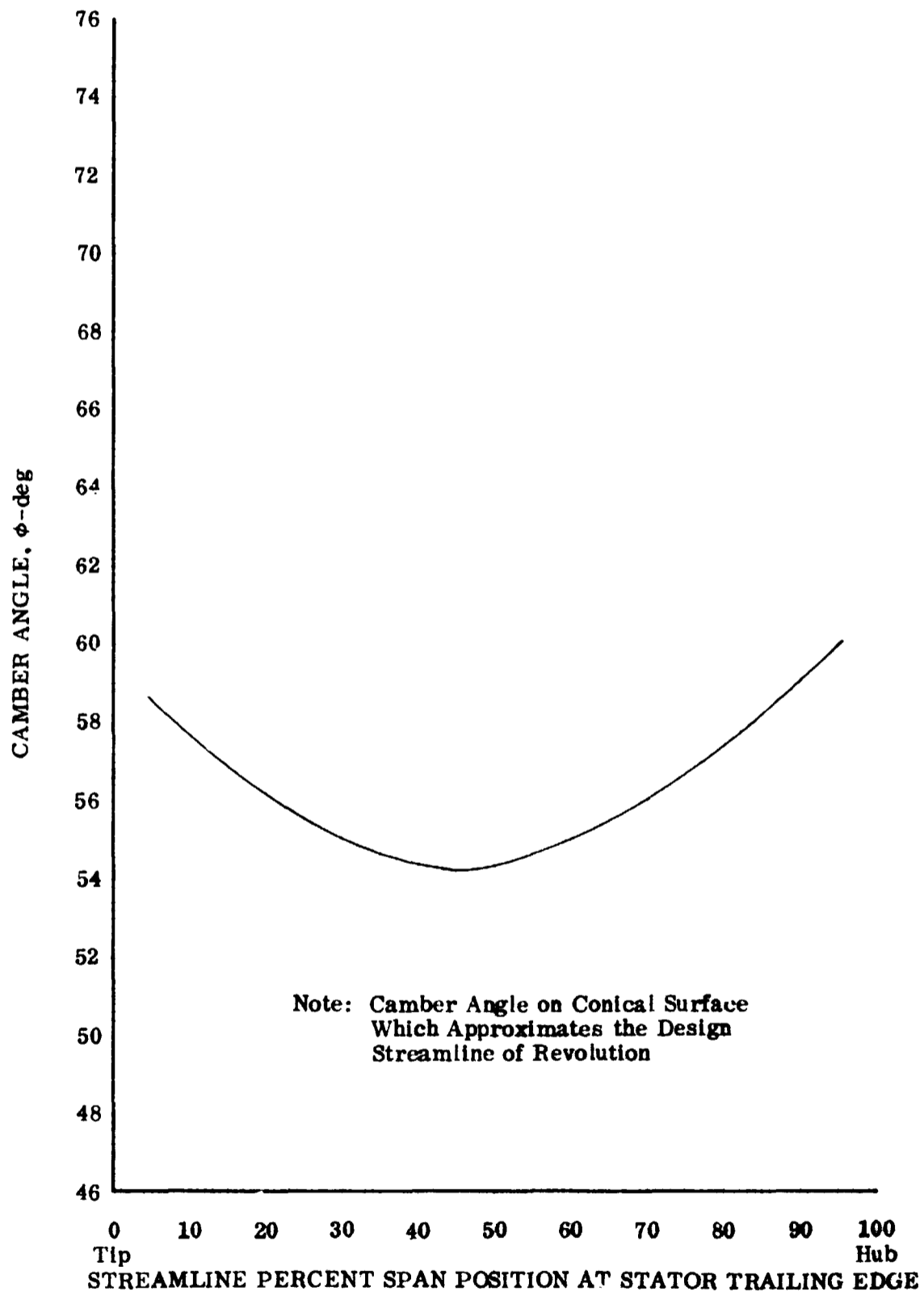


Figure 14. Stator Camber Angle

DF 90571

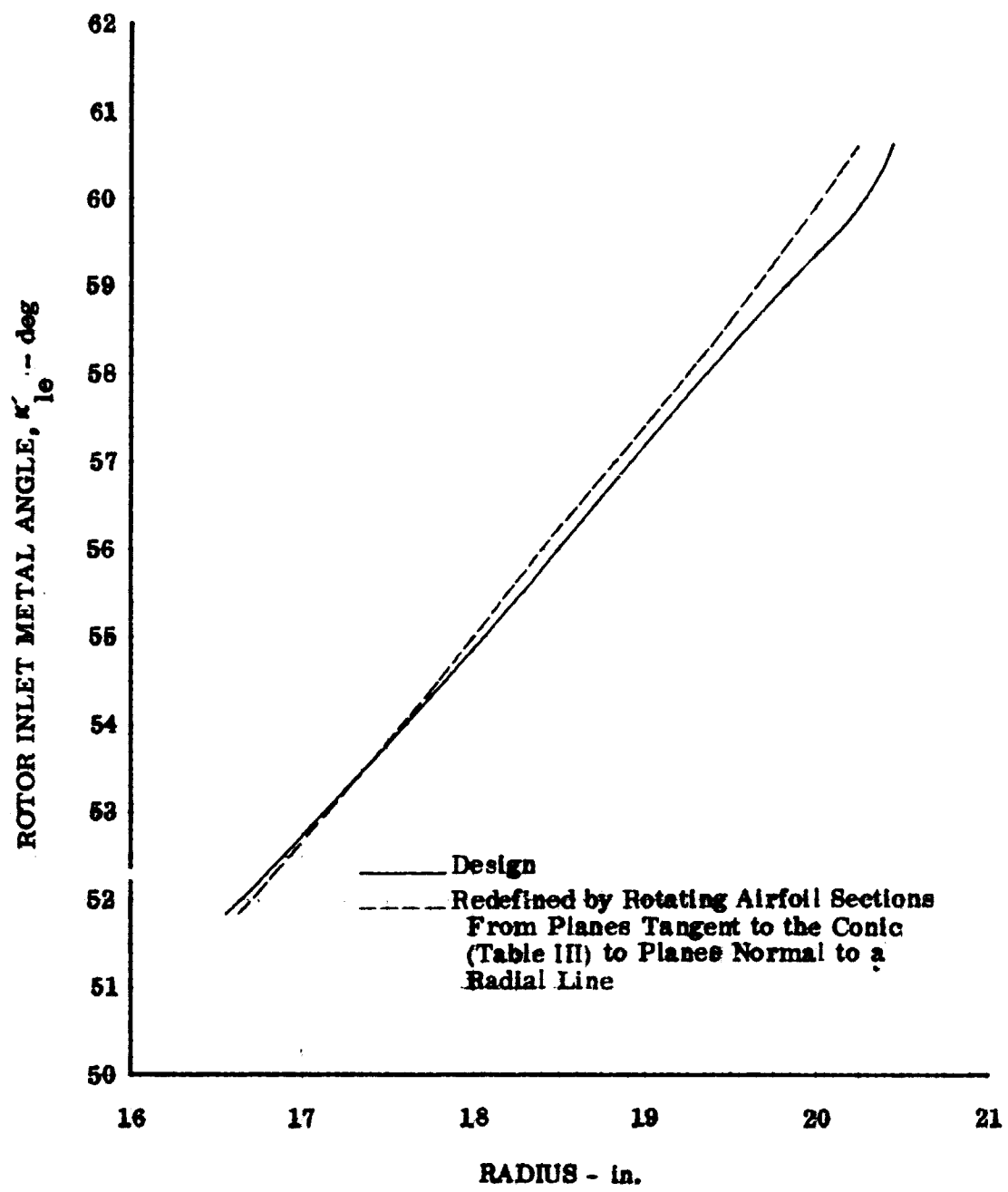


Figure 15. Rotor Inlet Metal Angle Comparison

DF 90572

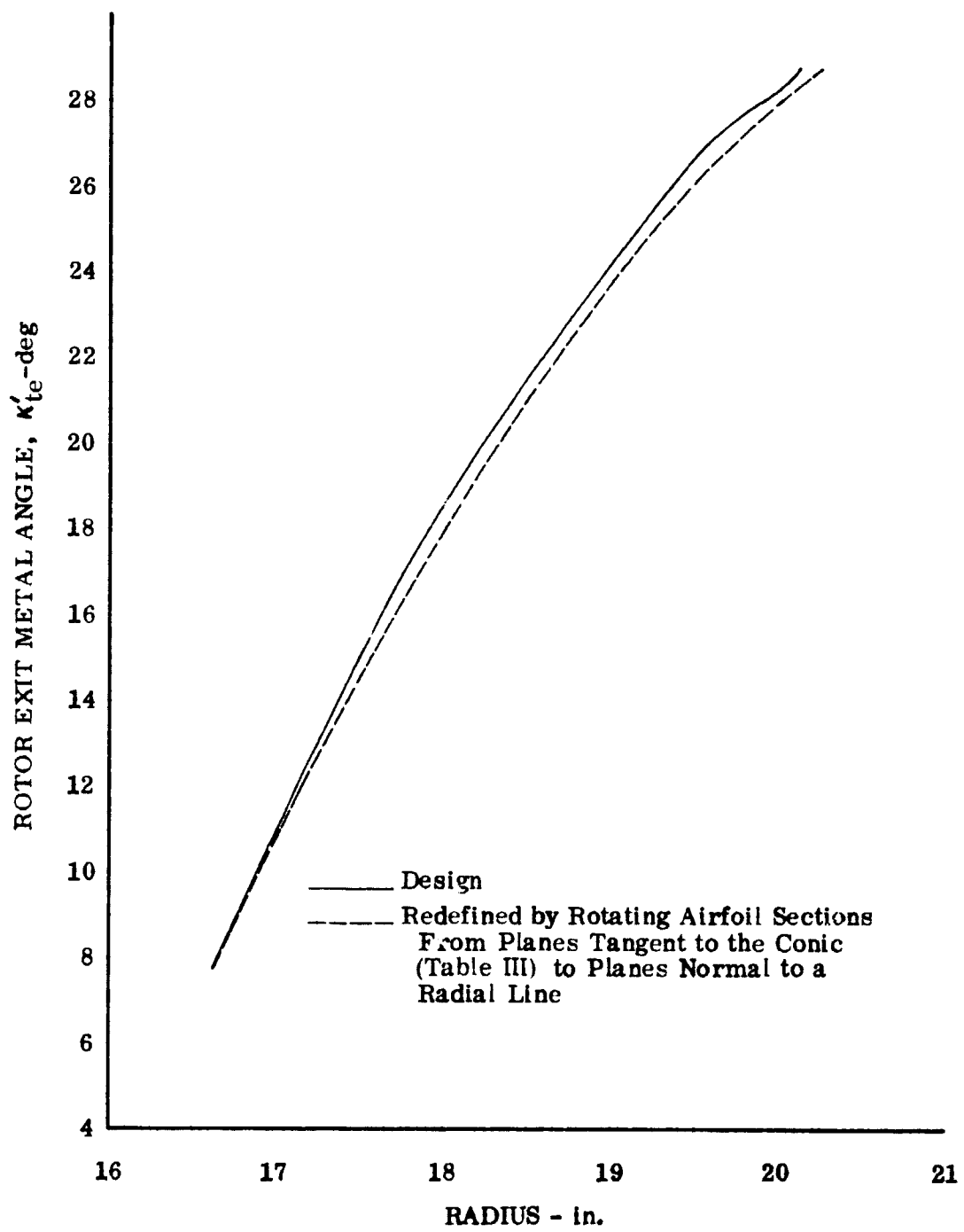


Figure 16. Rotor Exit Metal Angle Comparison

DF 90573

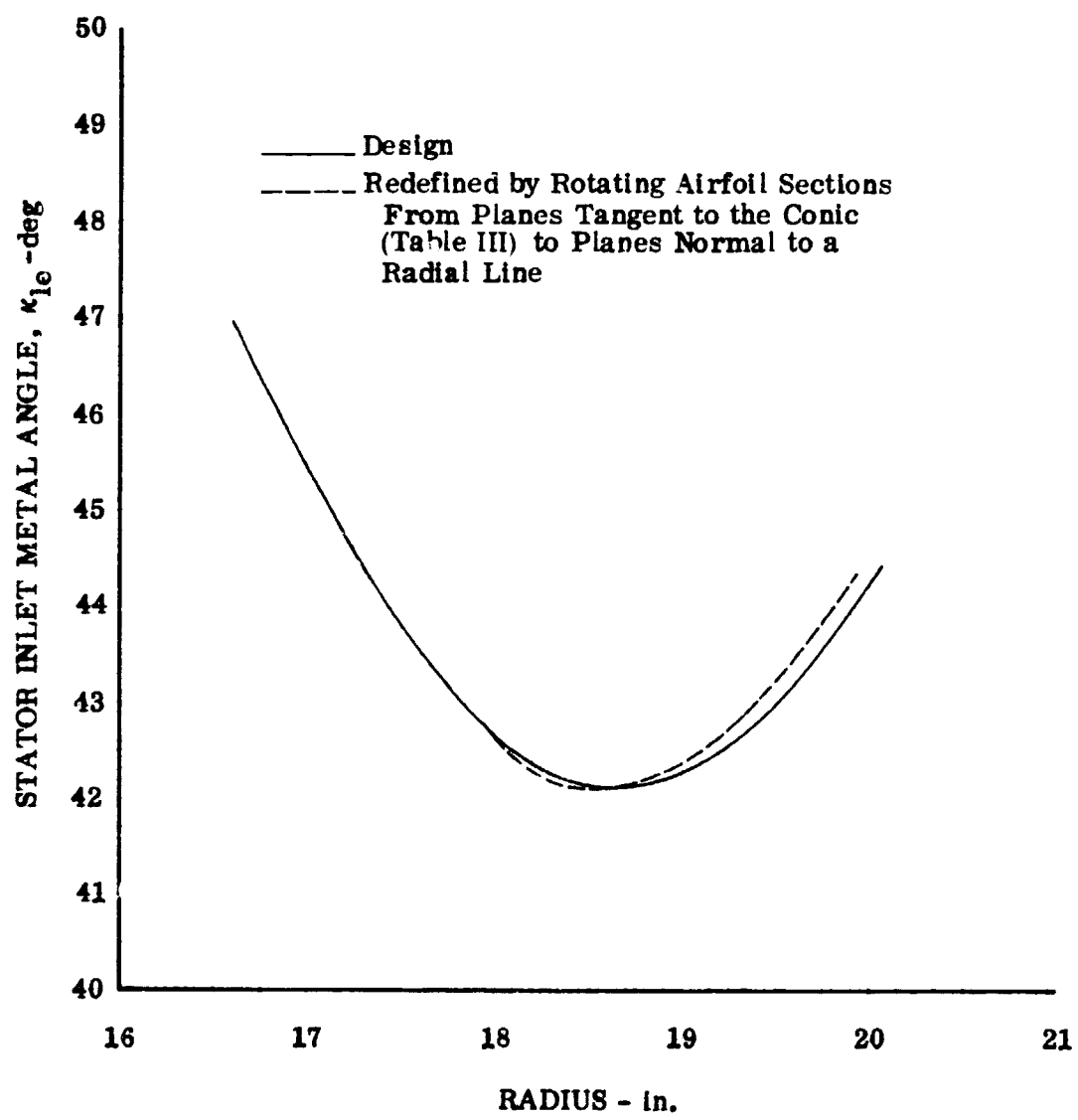


Figure 17. Stator Inlet Metal Angle Comparison

DF 90574

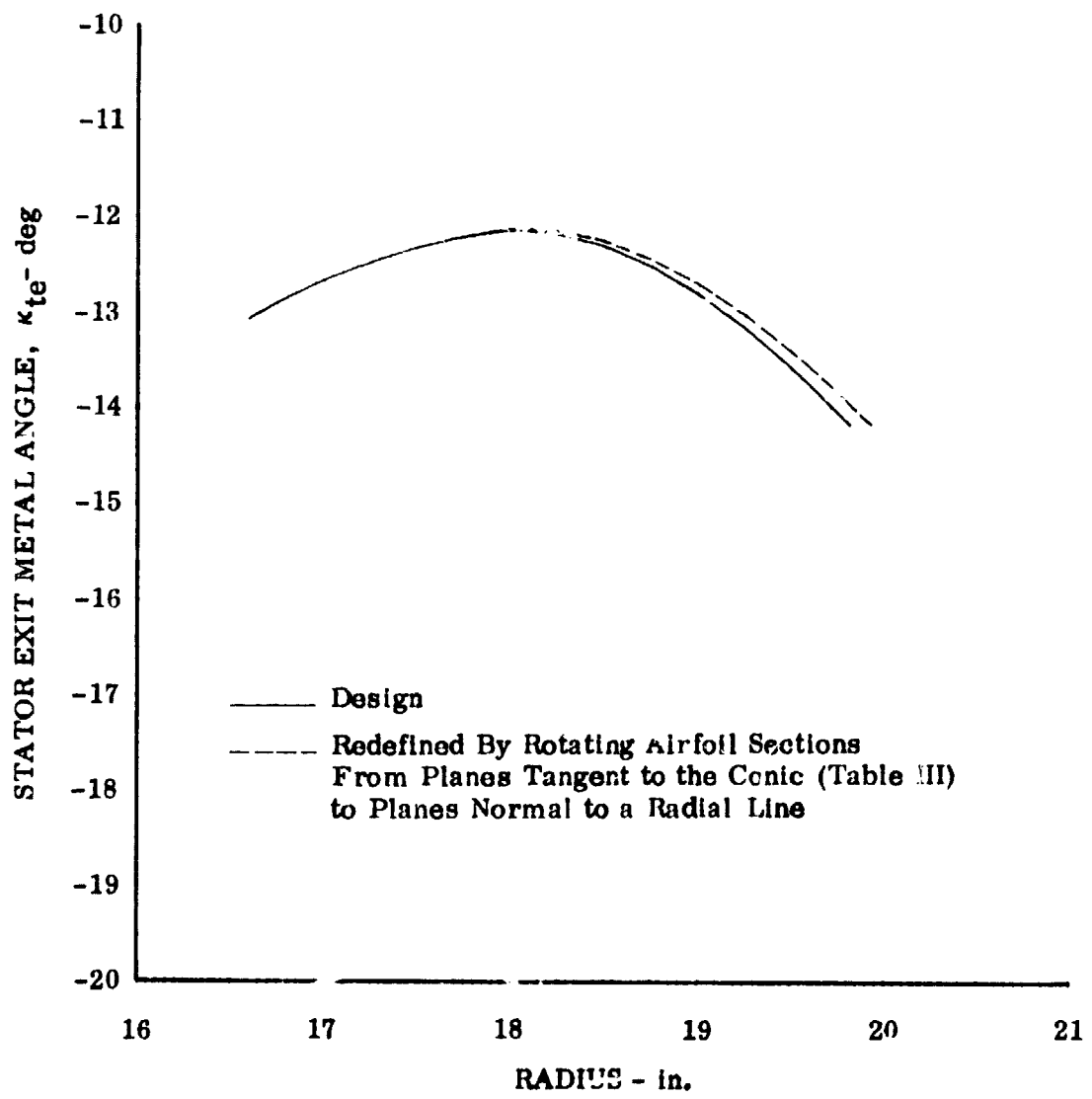


Figure 18. Stator Exit Metal Angle Comparison

DF 90575

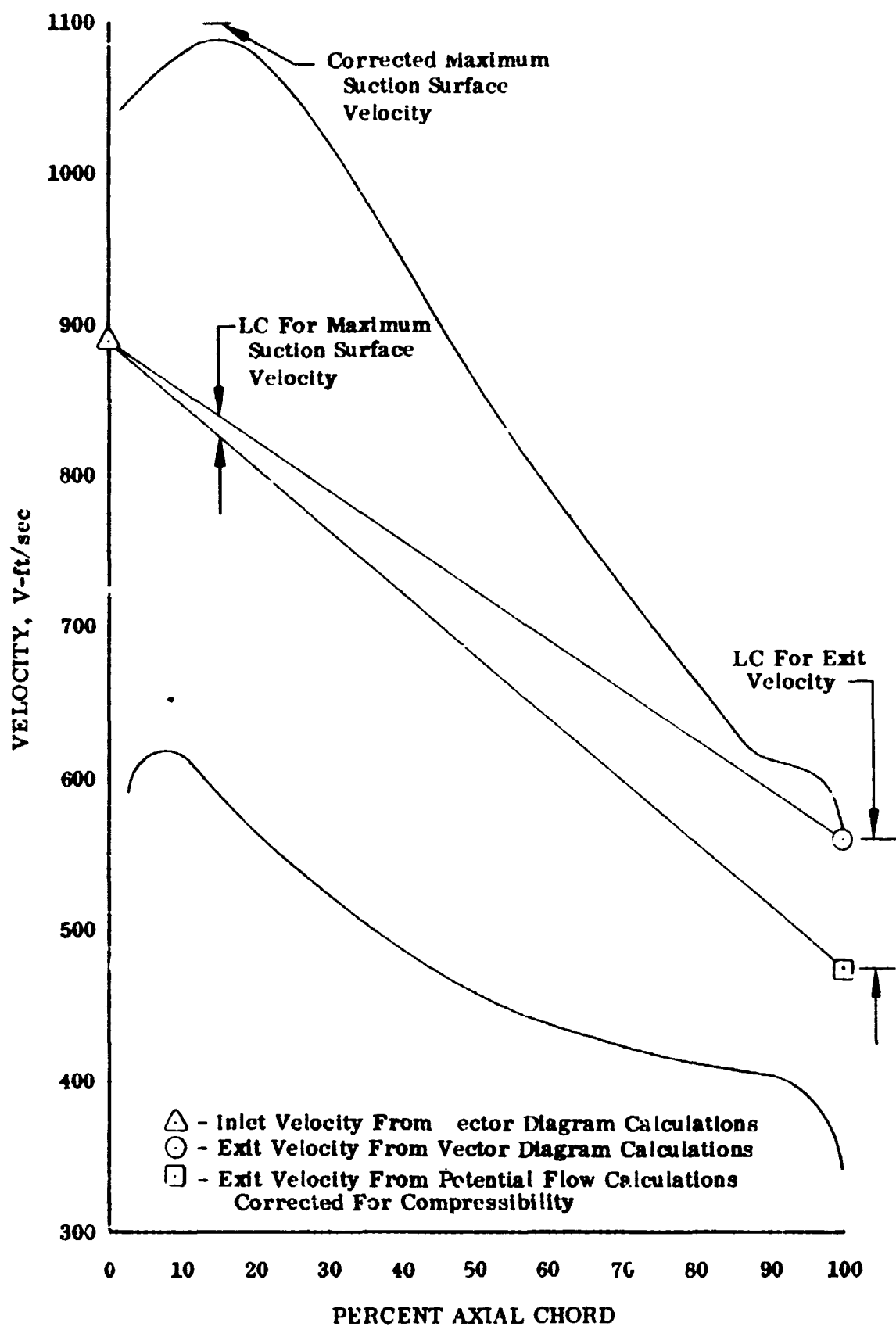


Figure 19. Rotor A Blade Surface Velocities, 5% Span DF 90576 From Tip

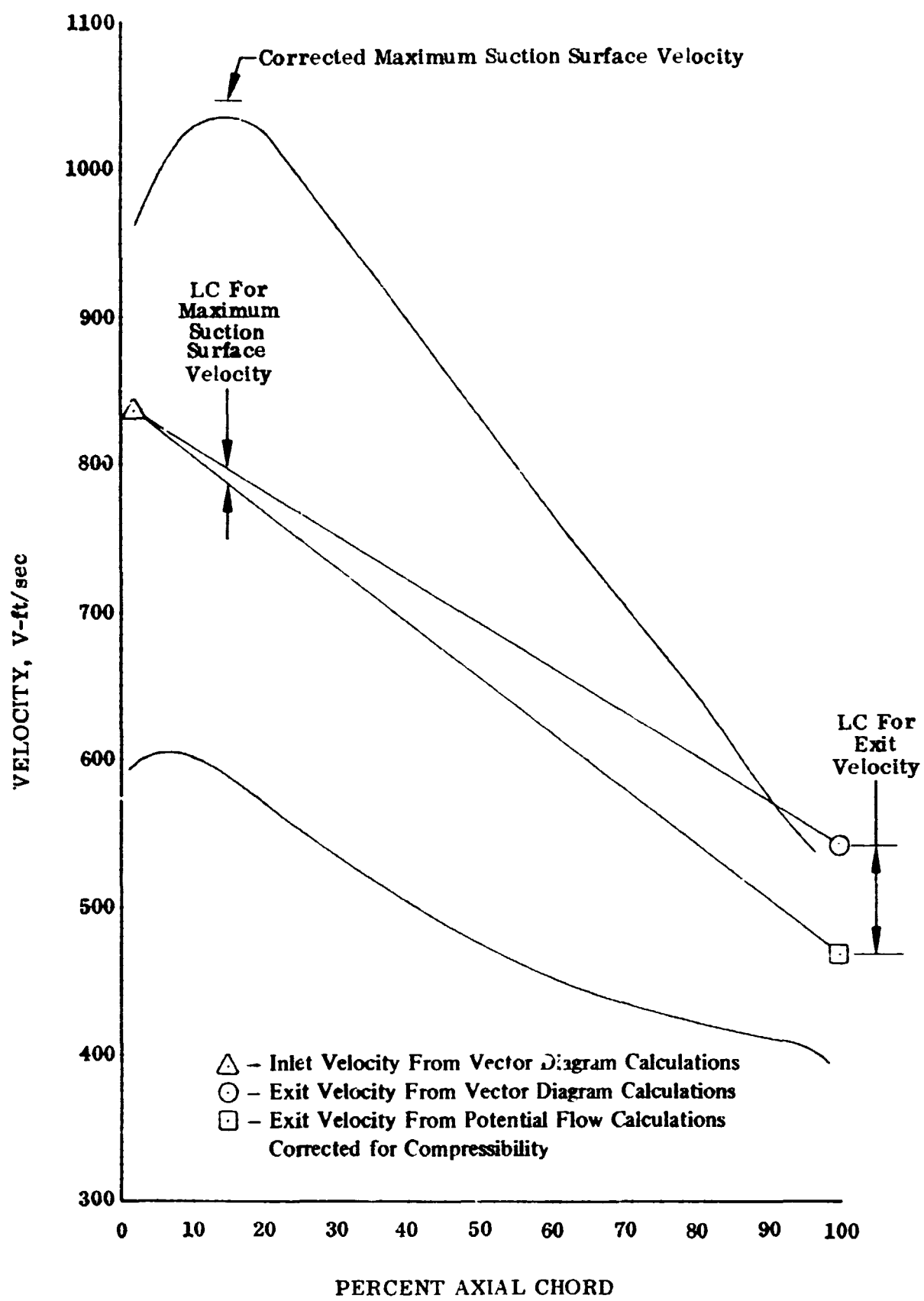


Figure 20. Rotor A Blade Surface Velocities, 50% Span

DF 90577

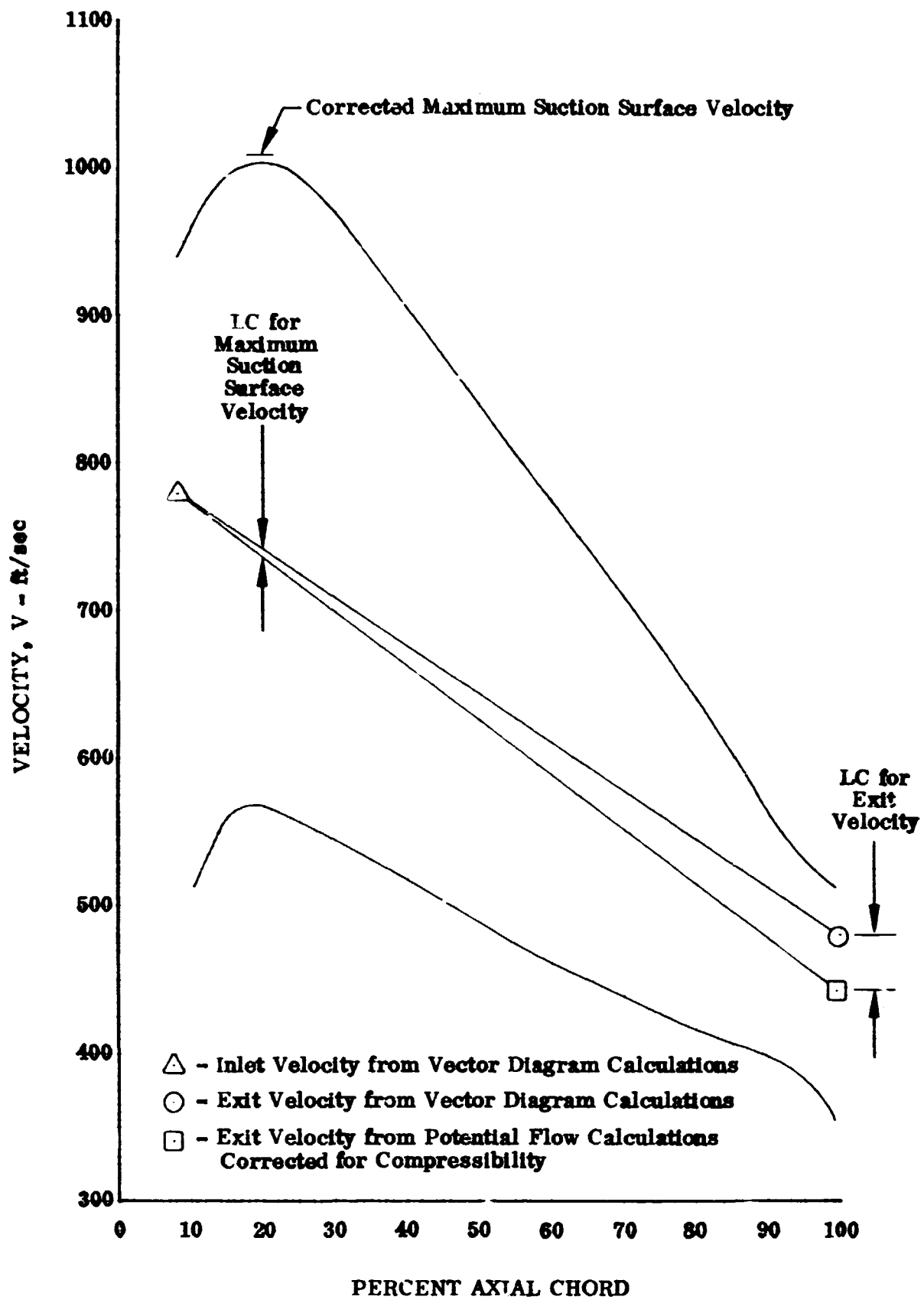


Figure 21. Rotor A Blade Surface Velocities, 95% Span From Tip

DF 90578

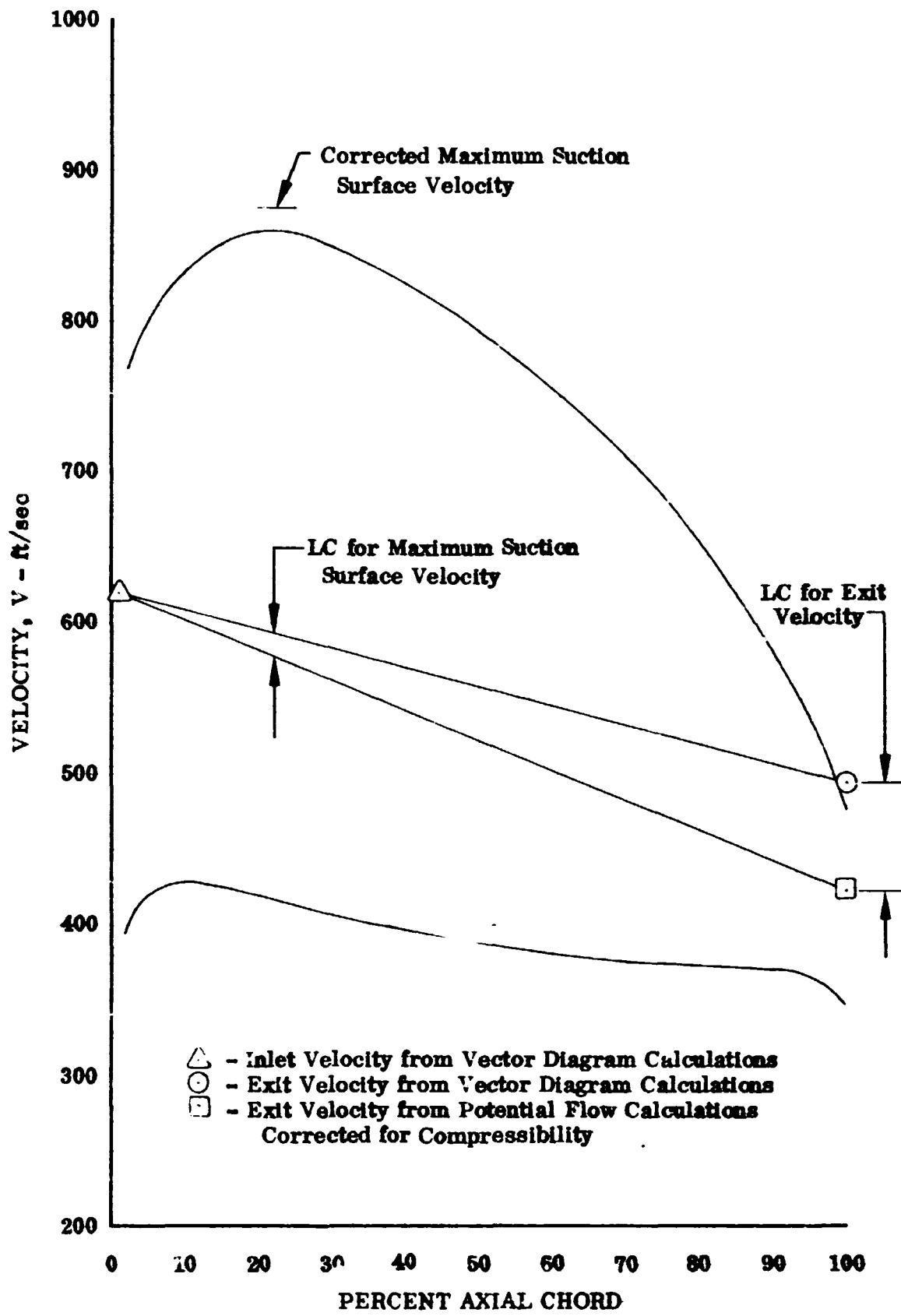


Figure 22. Stator A Vane Surface Velocities, 5% Span From Tip

DF 90579

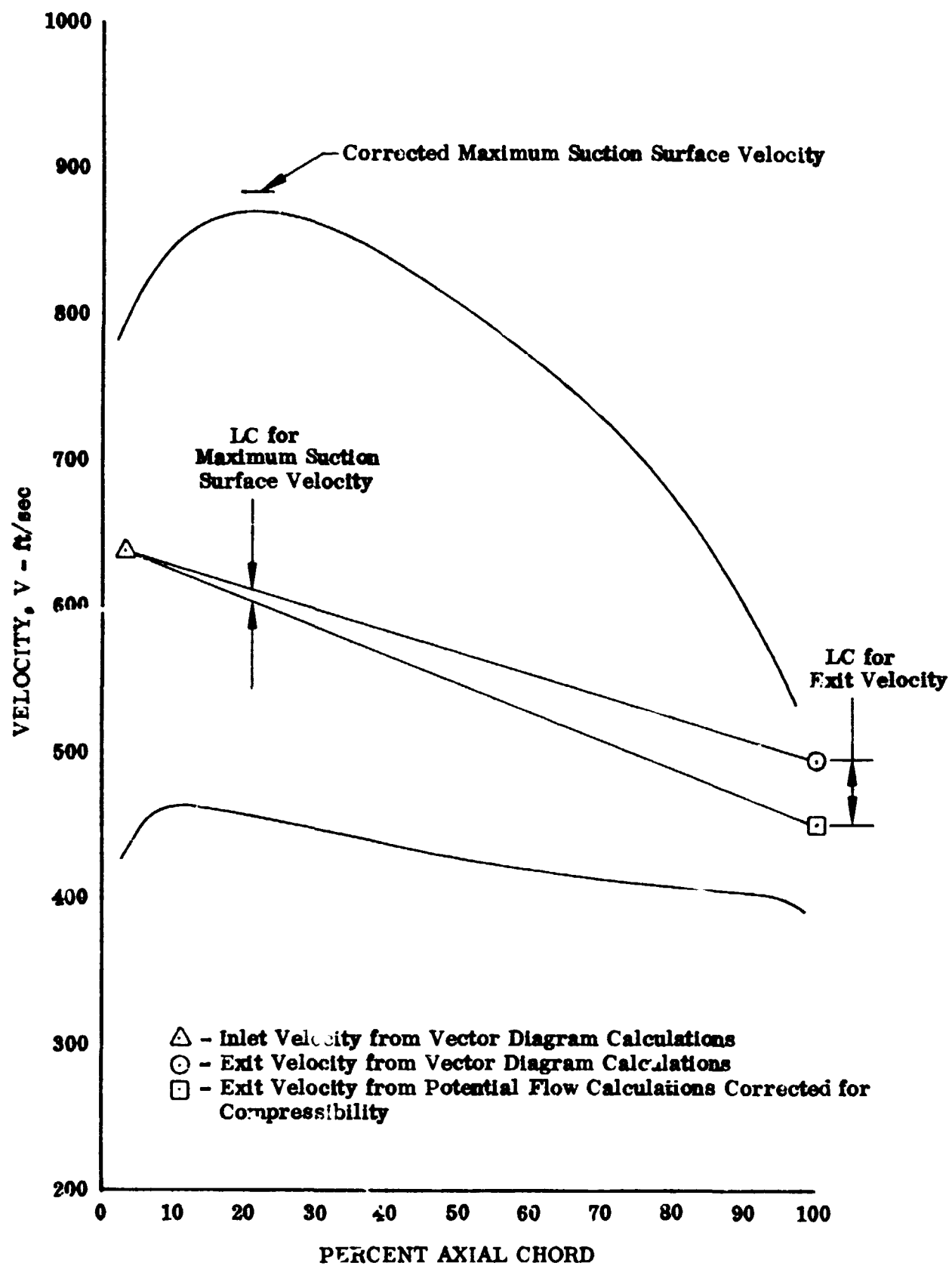


Figure 23. Stator A Vane Surface Velocities, 50% Span

DF 90580

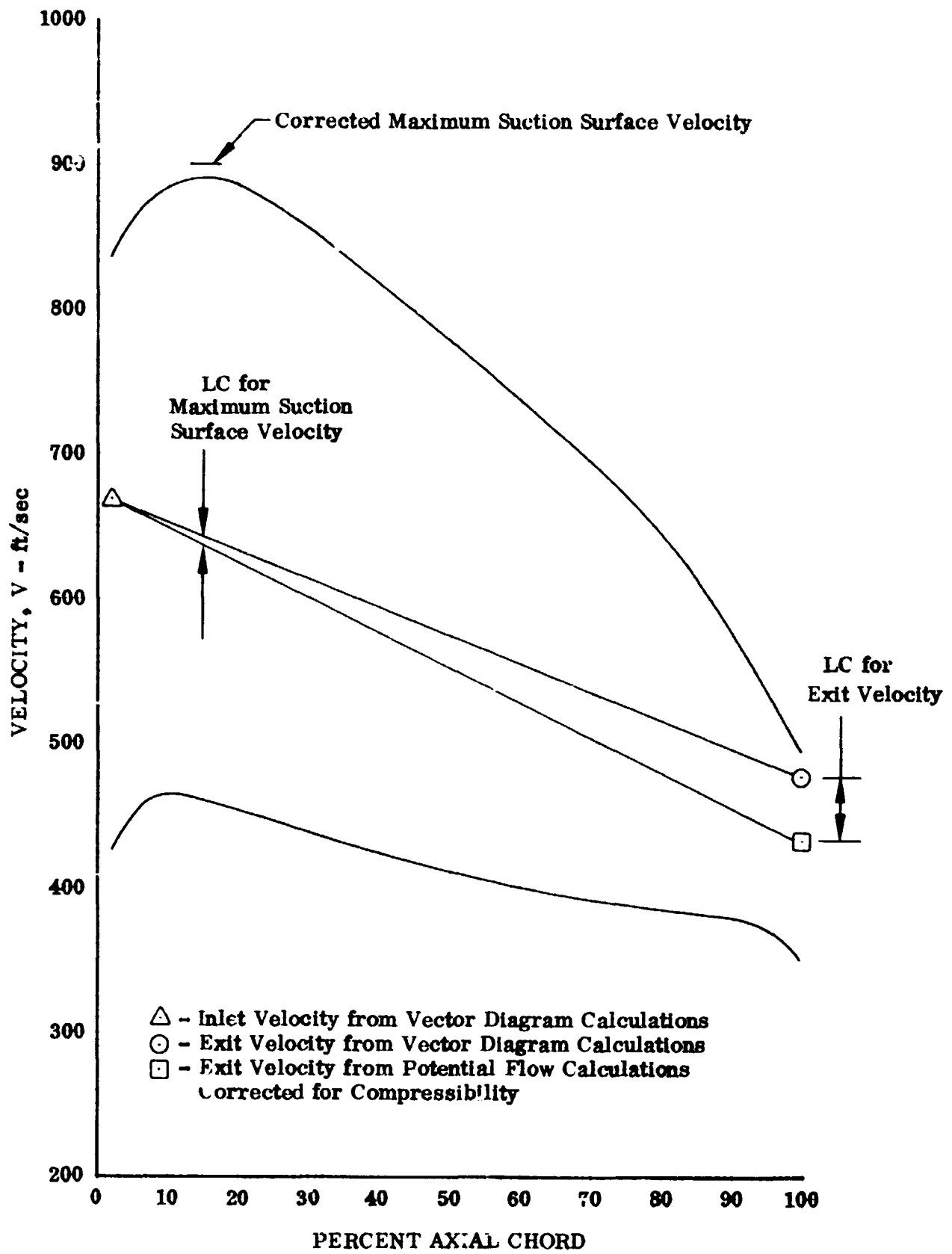
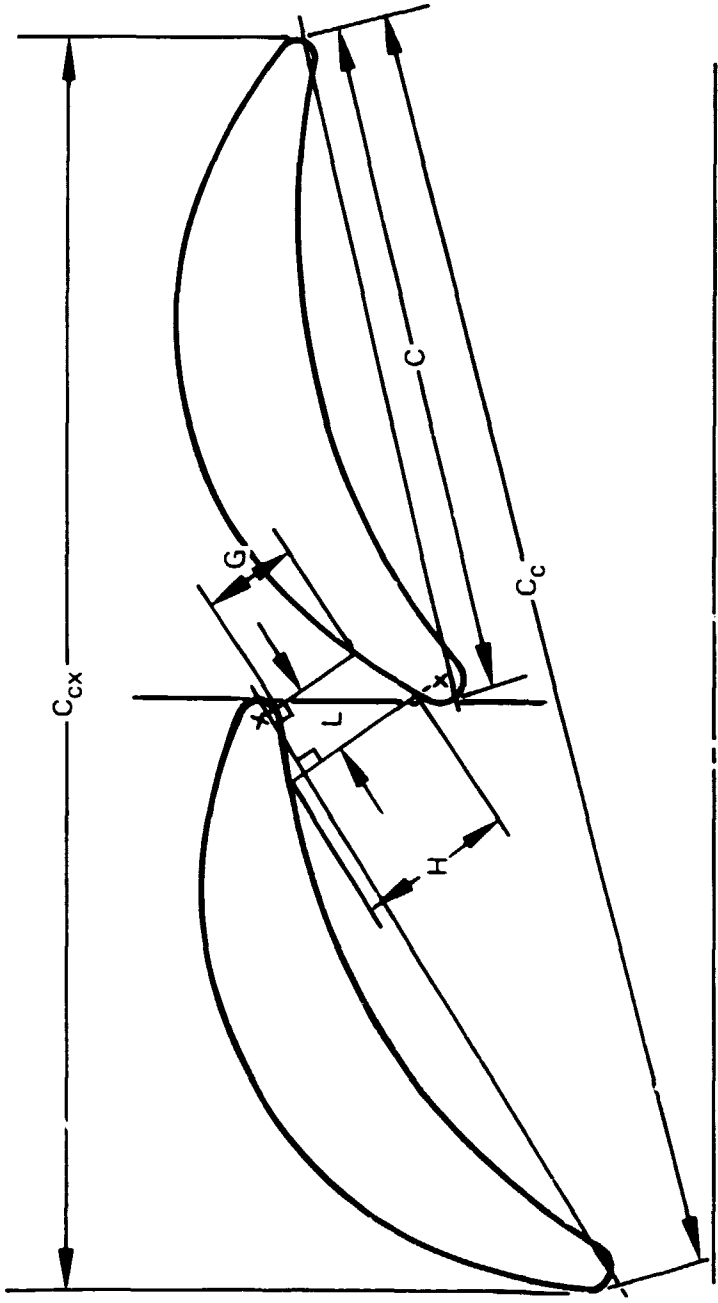


Figure 24. Stator A Vane Surface Velocities, 95% Span From Tip DF 90581



Blade Passage Convergence - $F=H/G$

Blade Passage Gap Ratio - G/C

Blade Passage Overlap Ratio - L/C

C = Individual Airfoil Chord

C_c = Combined or Overall Chord

C_{cx} = Overall Axial Chord

47 Figure 25. Tandem Airfoil Geometry, Circular-Arc Airfoils

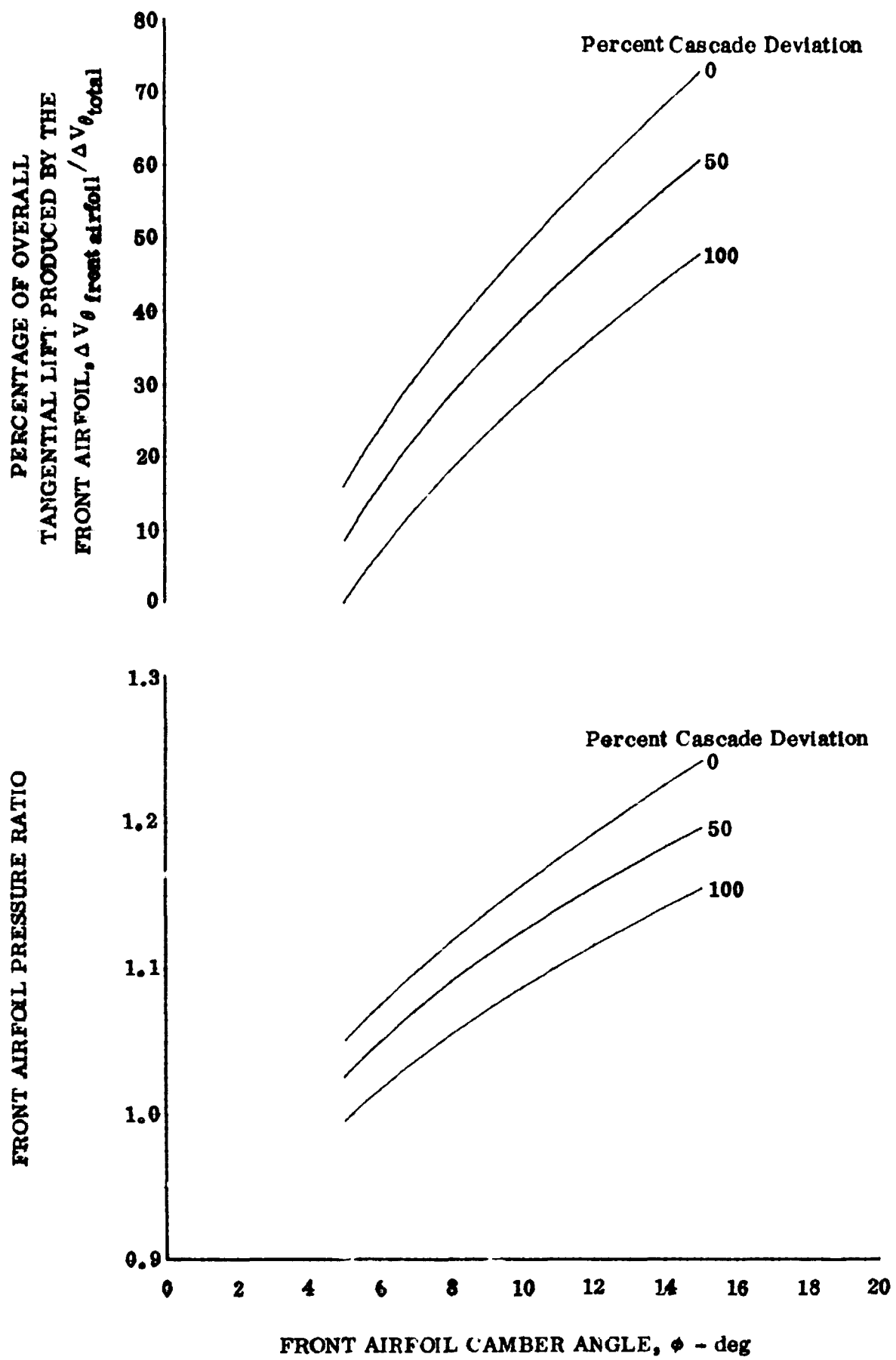


Figure 26. Tandem Rotor Front Airfoil Meanline Analysis

DF 90582

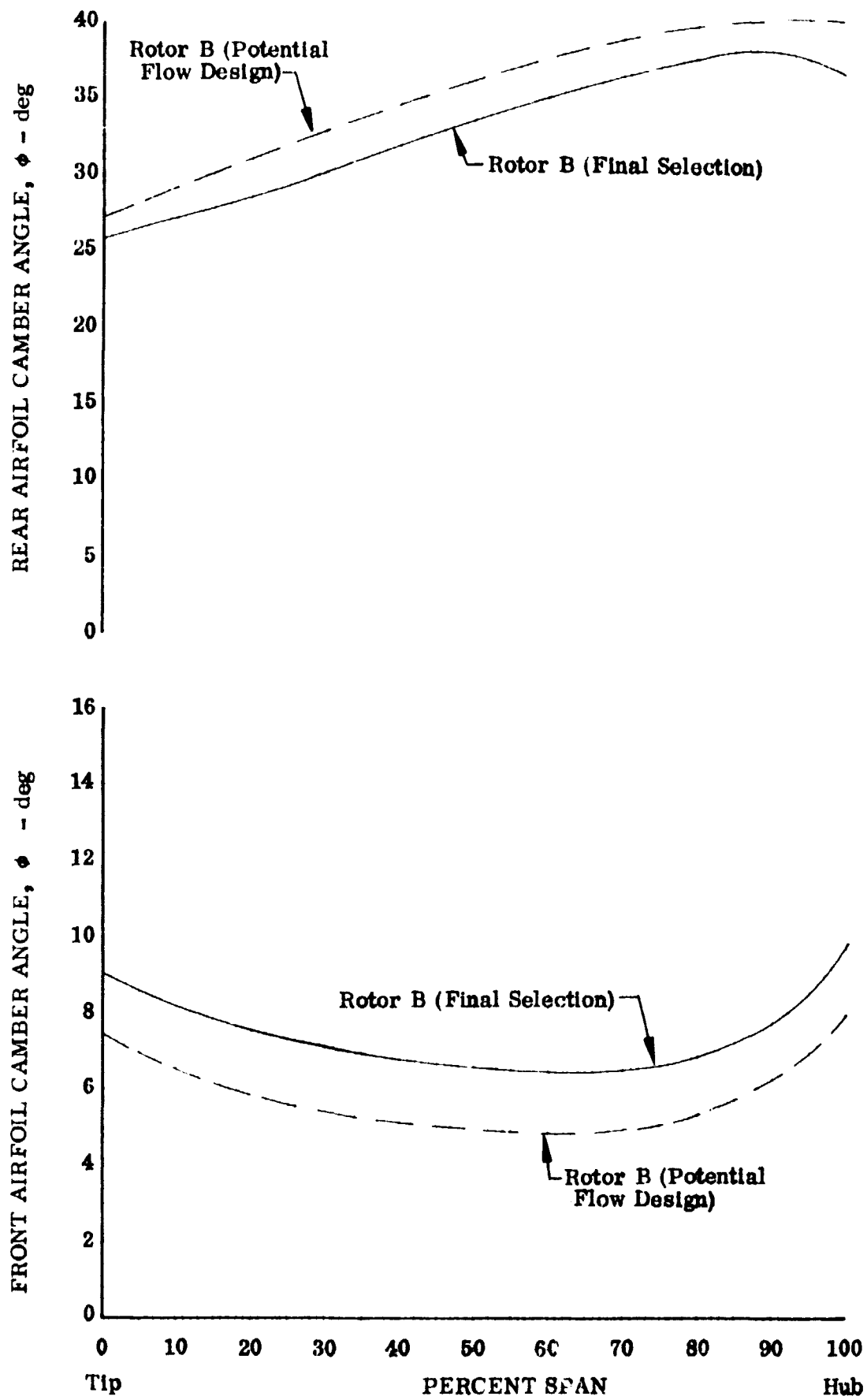


Figure 27. Rotor B Camber Angle Distributions

DF 90583

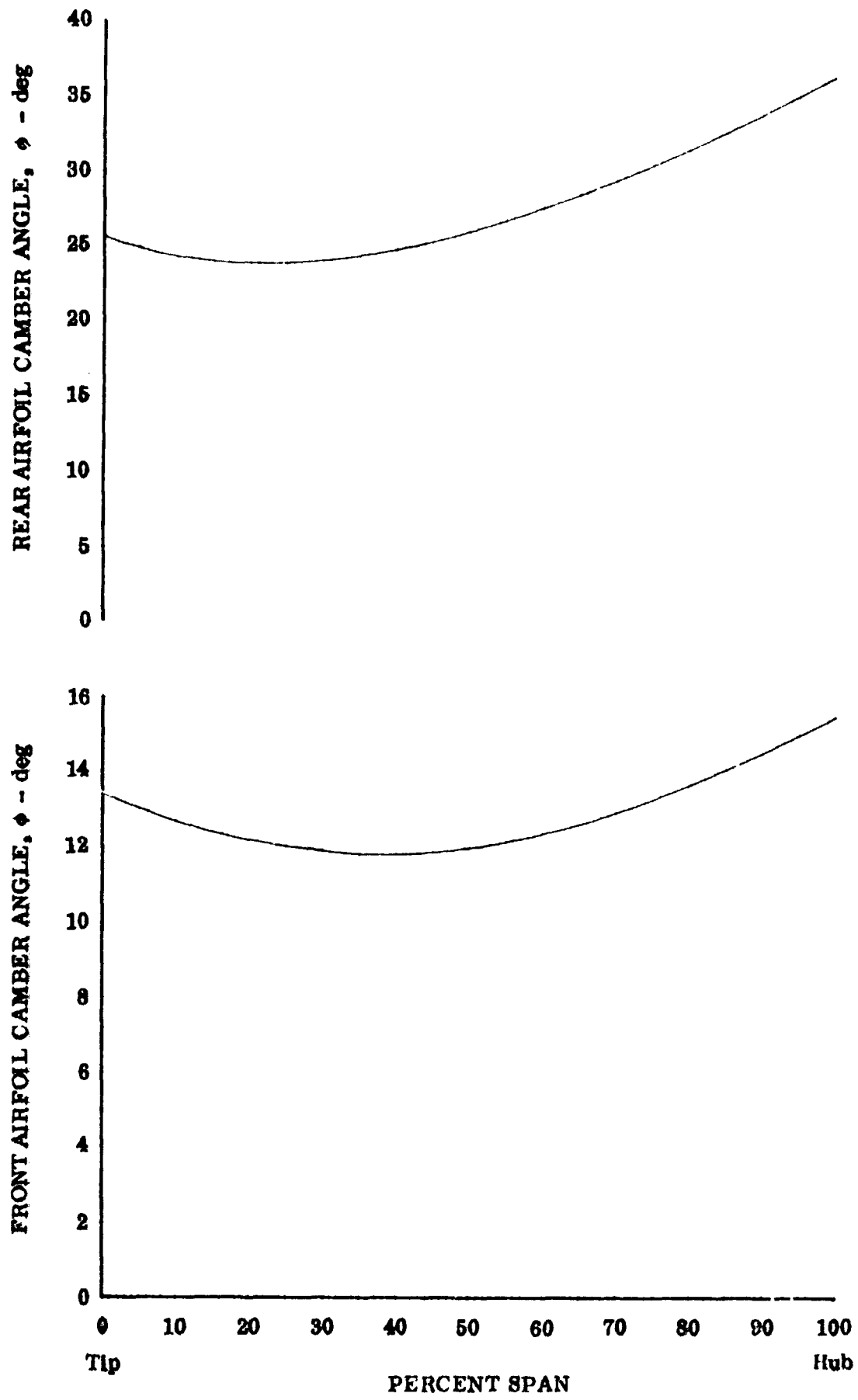


Figure 28. Rotor C Camber Angle Distributions

DF 90584

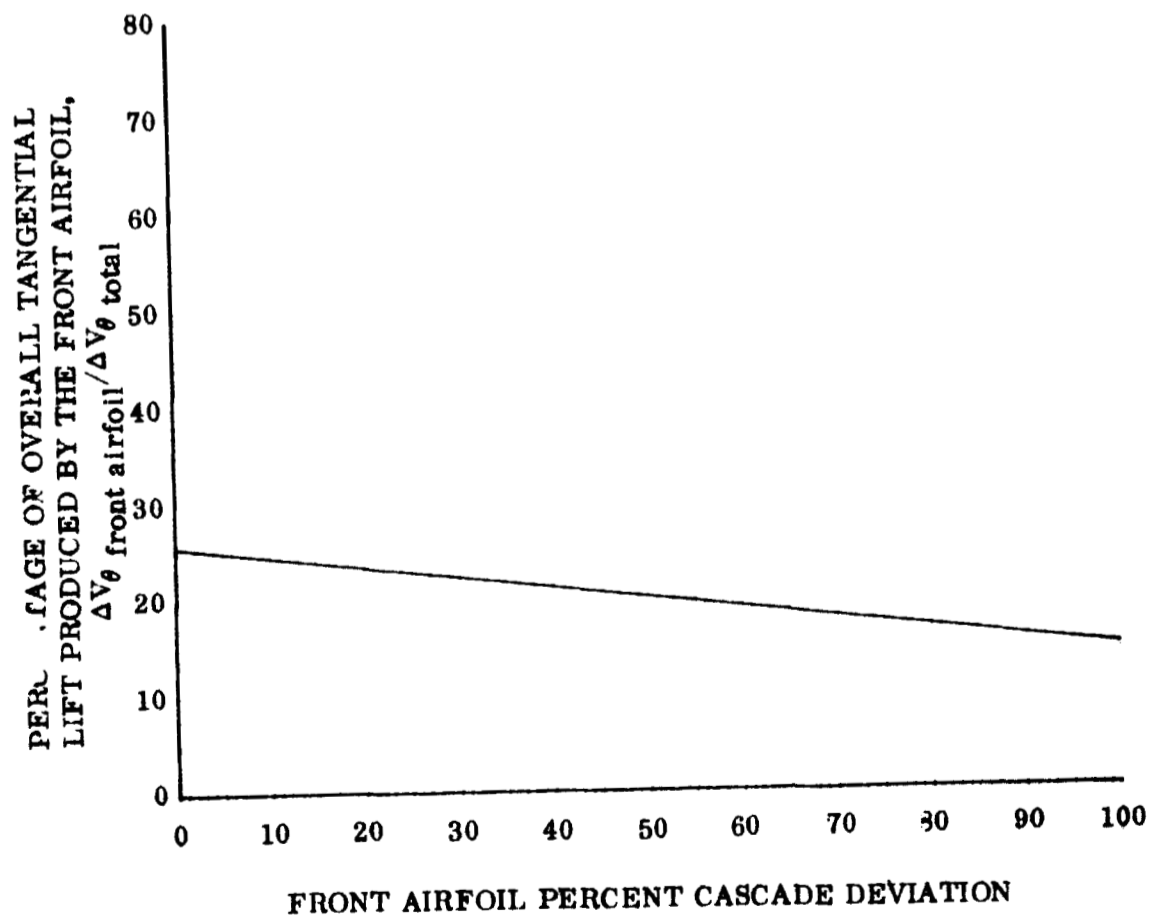


Figure 29. Stator B Front Airfoil Loading Split

DF 90585

22

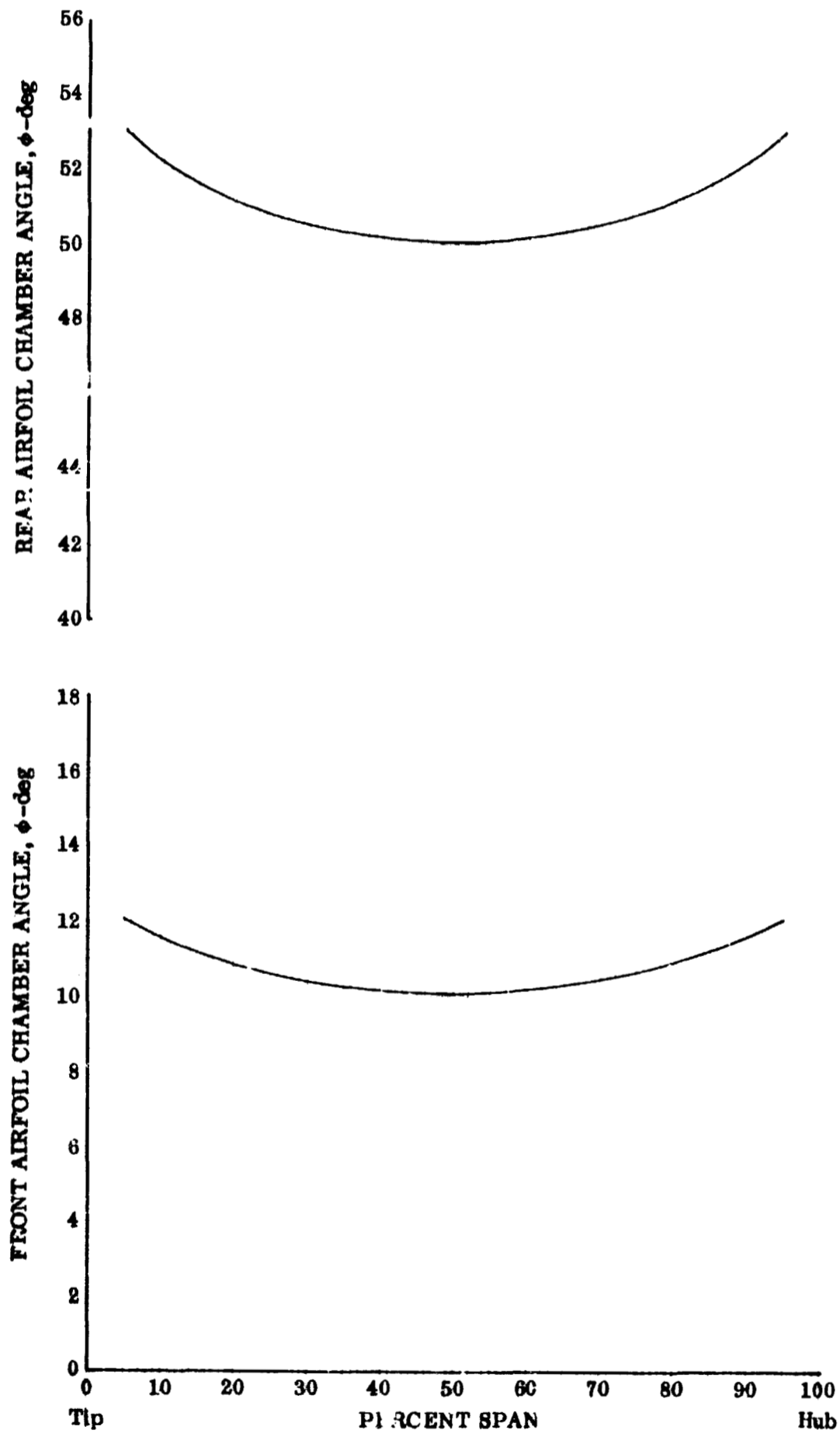


Figure 30. Stator B Camber Angle Distribution

DF 90630

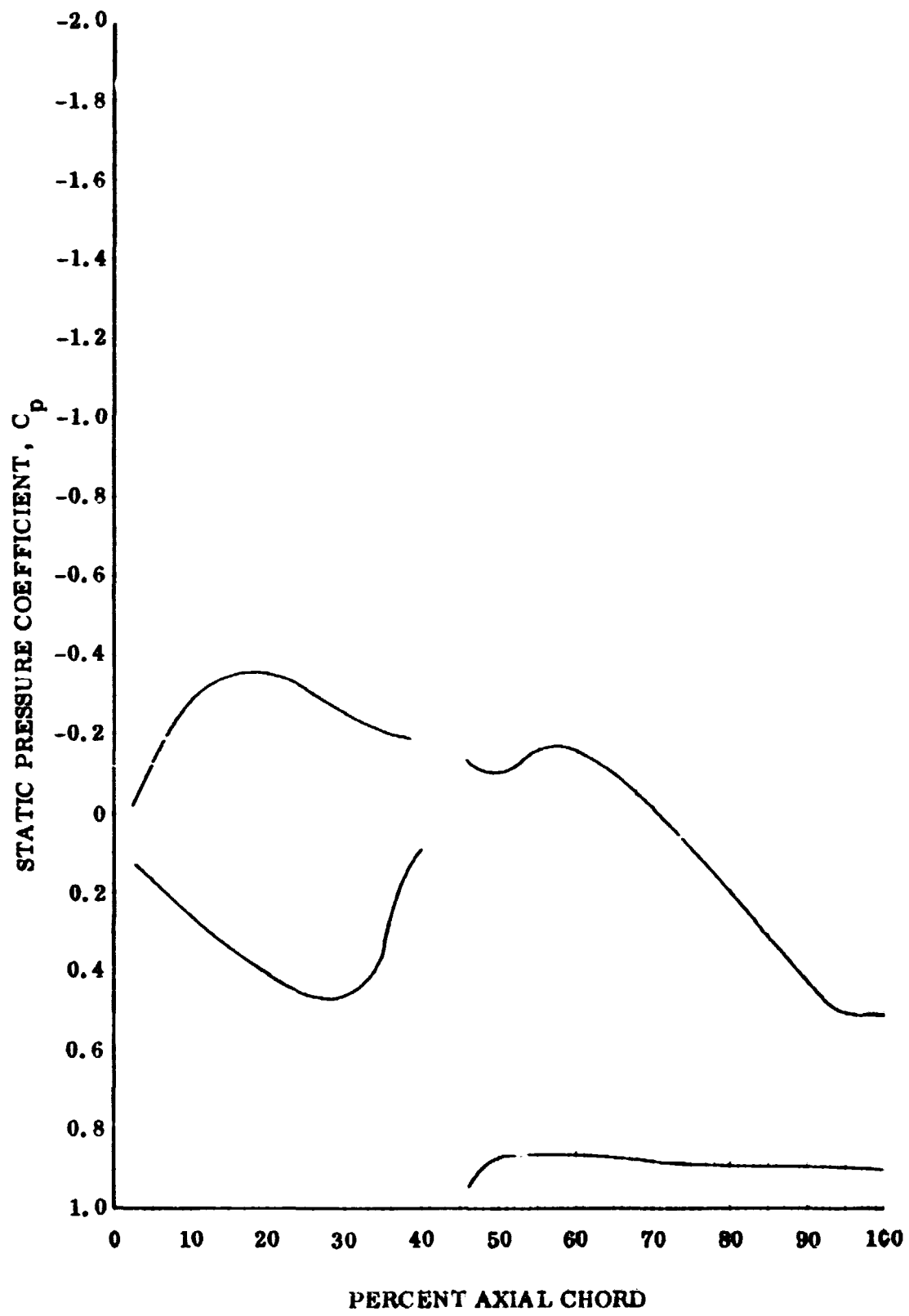


Figure 31. Rotor B Static Pressure Coefficient, 5% Span From Tip DF 90586

02

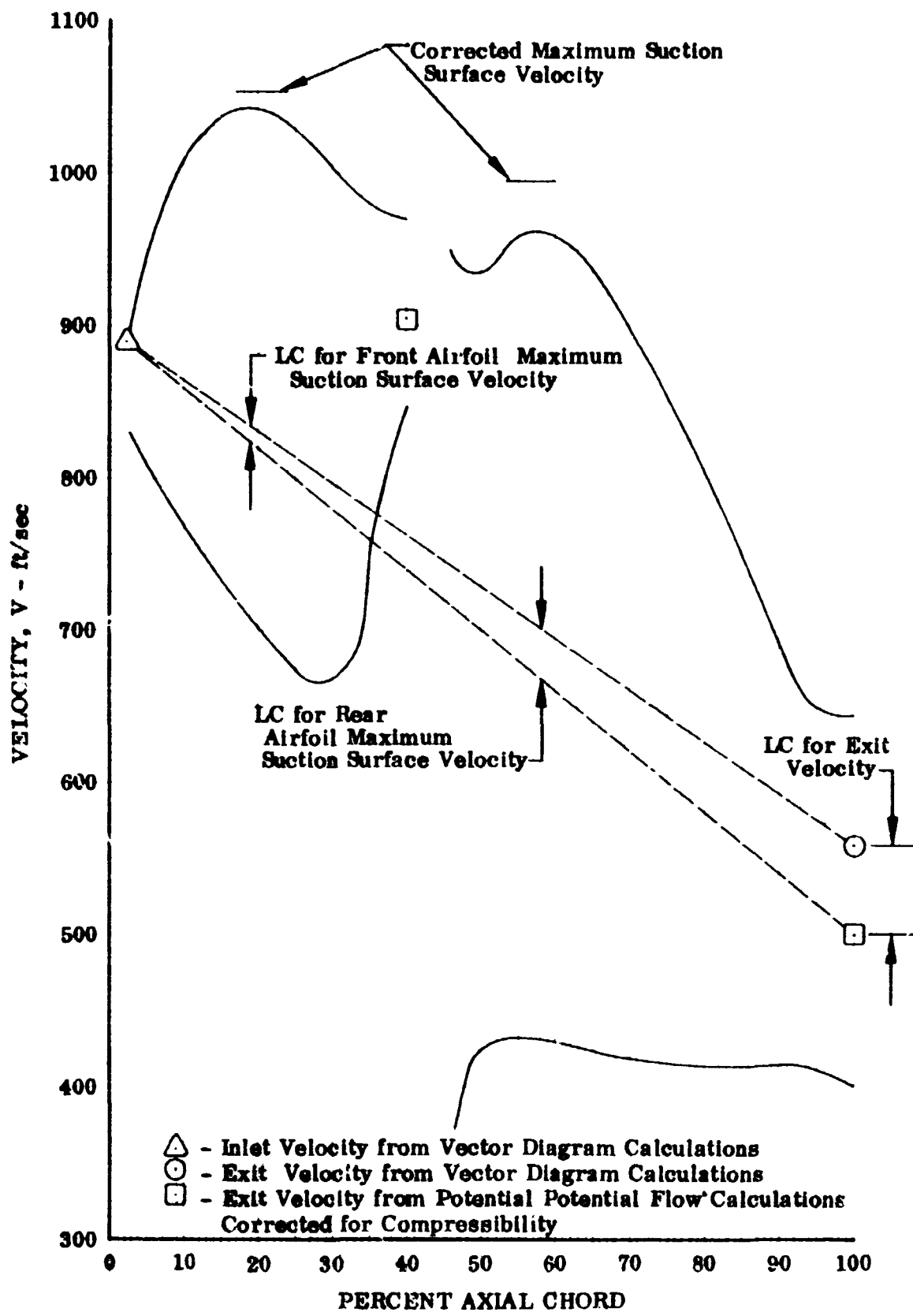


Figure 32. Rotor B Blade Surface Velocities, 5% Span From Tip

DF 90587

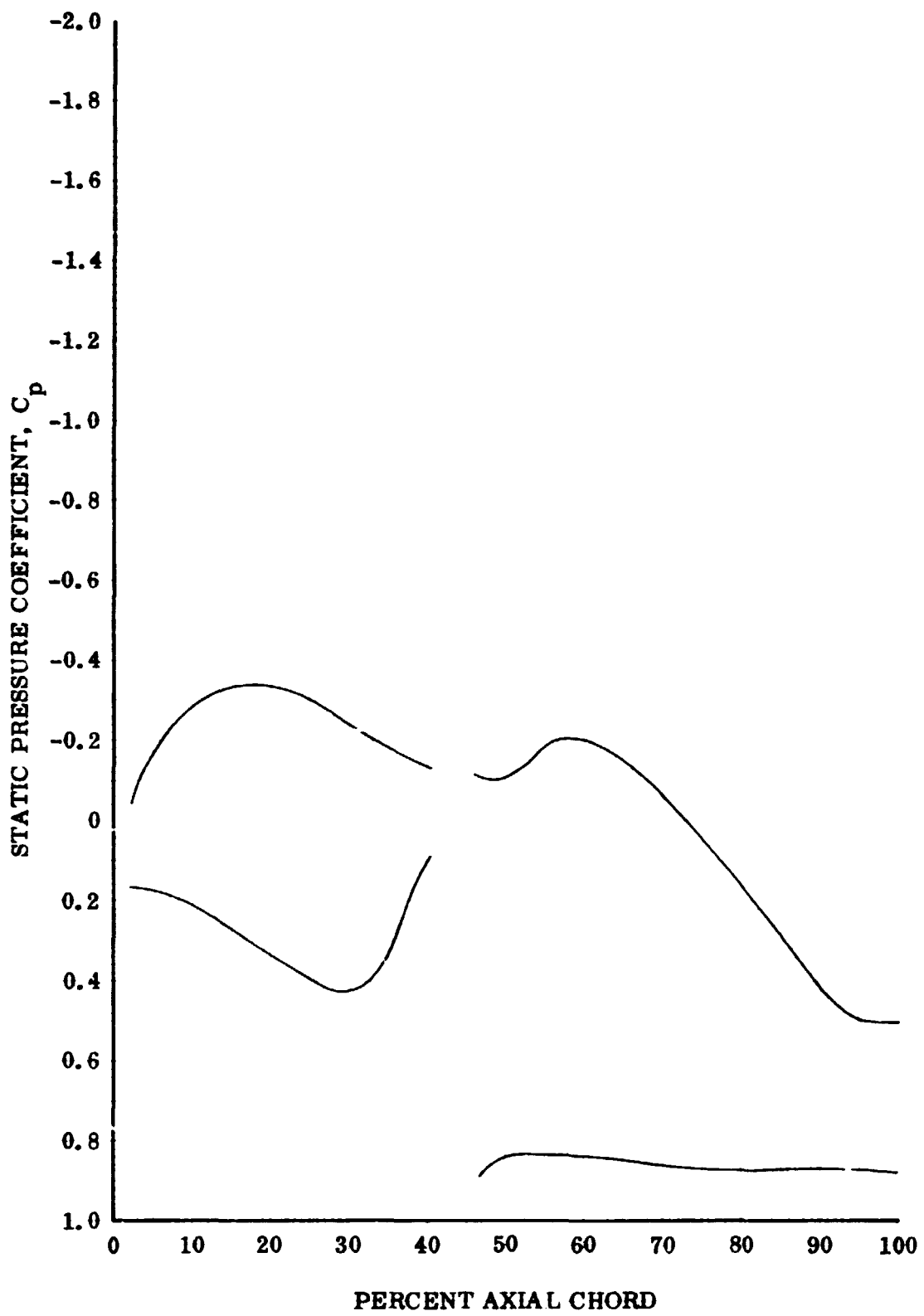


Figure 33. Rotor B Static Pressure Coefficient, 25% Span From Tip DF 90588

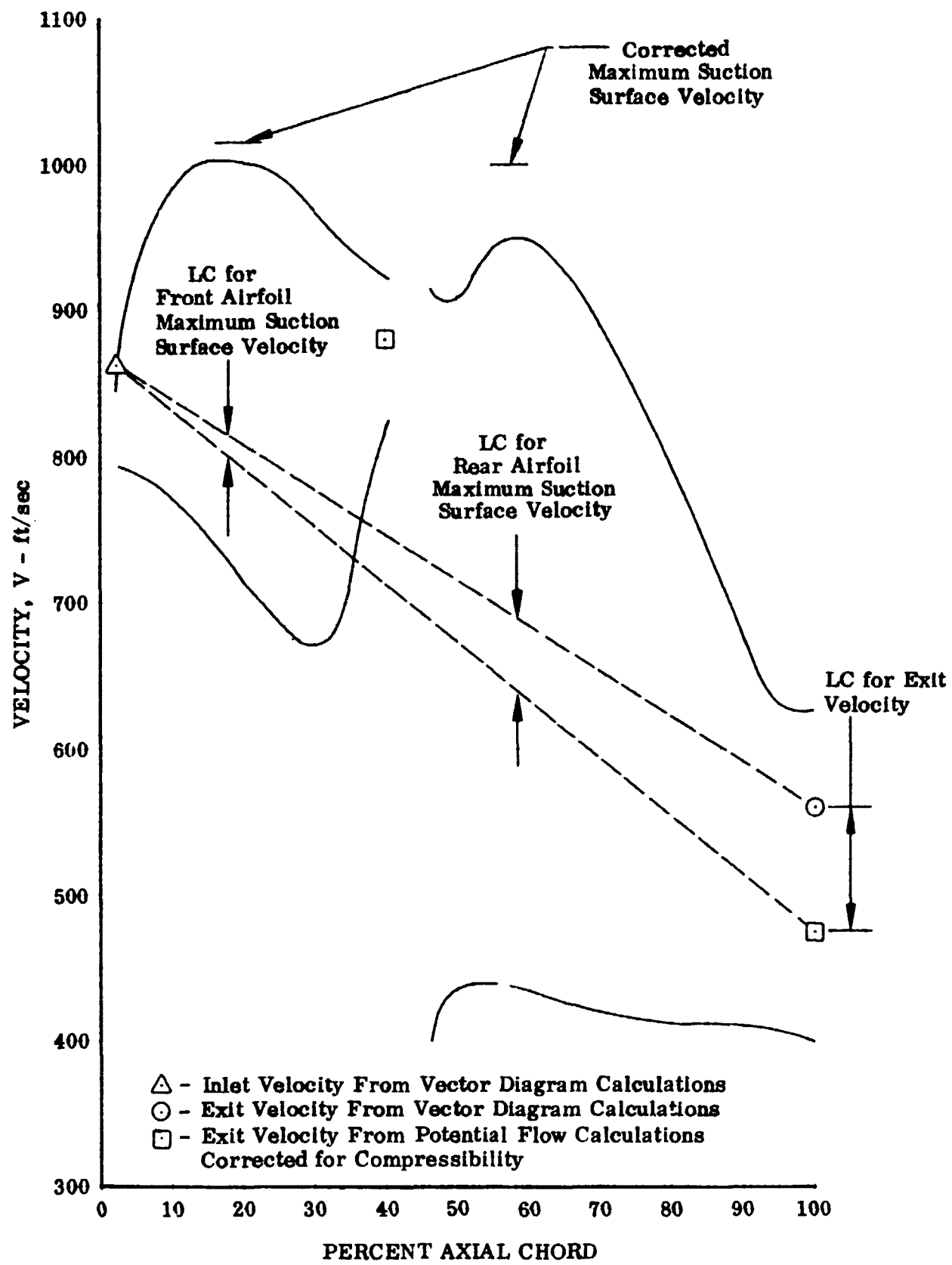


Figure 34. Rotor B Blade Surface Velocities, 25% Span From Tip

DF 90589

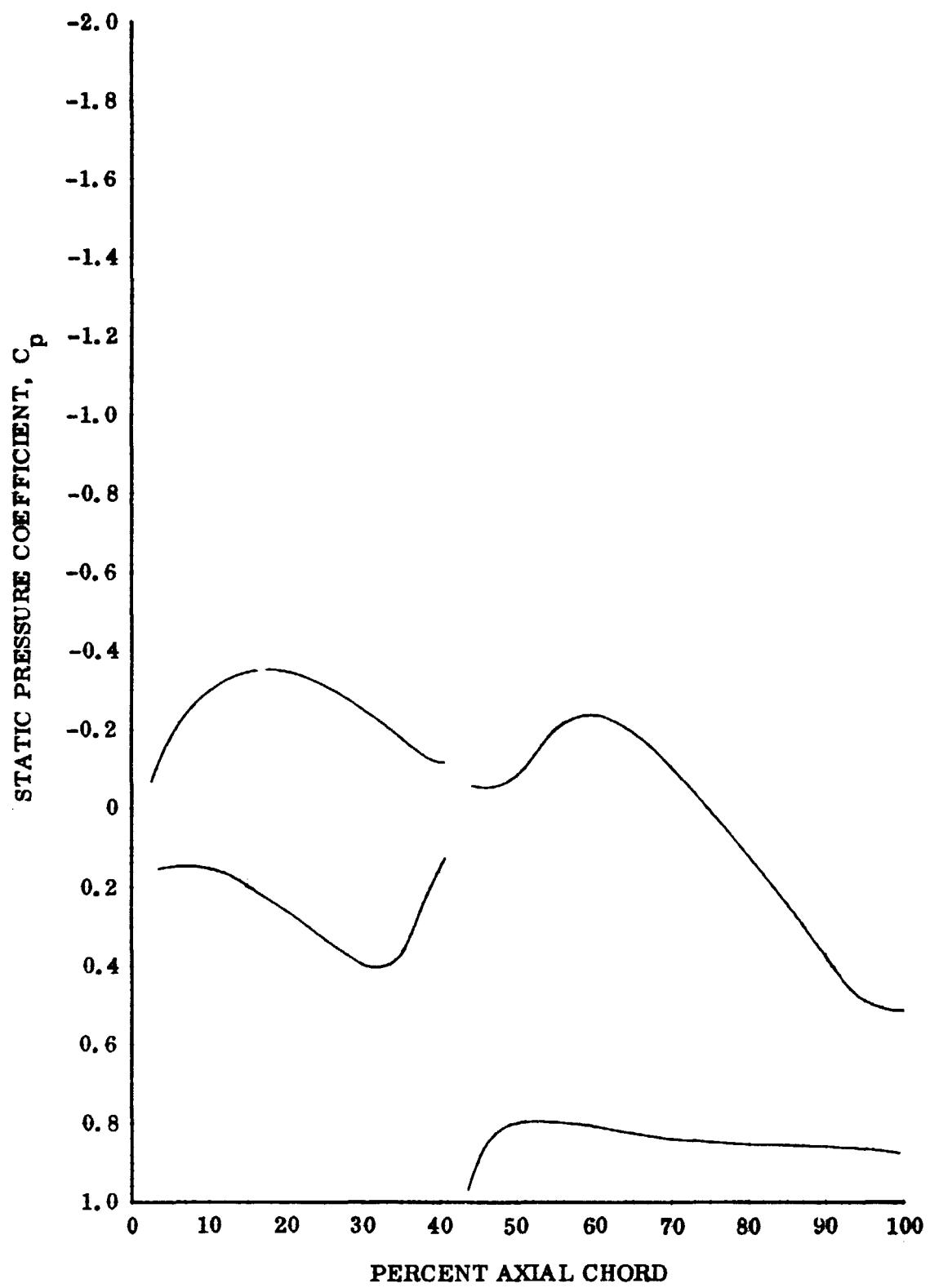


Figure 35. Rotor B Static Pressure Coefficient,
50% Span

DF 90590

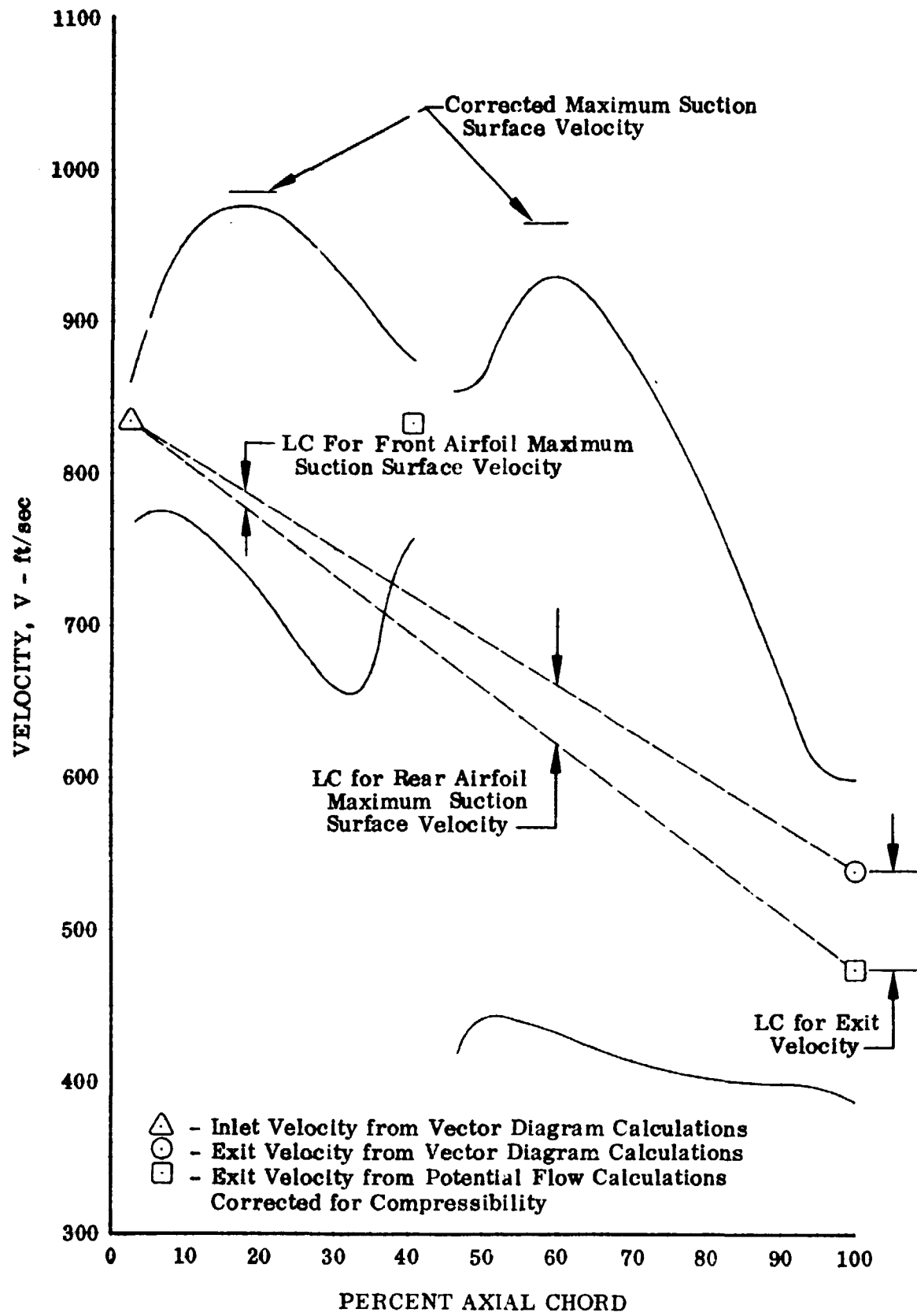


Figure 36. Rotor B Blade Surface Velocities, 50% Span

DF 90591

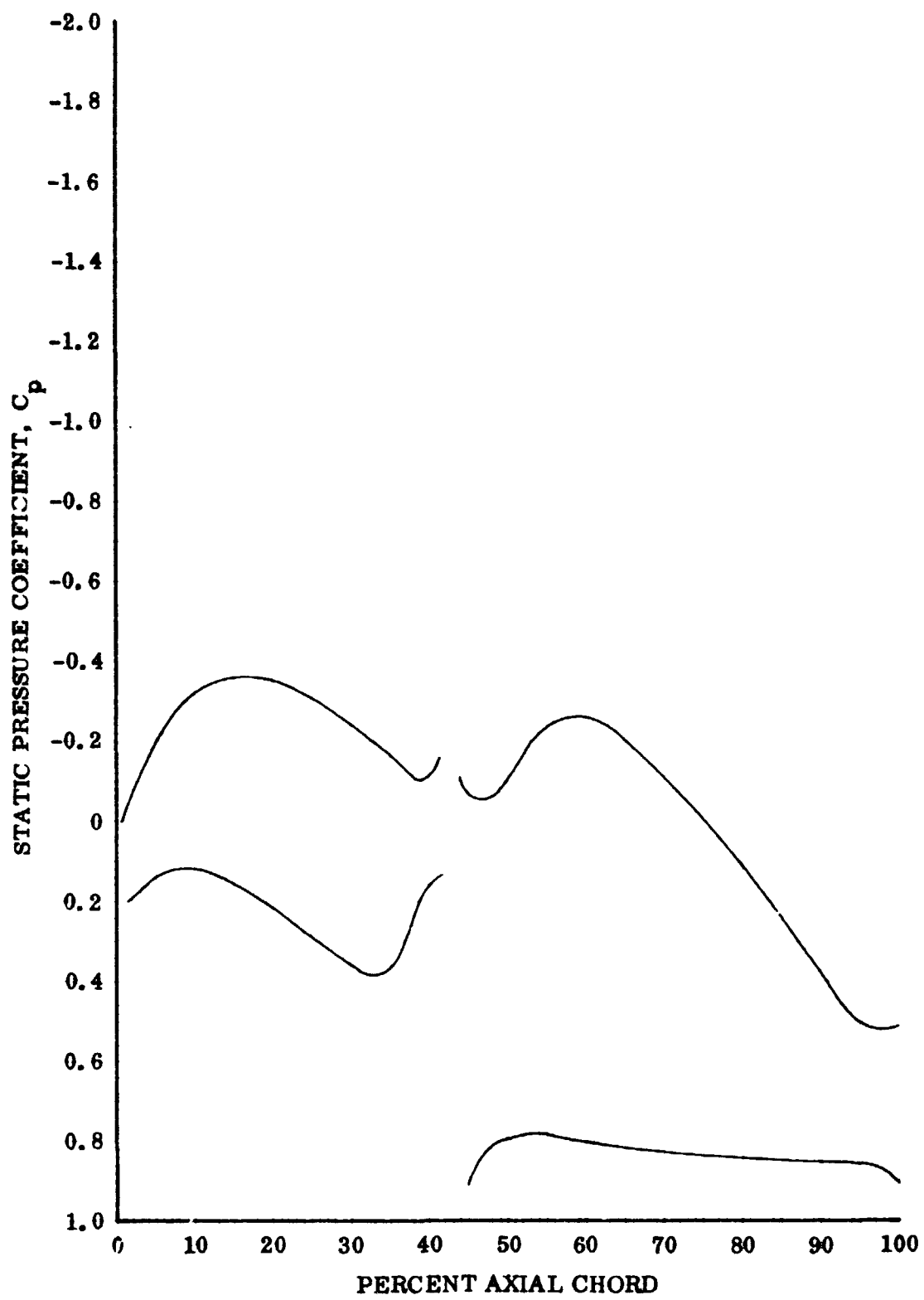


Figure 37. Rotor B Static Pressure Coefficient, 75% Span From Tip DF 90592

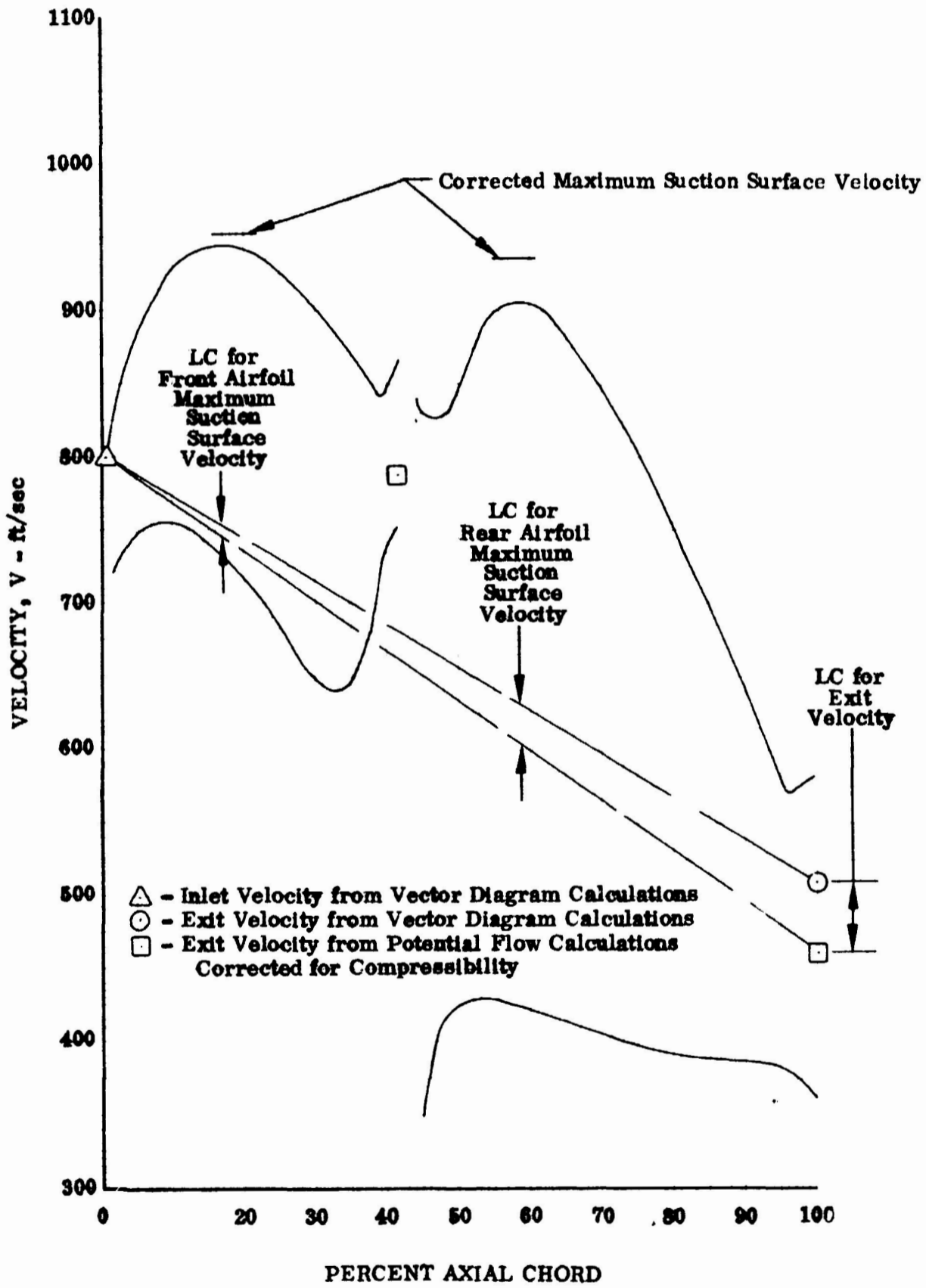


Figure 38. Rotor B Blade Surface Velocities, 75% Span From Tip

DF 90593

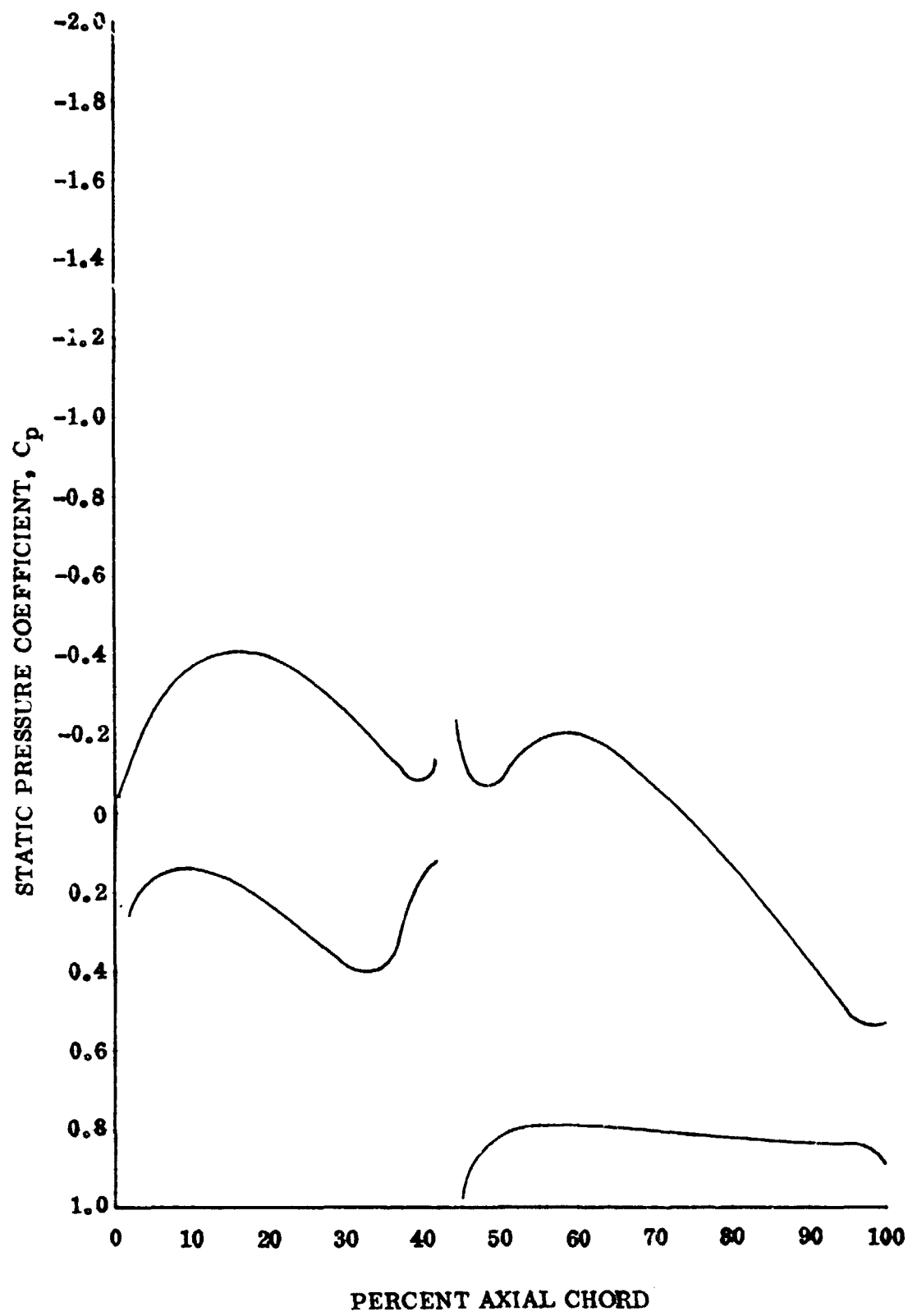


Figure 39. Rotor B Static Pressure Coefficient, 95% Span From Tip DF 90594

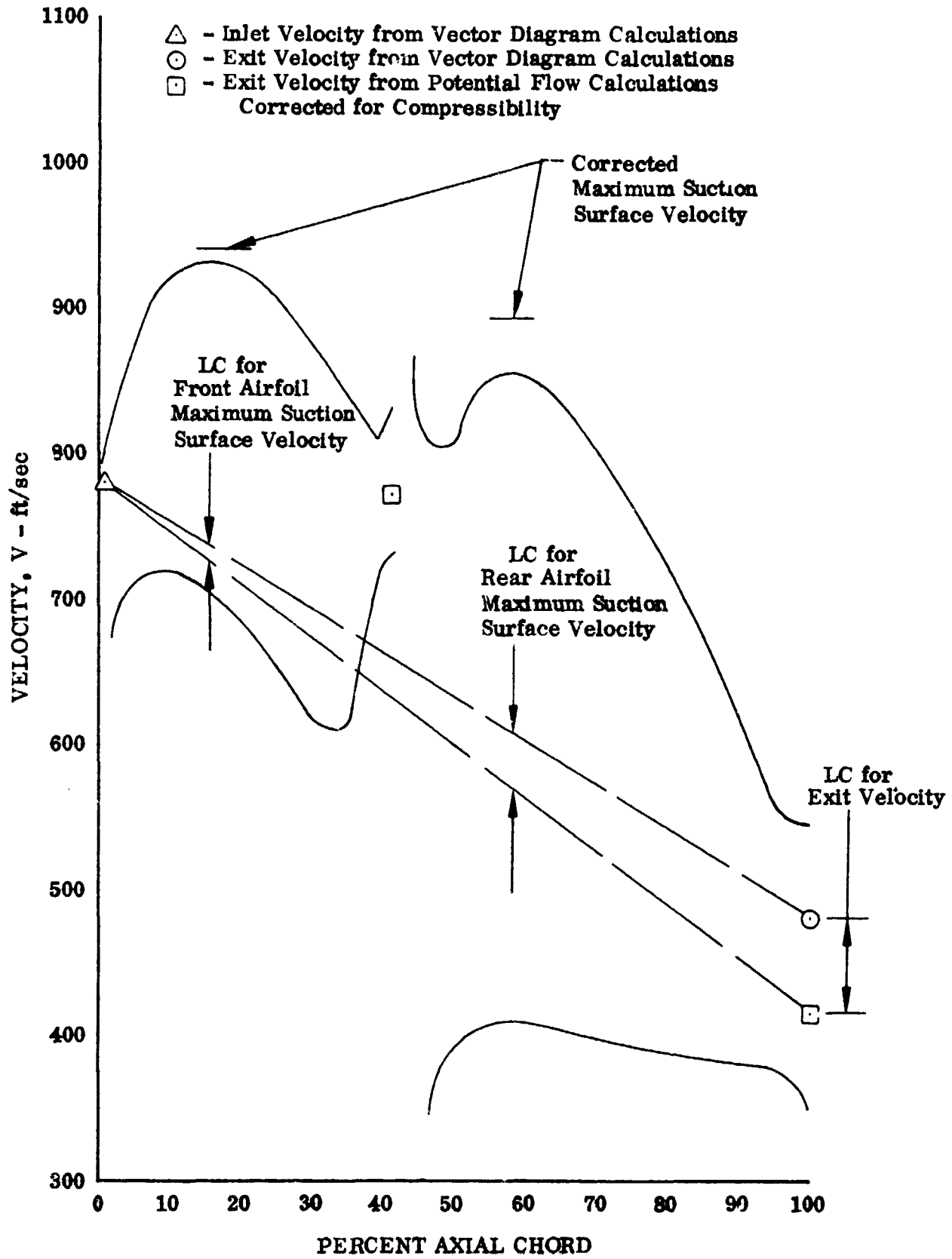


Figure 40. Rotor B Blade Surface Velocities, 95% Span From Tip

DF 90595

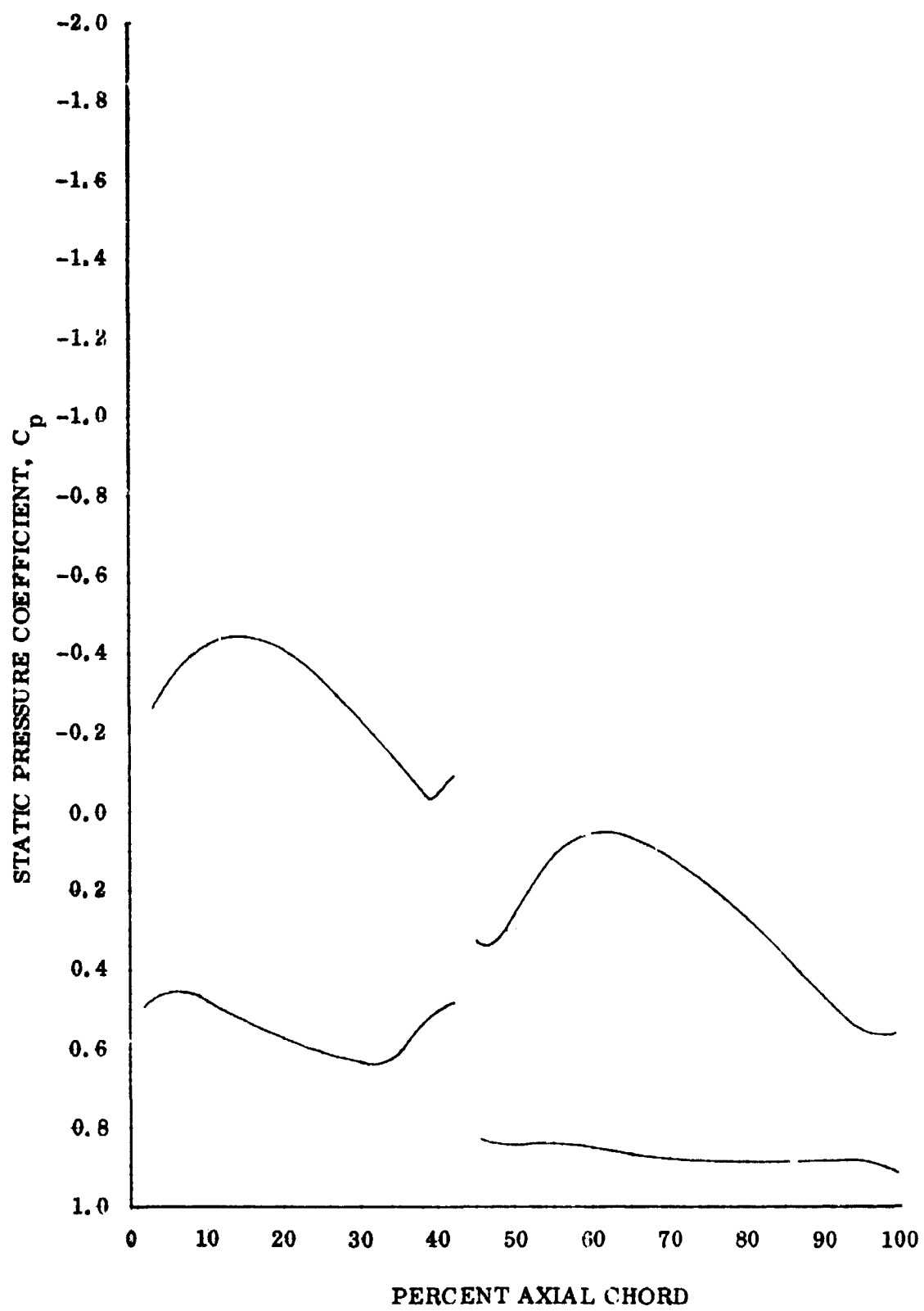


Figure 41. Rotor C Static Pressure Coefficient, 5% Span From Tip DF 90596

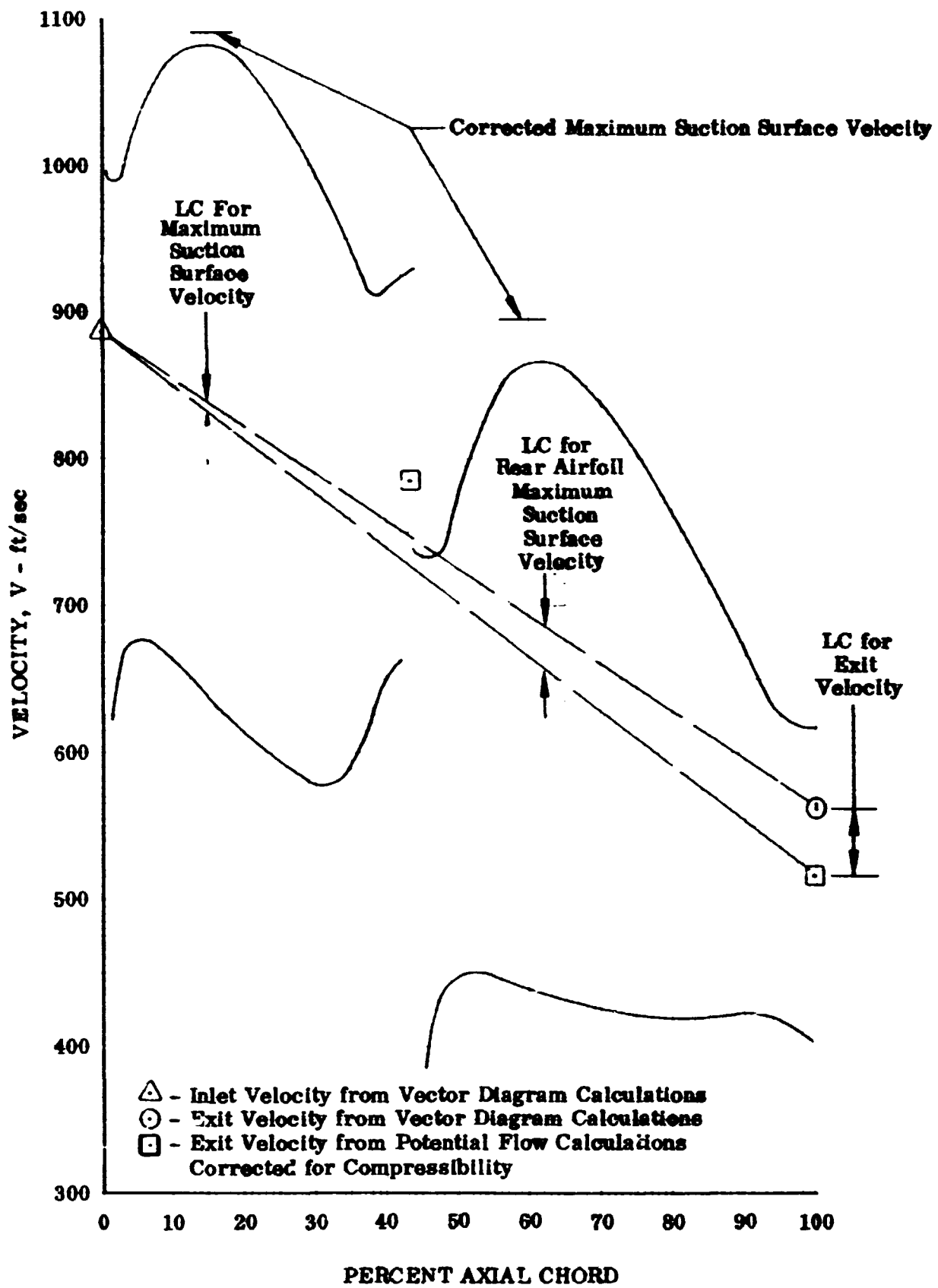


Figure 42. Rotor C Blade Surface Velocities, 5% Span From Tip

DF 90597

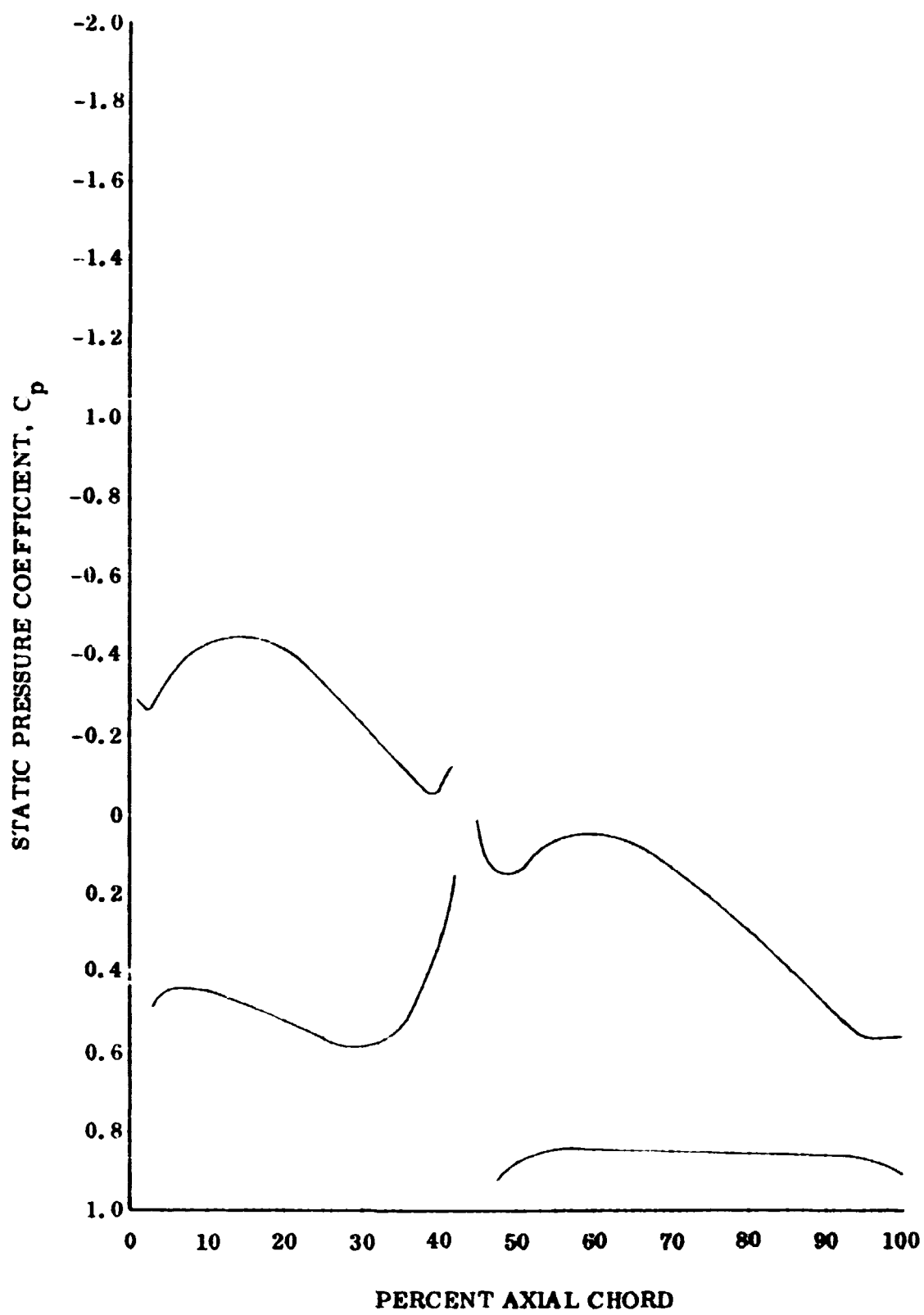


Figure 43. Rotor C Static Pressure Coefficient, 25% Span From Tip DF 90598

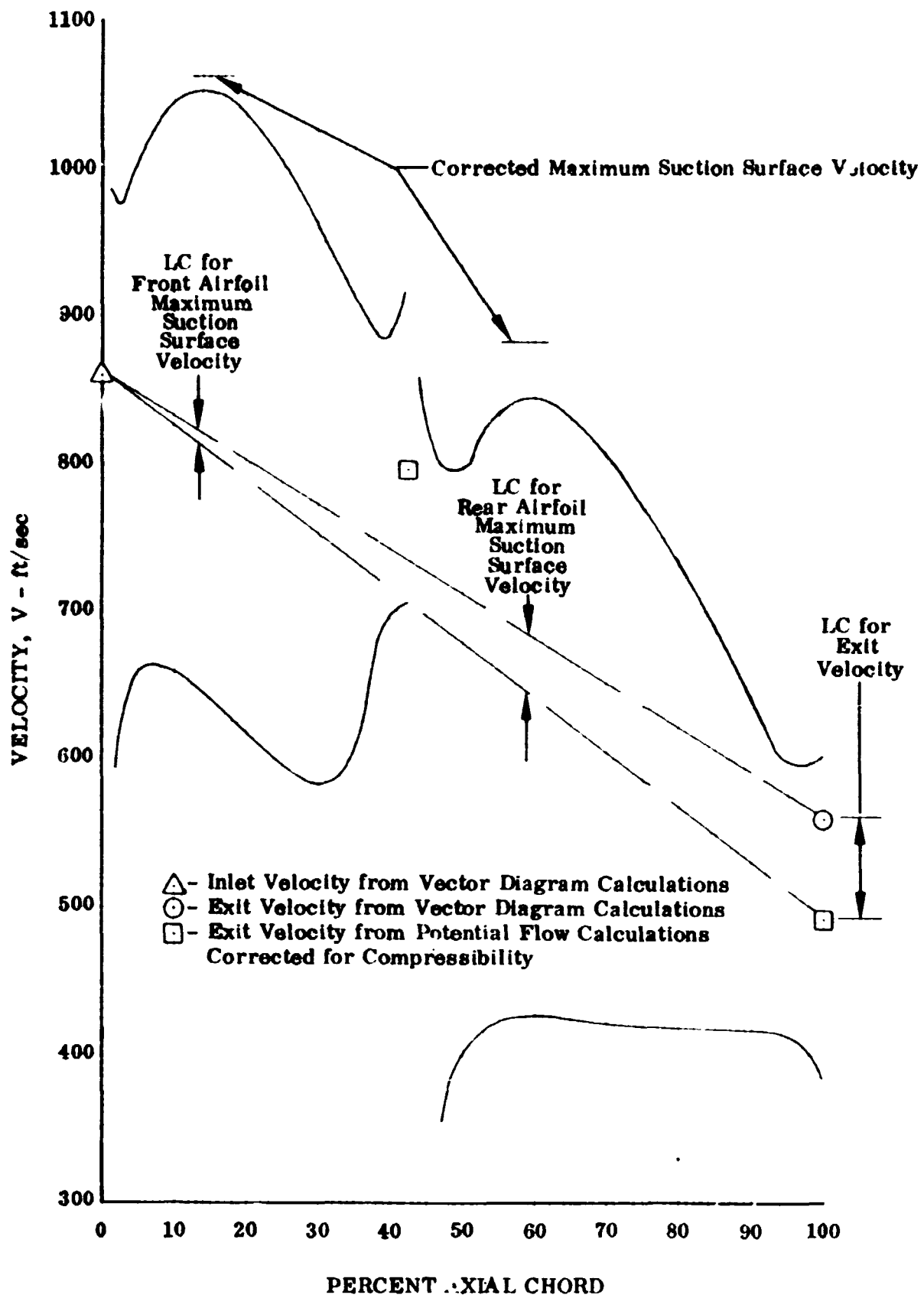


Figure 44. Rotor C Blade Surface Velocities, 25% Span From Tip

DF 90599

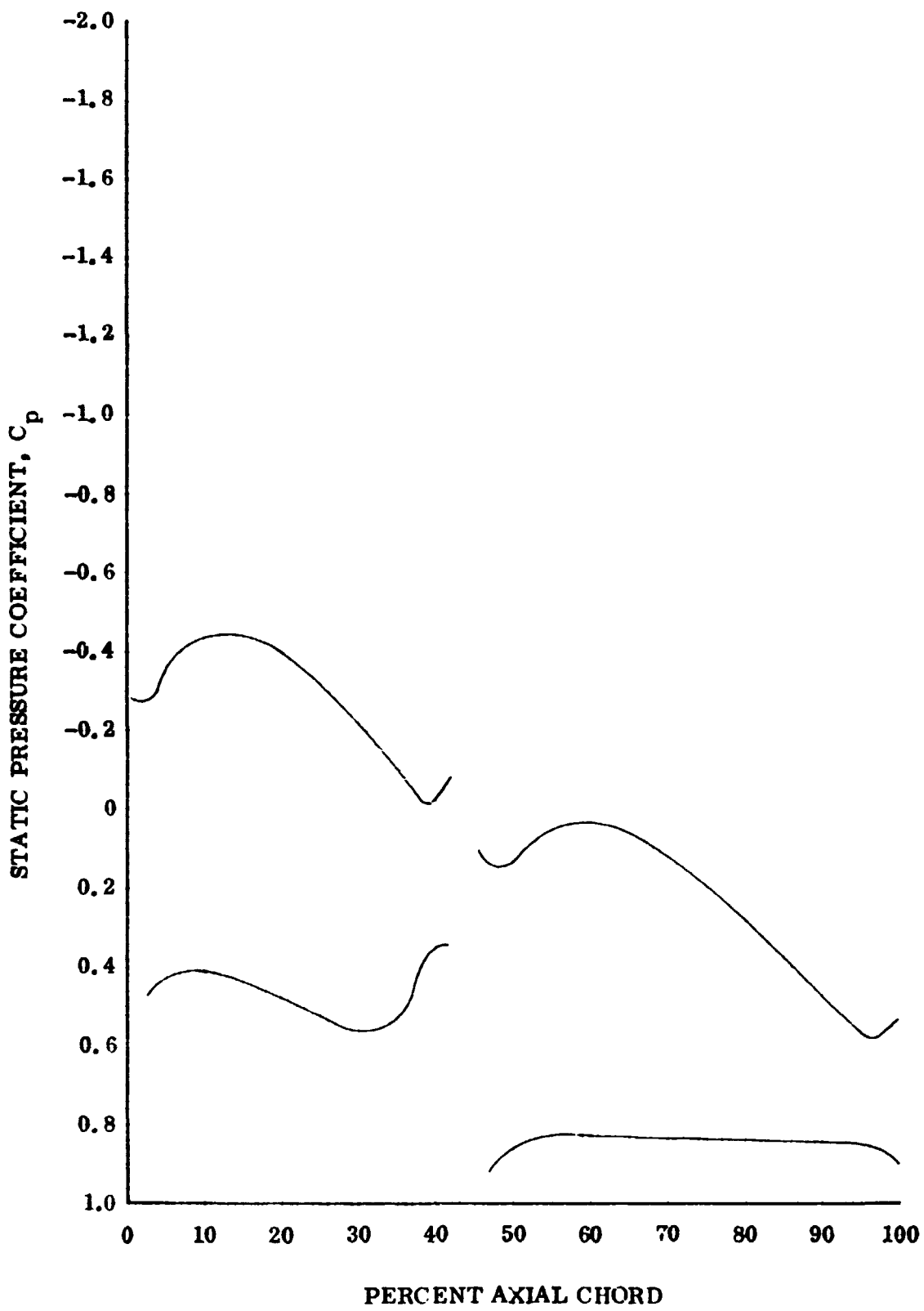


Figure 45. Rotor C Static Pressure Coefficient, 50% Span DF 90600

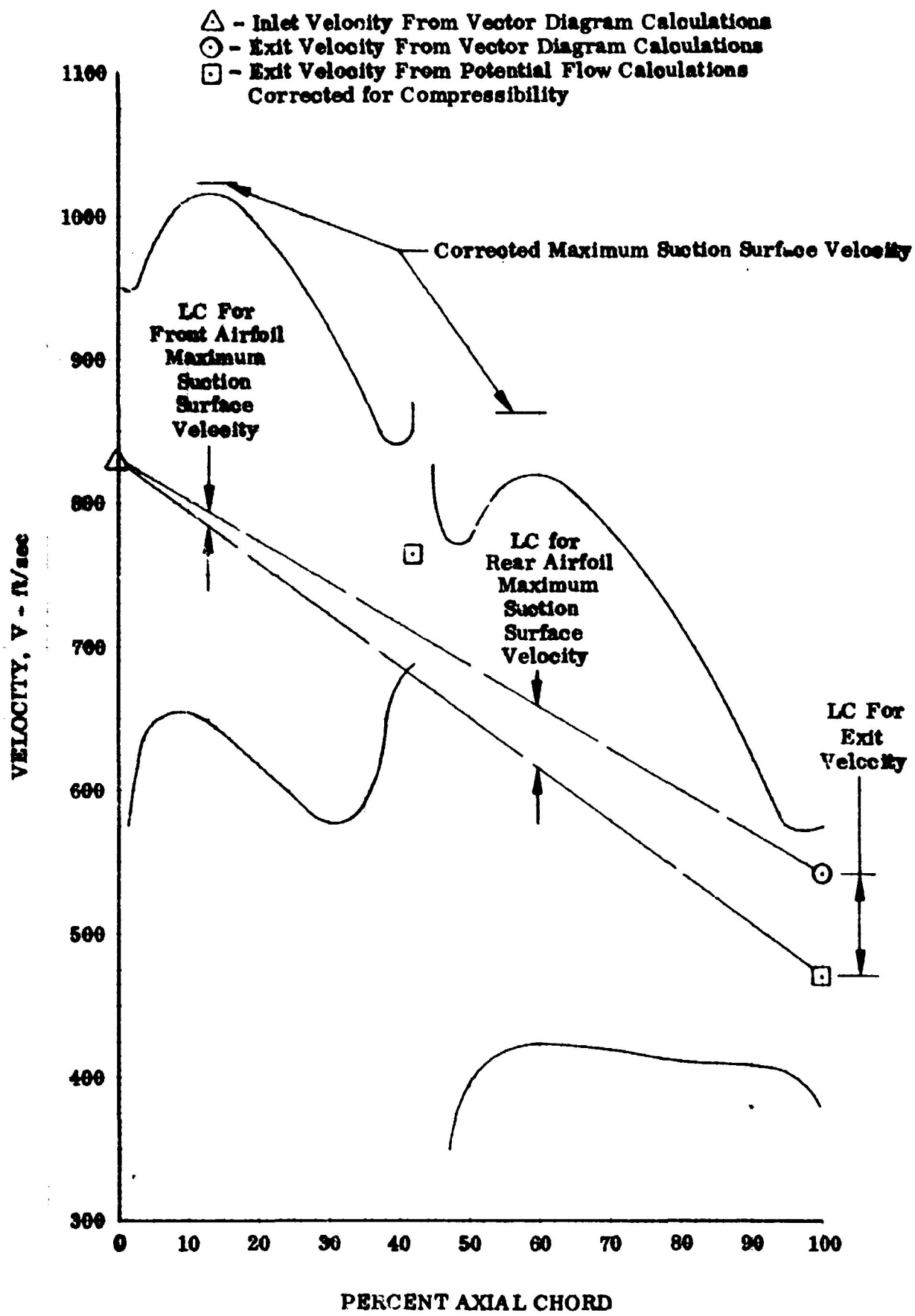


Figure 46. Rotor C Blade Surface Velocities, 50% Span

DF 90601

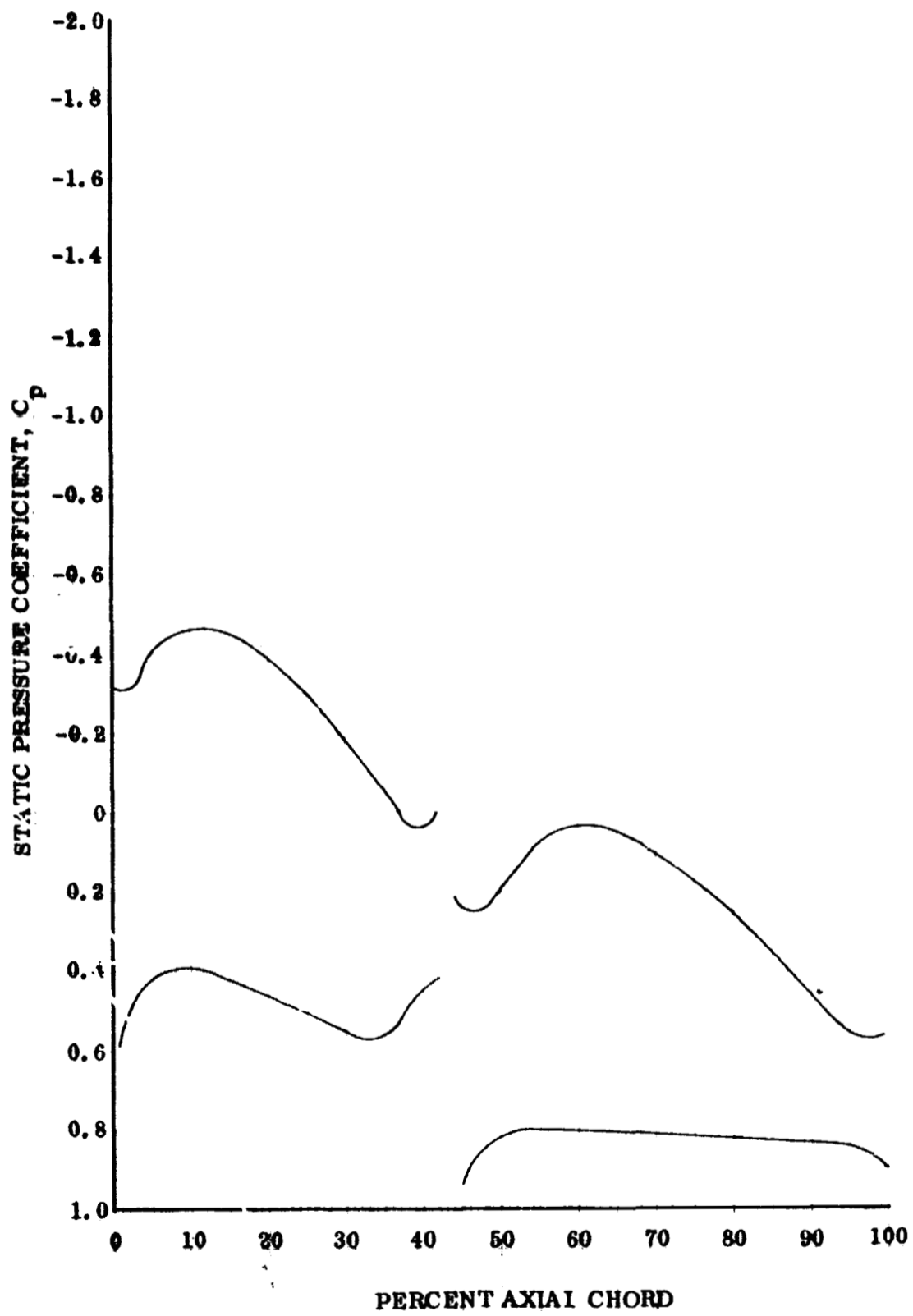
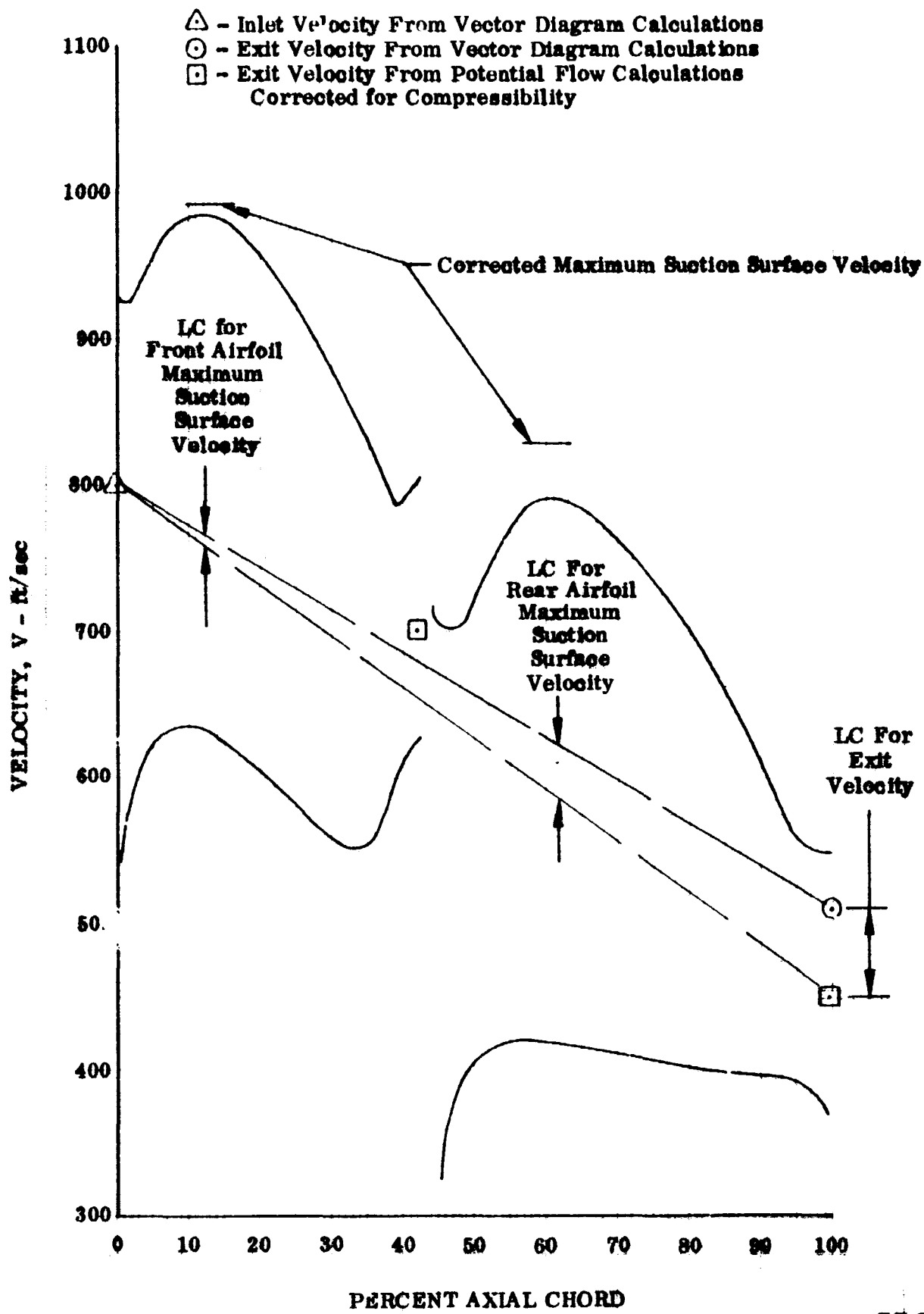


Figure 47. Rotor C Static Pressure Coefficient,
75% Span From Tip

DF 90602



DF 90603

Figure 48. Rotor C Blade Surface Velocities, 75% Span From Tip

DF 90603

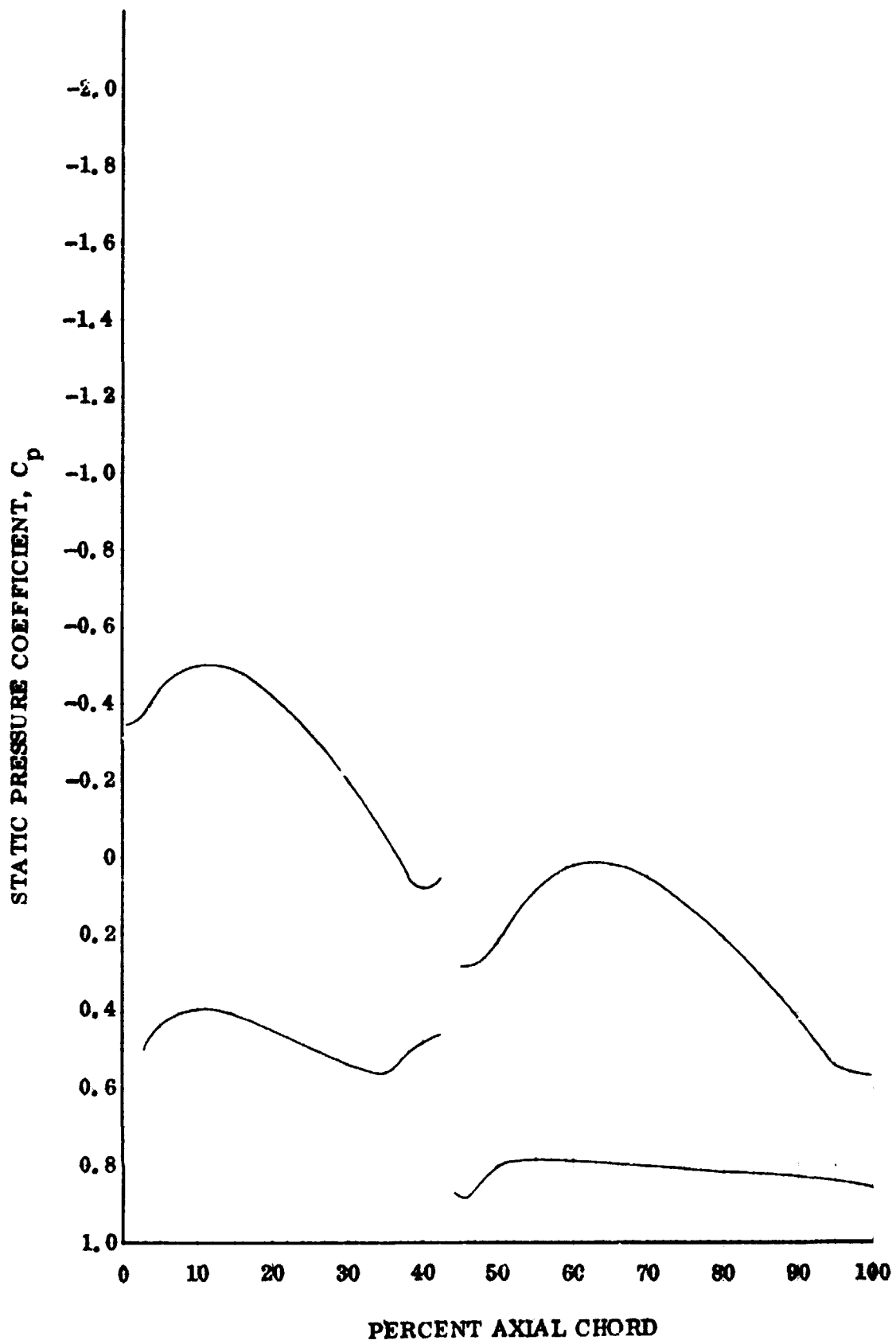


Figure 49. Rotor C Static Pressure Coefficient,
95% Span From Tip

DF 90604

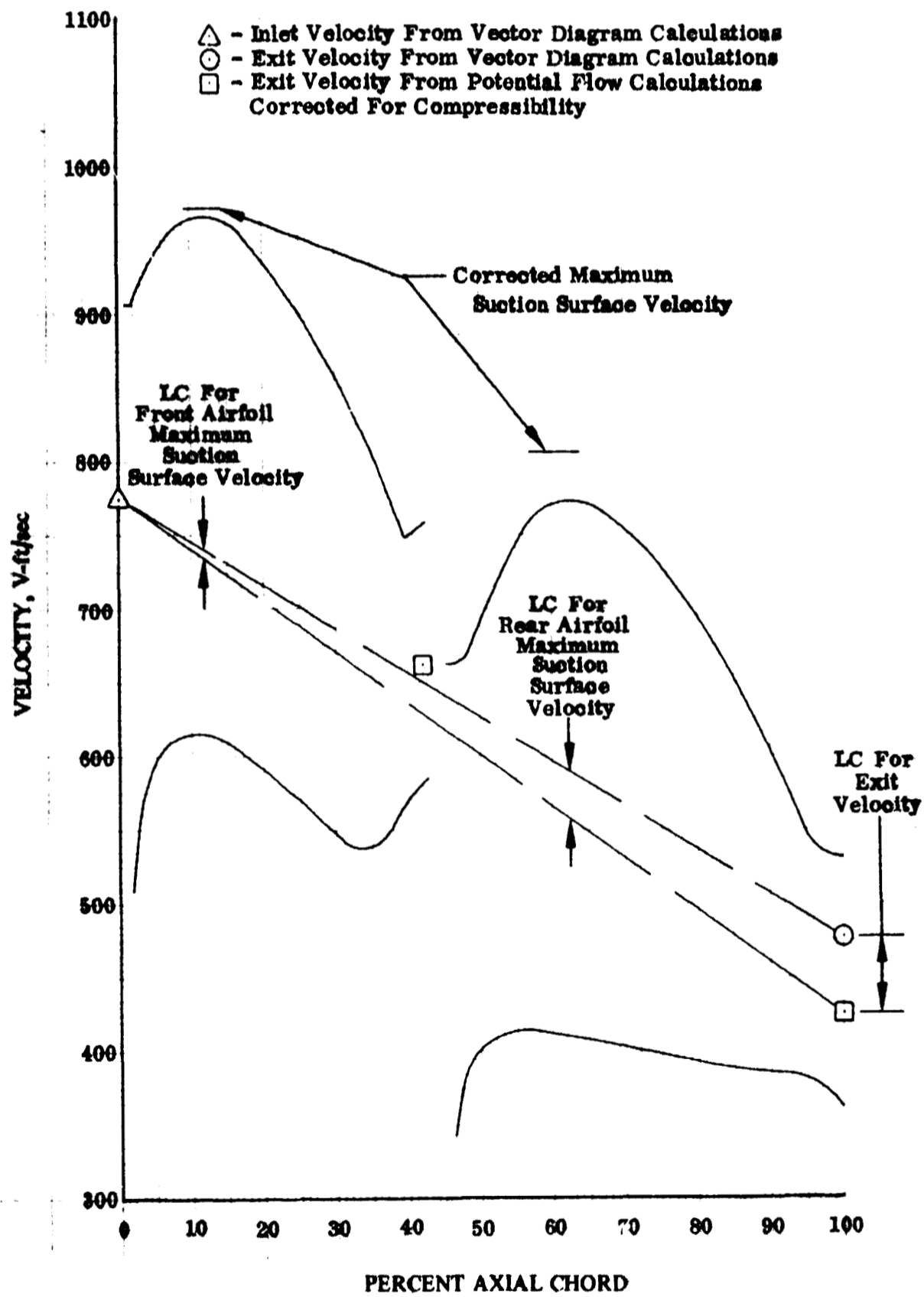


Figure 50. Rotor C Blade Surface Velocities, 95% Span From Tip

DF 90605

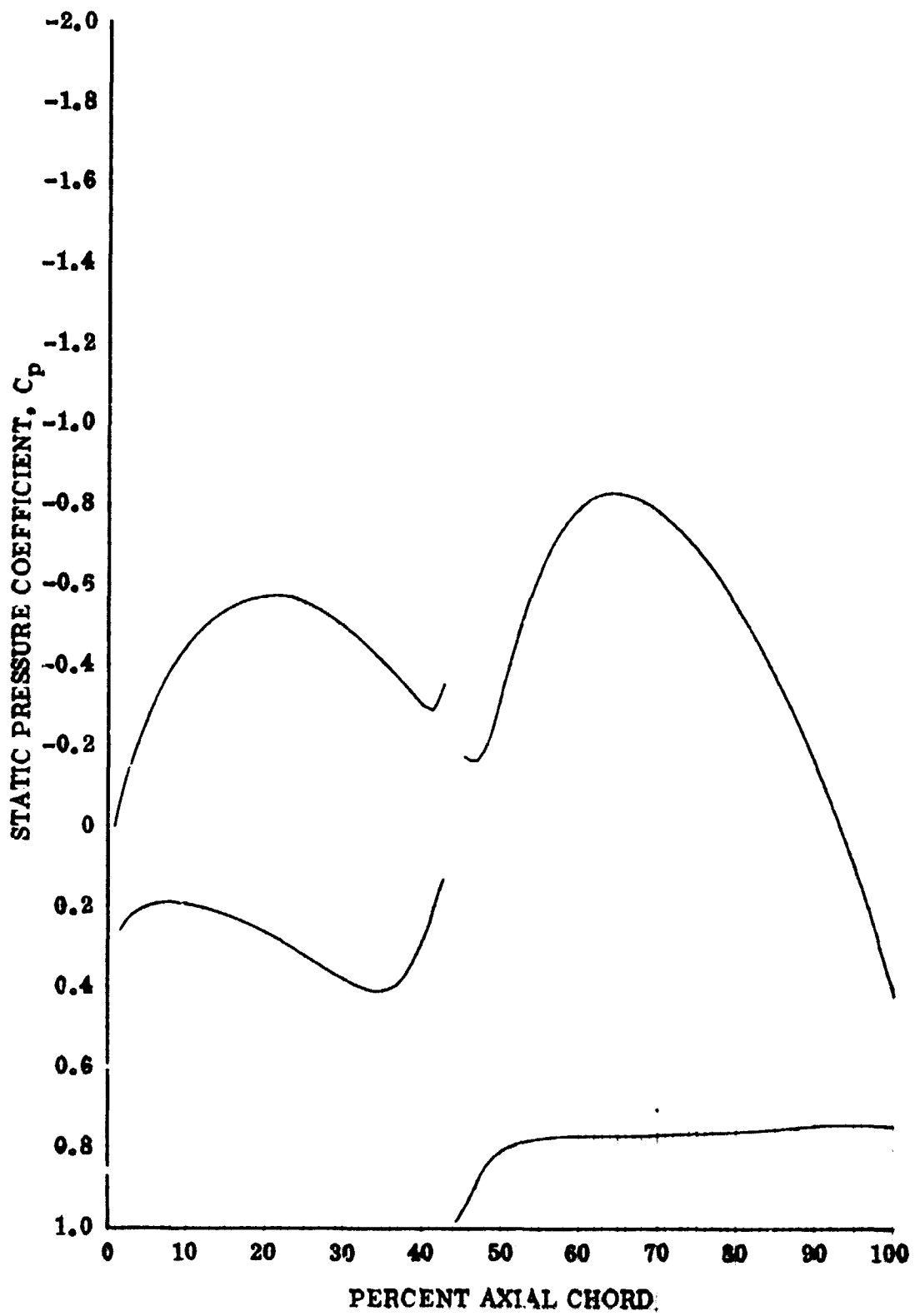


Figure 51. Stator B Static Pressure Coefficient, 5% Span From Tip DF 90606

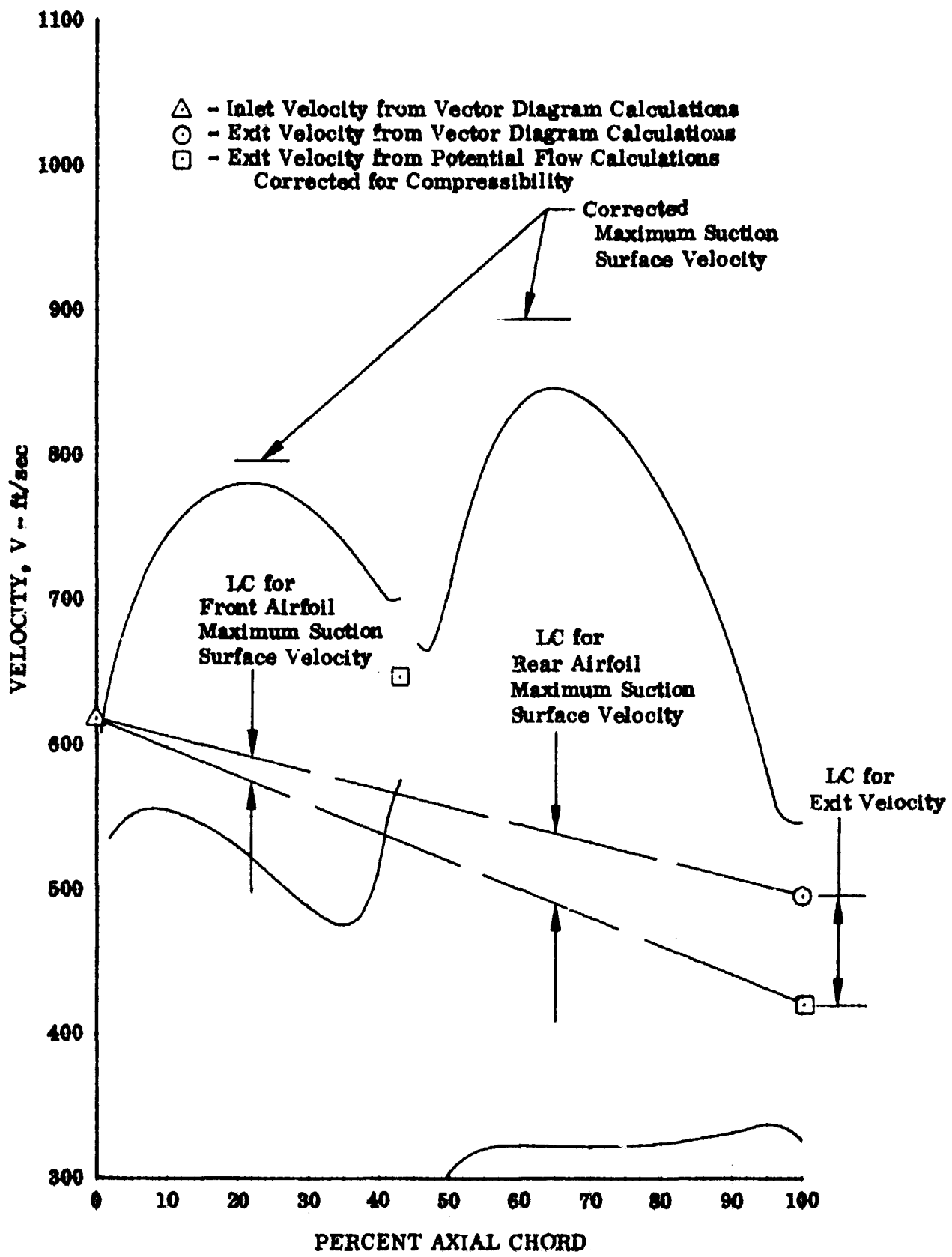


Figure 52. Stator B Vane Surface Velocities, 5% Span From Tip

DF 90607

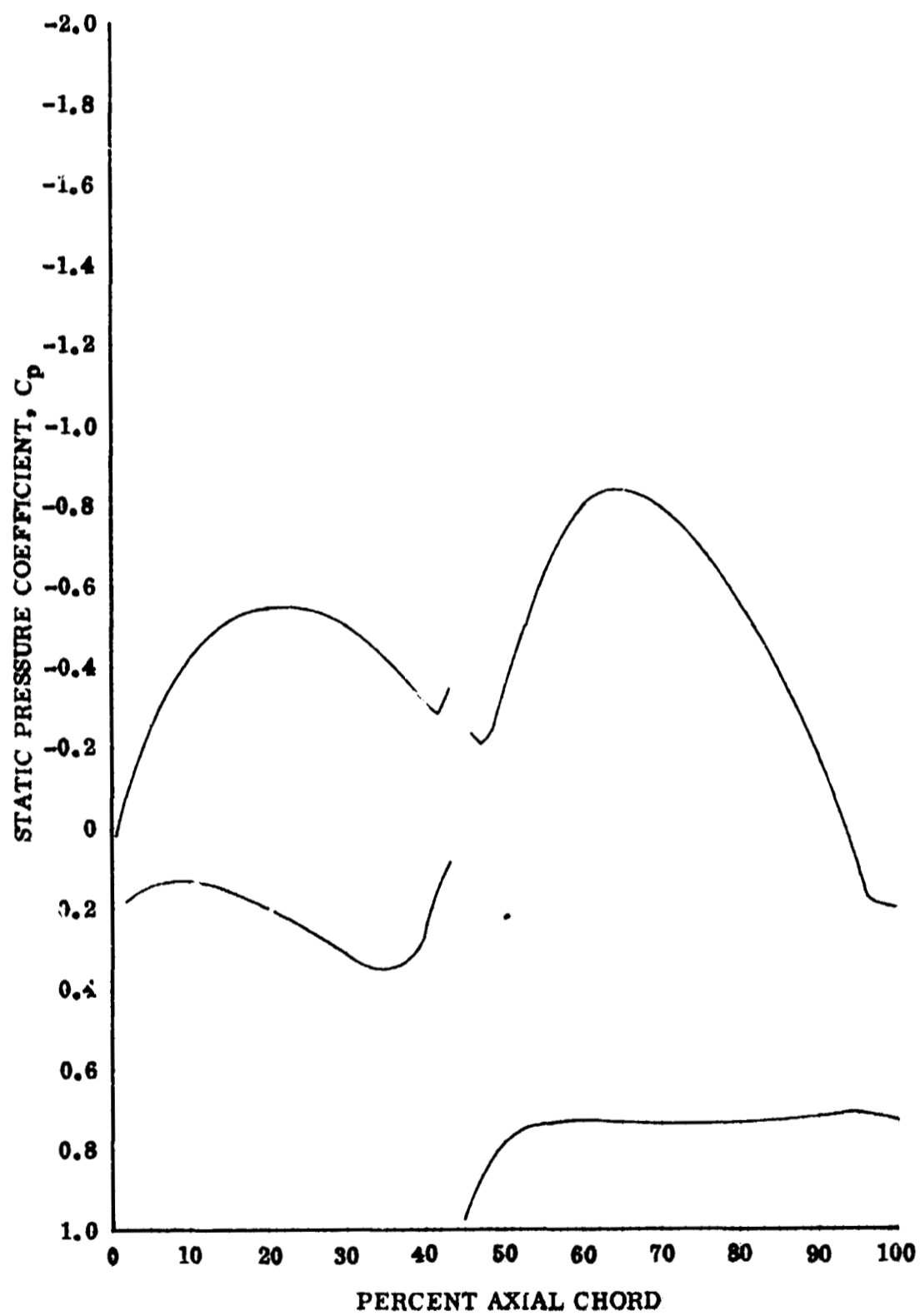


Figure 53. Stator B Static Pressure Coefficient,
25% Span From Tip

DF 90608

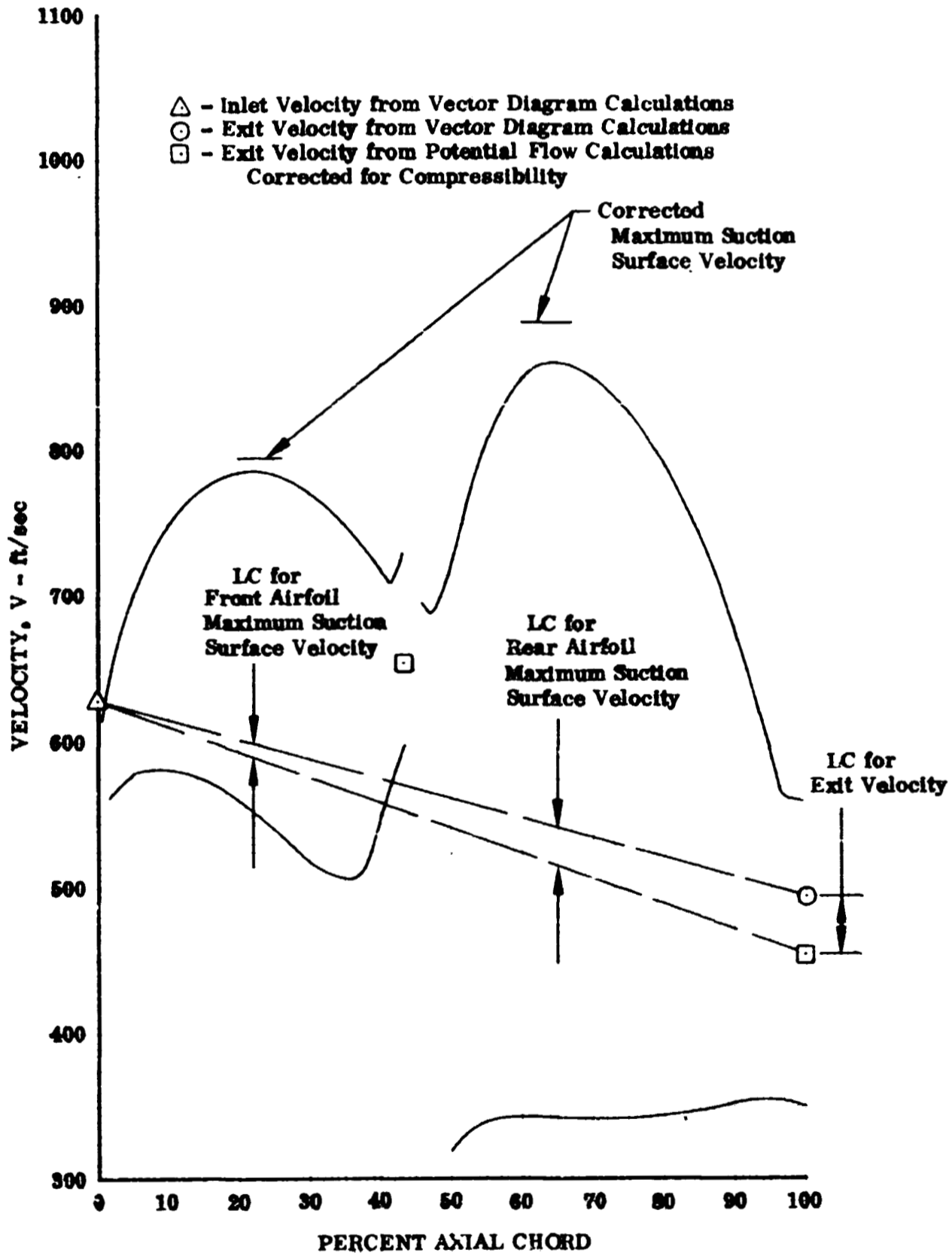


Figure 54. Stator B Vane Surface Velocities, 25% Span From Tip

DF 90609

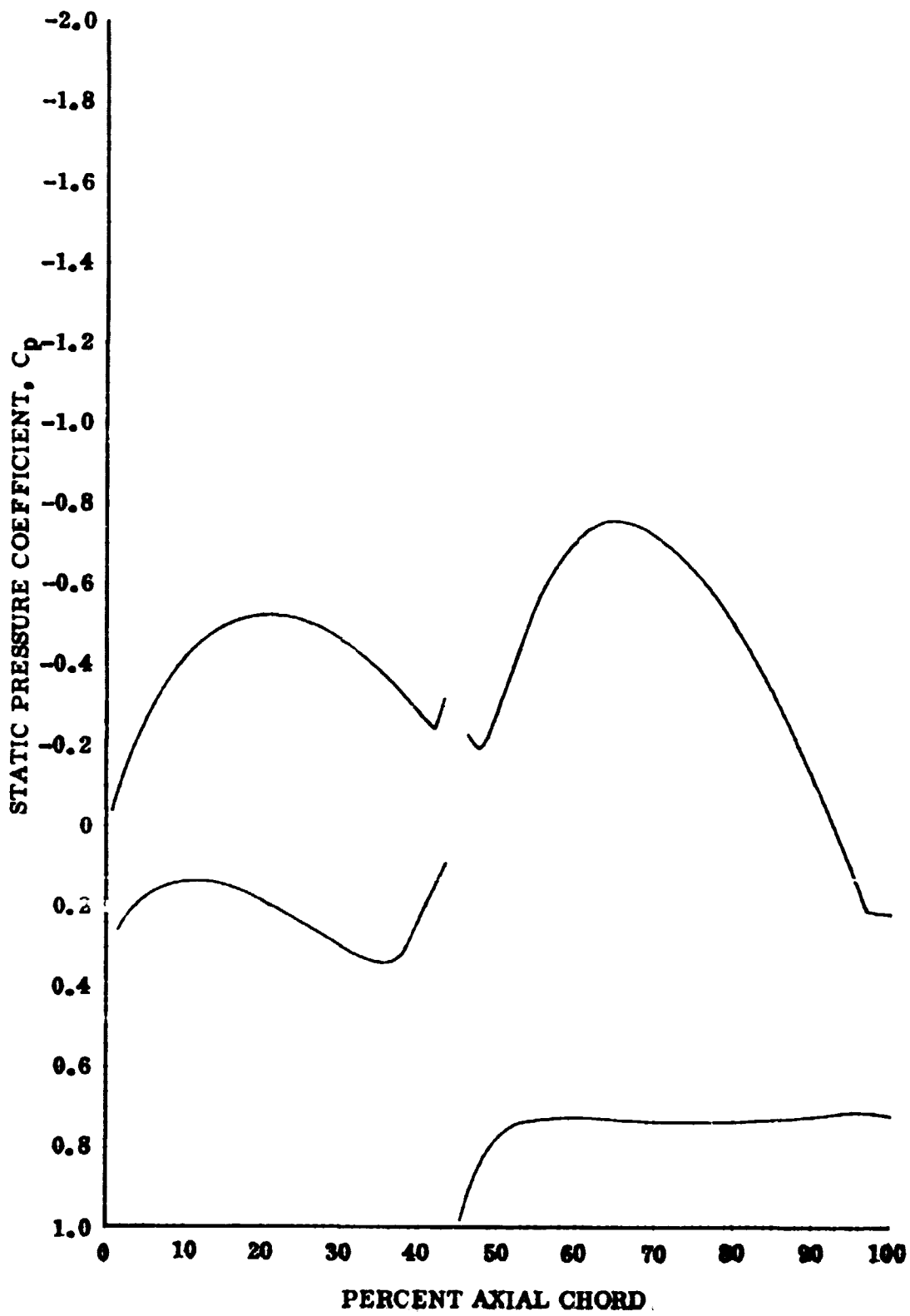


Figure 55. Stator B Static Pressure Coefficient,
50% Span

DF 90610

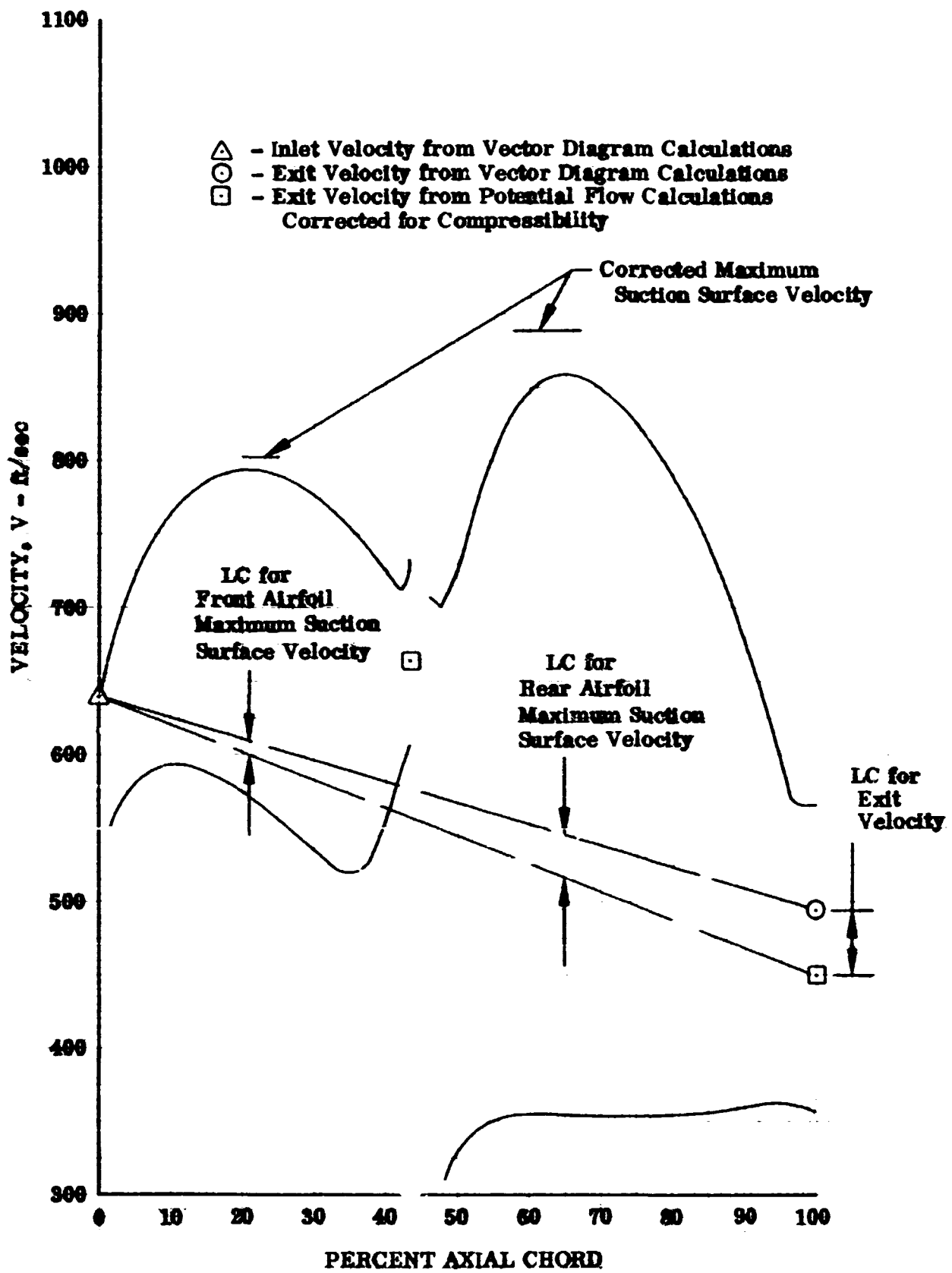


Figure 56. Stator B Vane Surface Velocities, 50% Span

DF 90611

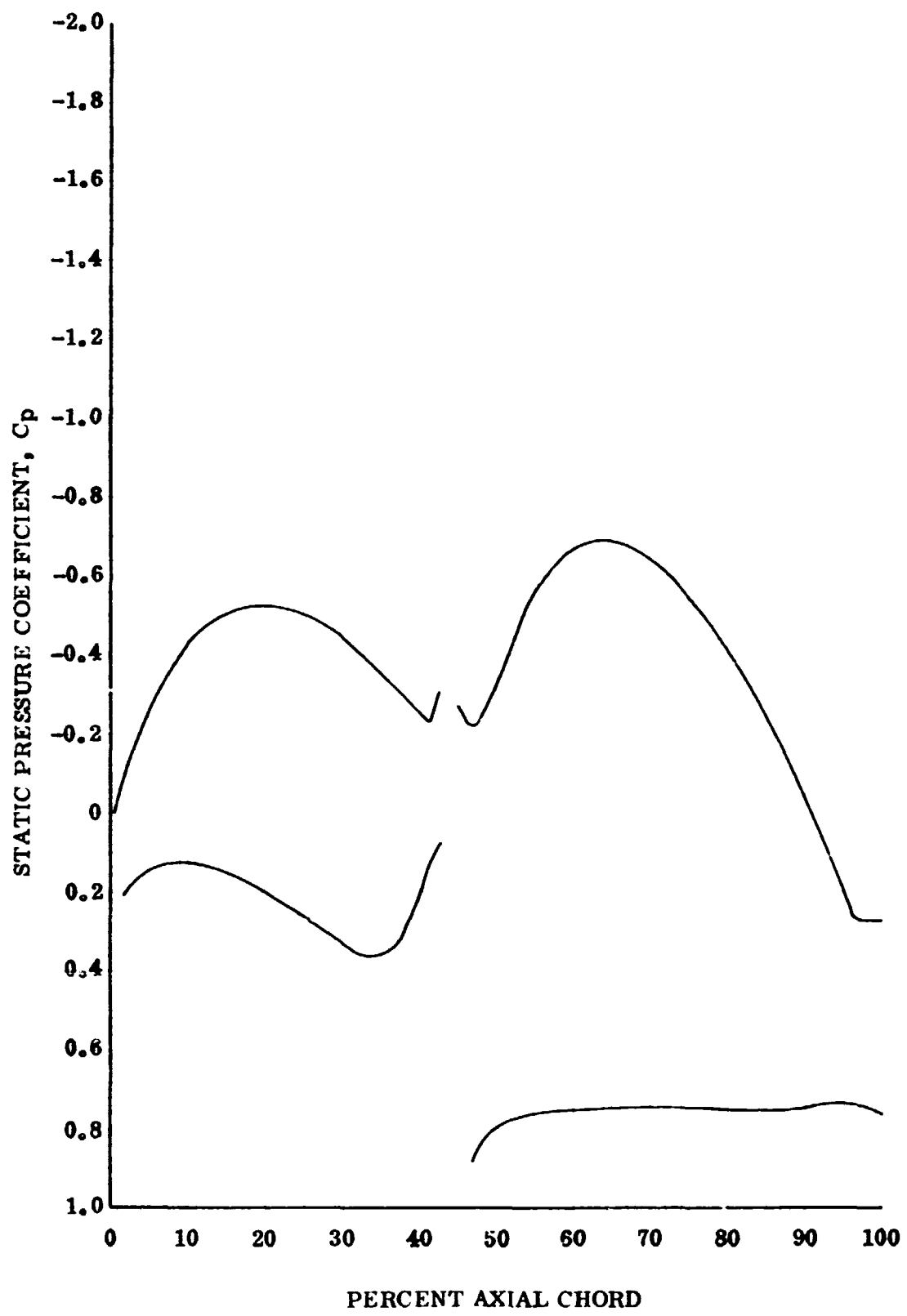


Figure 57. Stator B Static Pressure Coefficient,
75% Span From Tip

DF 90612

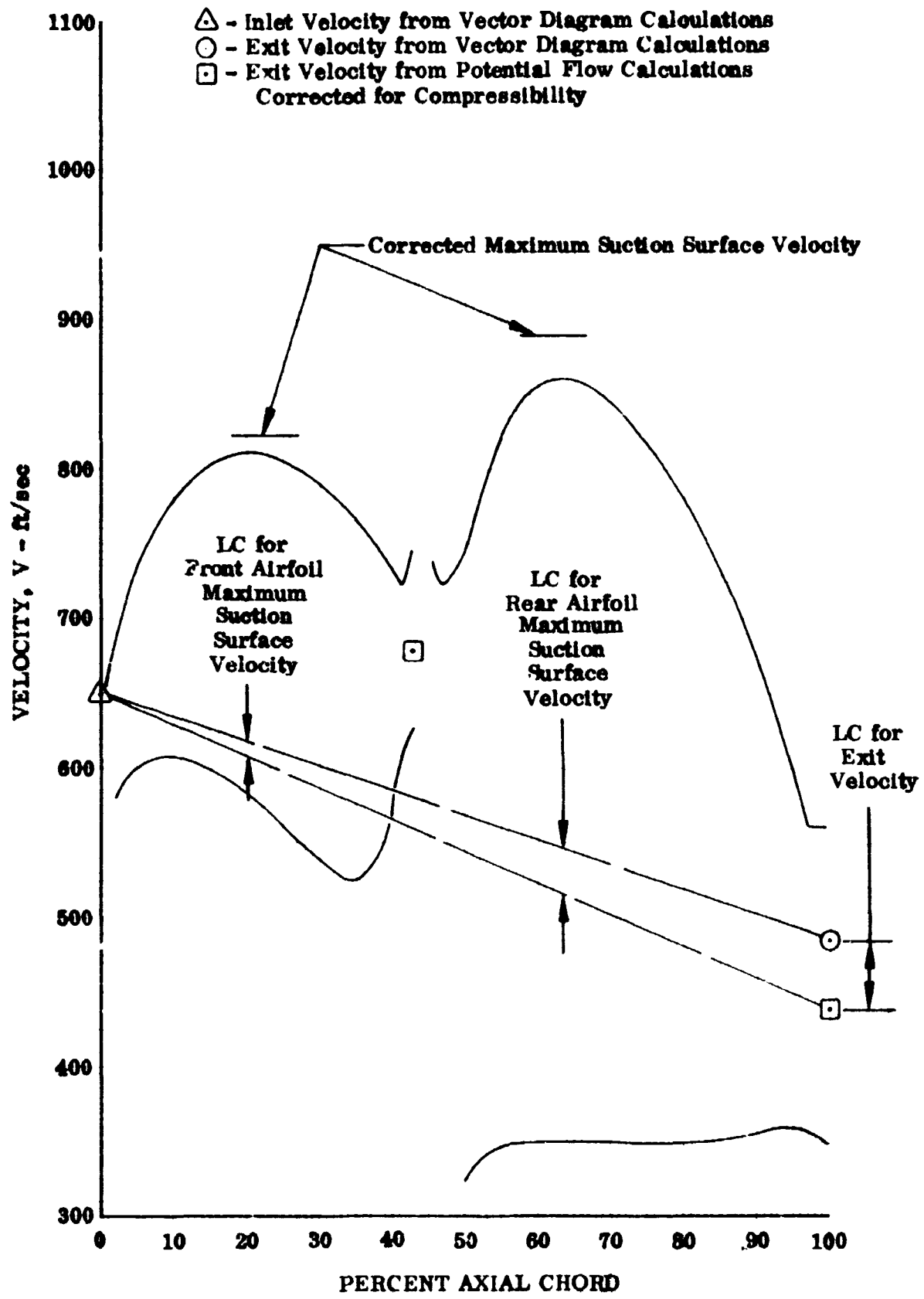


Figure 58. Stator B Vane Surface Velocities, 75% Span From Tip

DF 90613

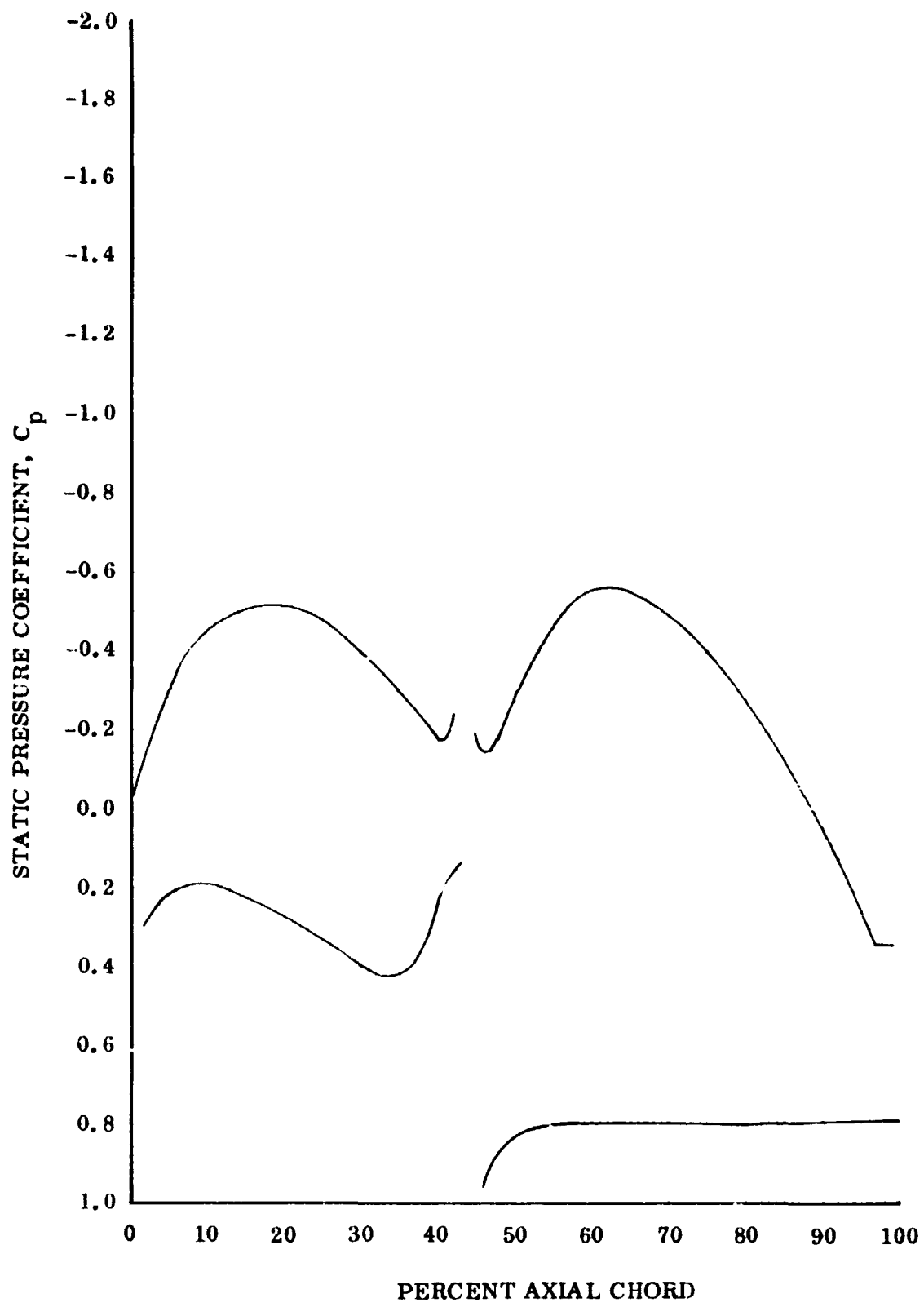


Figure 59. Stator B Static Pressure Coefficient,
95% Span From Tip

DF 90614

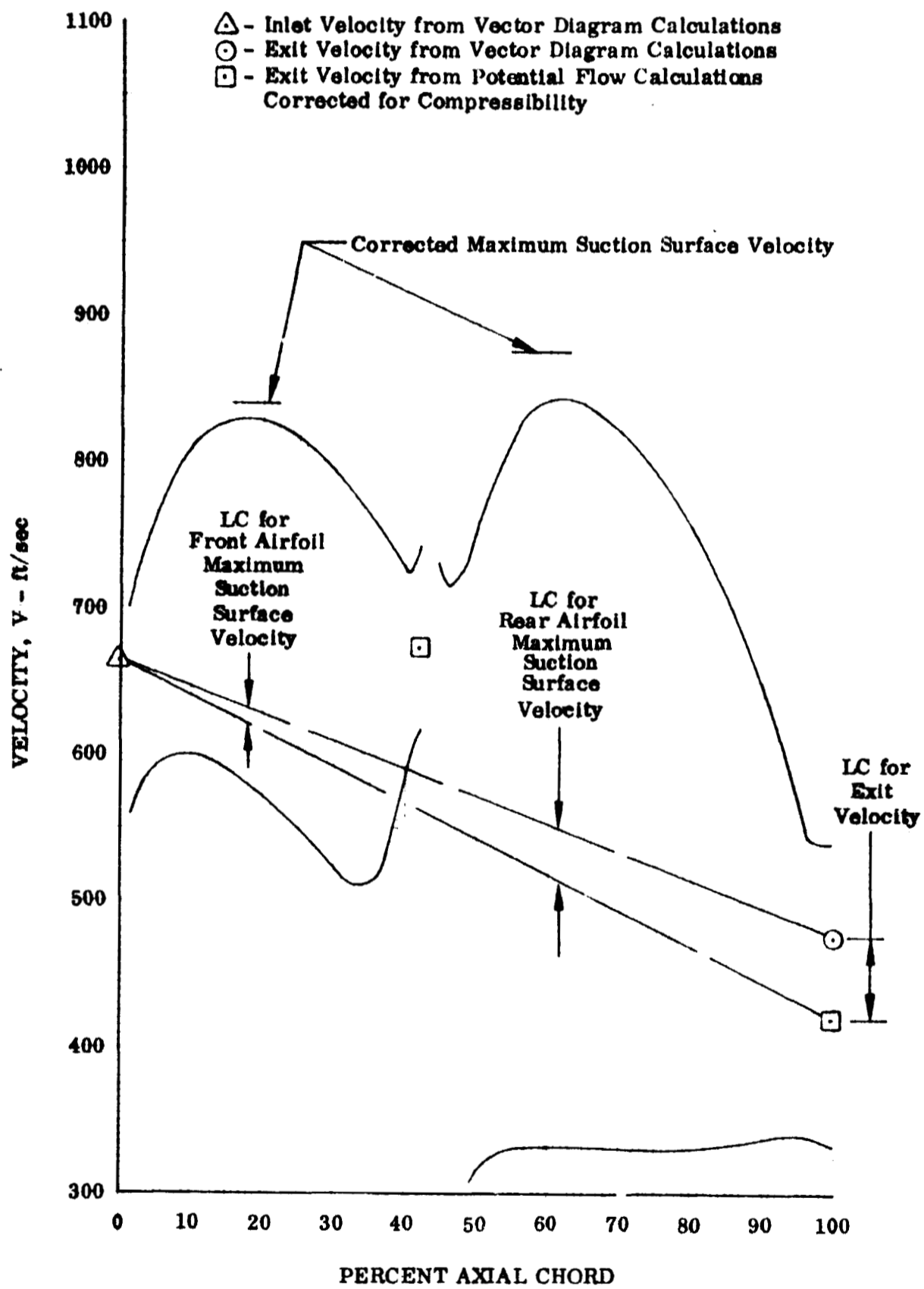
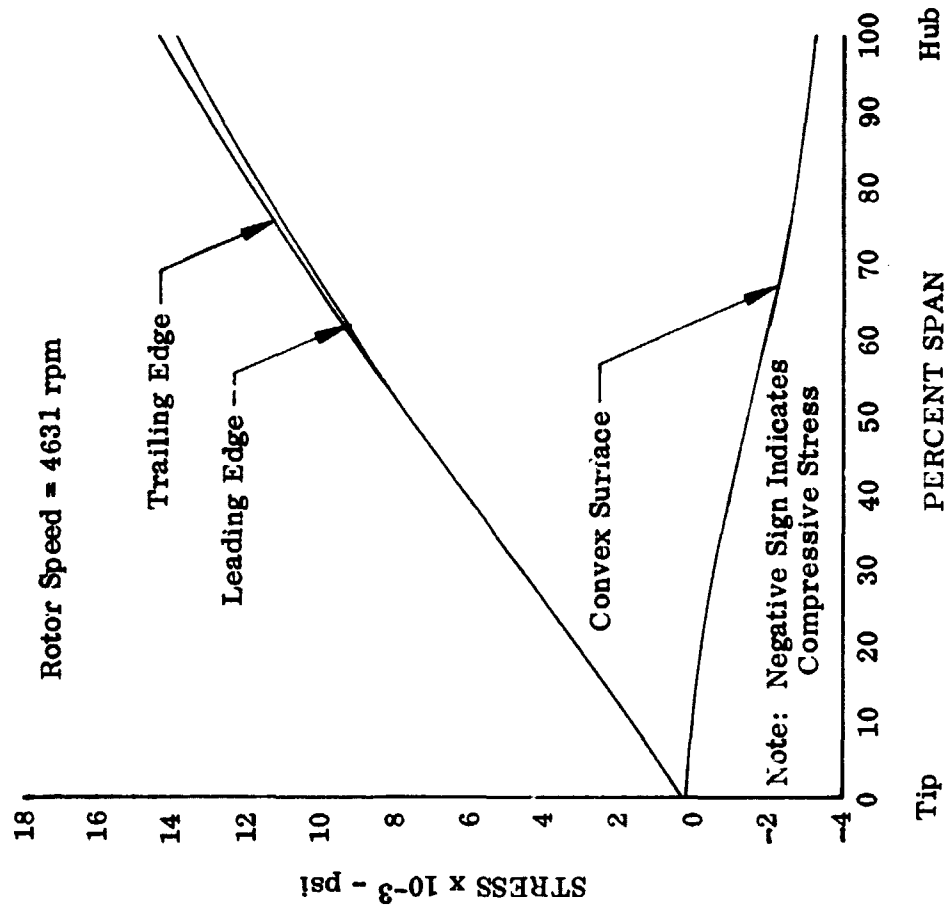


Figure 60. Stator B Vane Surface Velocities, 95% Span From Tip

DF 90615



23 Figure 61. Calculated Rotor A Stress Distribution

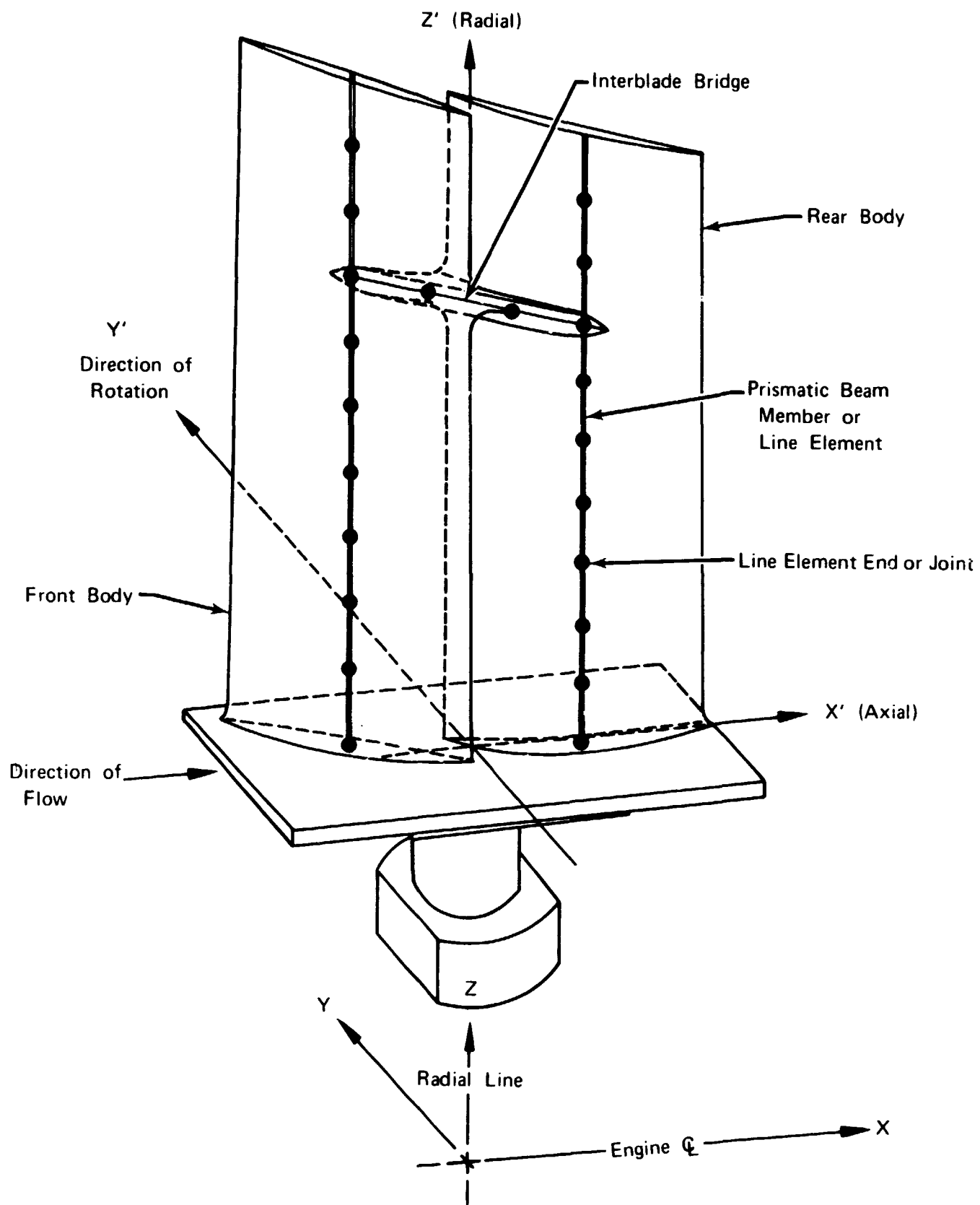
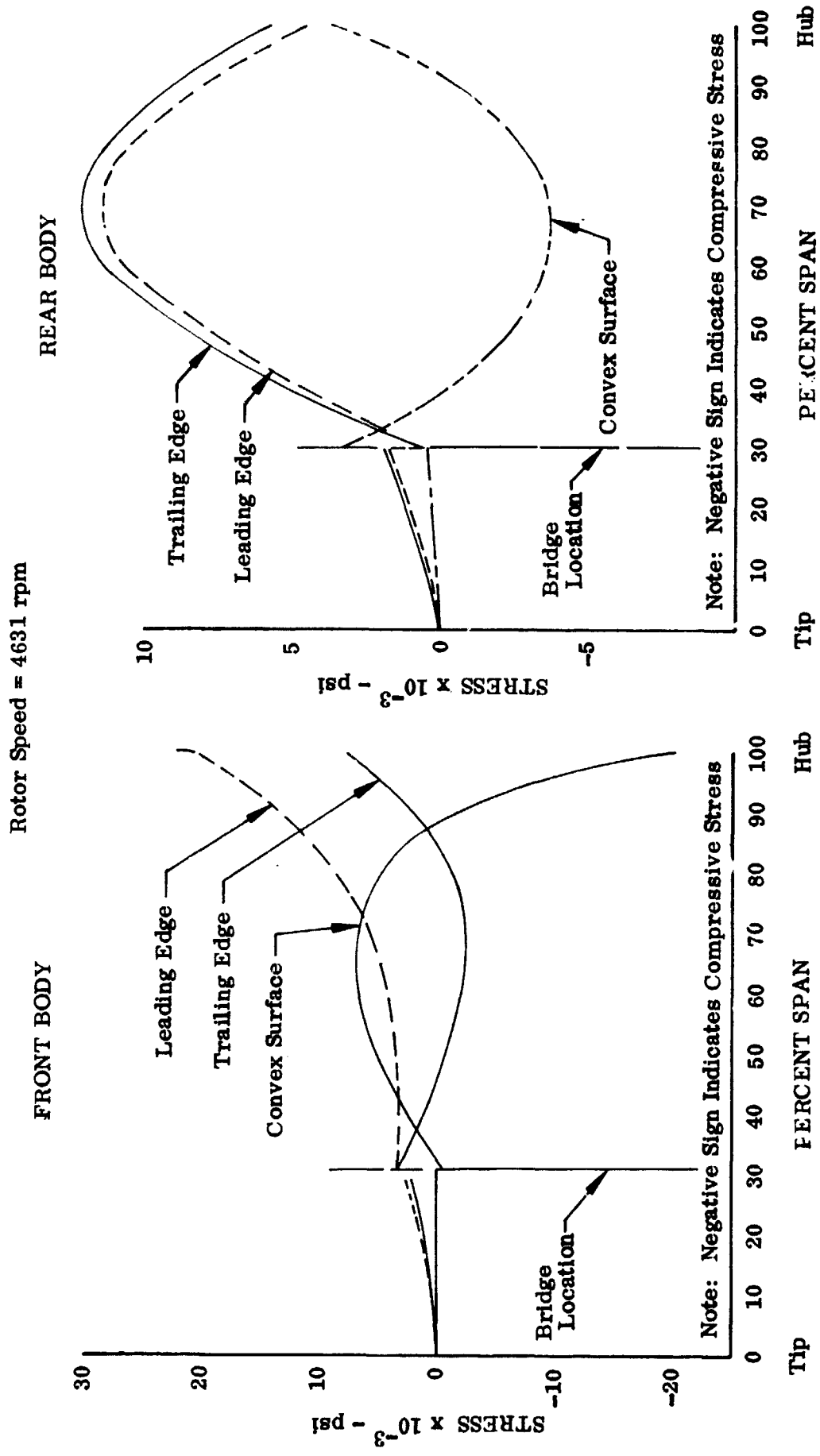


Figure 62. Graphic Description of Tandem Rotor Analytical Model

FD 62295



85 Figure 63. Calculated Rotor B Stress Distribution

DF 90632

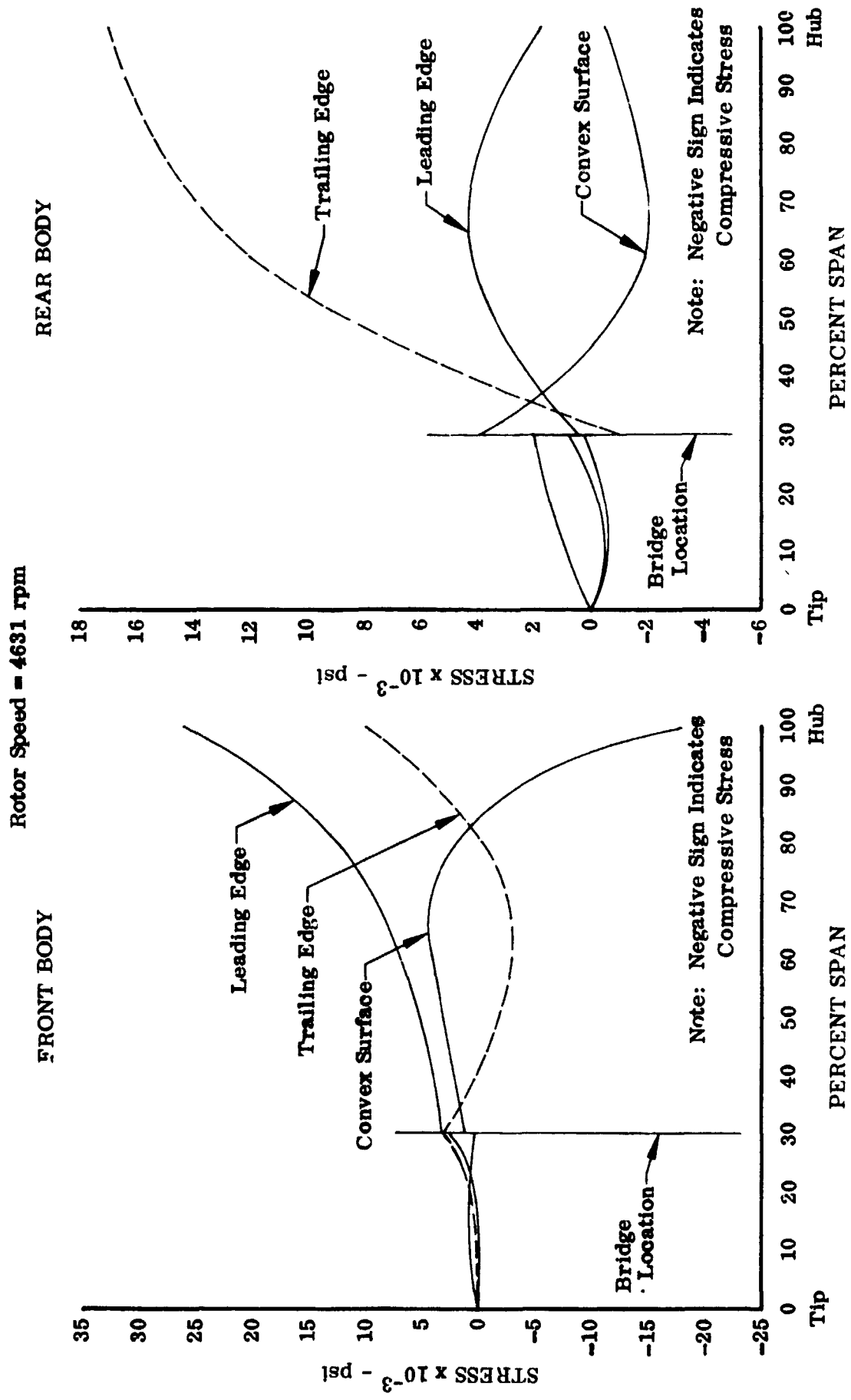


Figure 64. Calculated Rotor C Stress Distribution

DF 90633

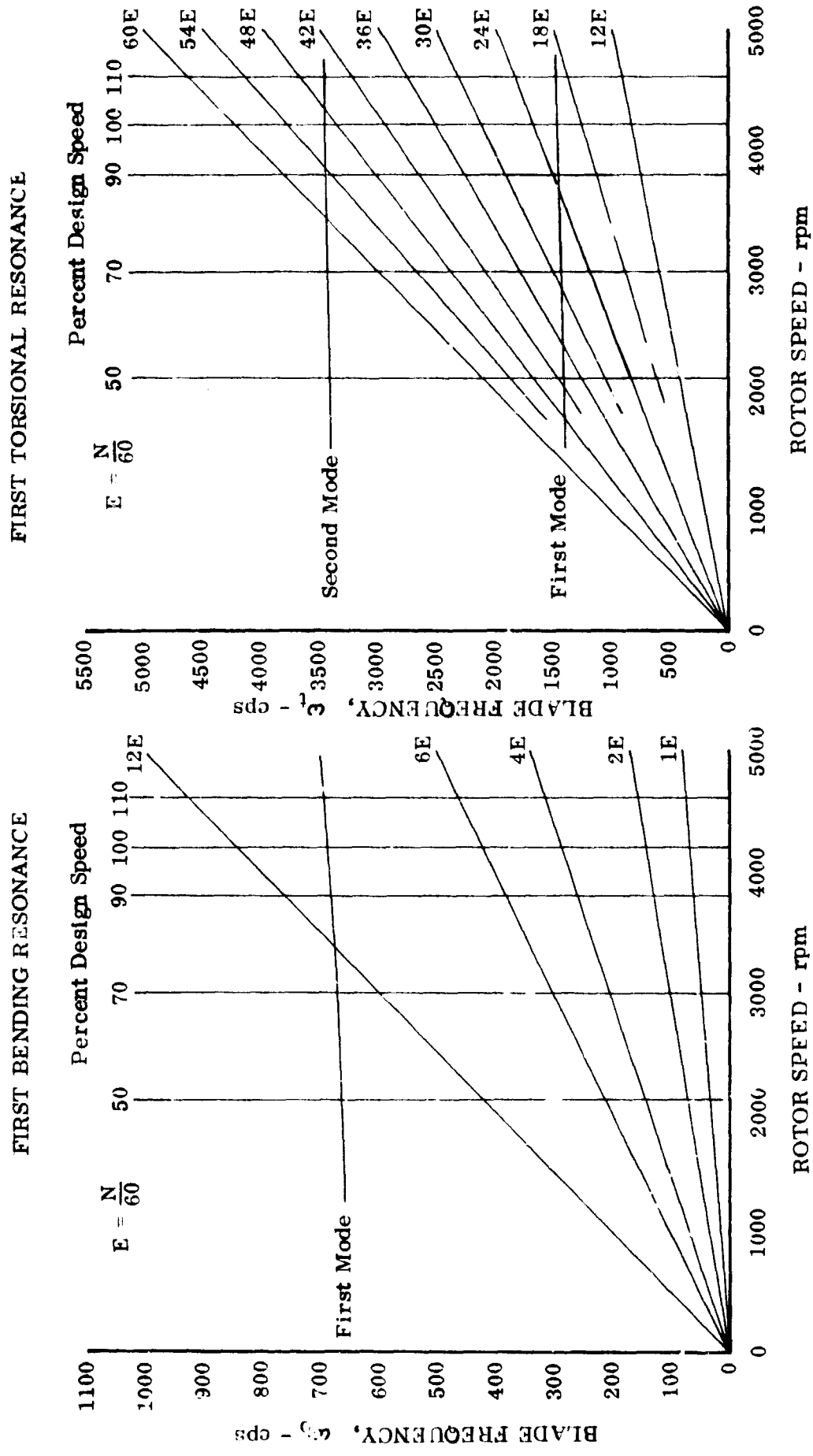


Figure 65. Rotor A Resonance Diagram for First Bending and First Torsional Mode Vibration DF 90616

AMS 5616 - Stainless Steel (Greek Ascoloy) 200°F

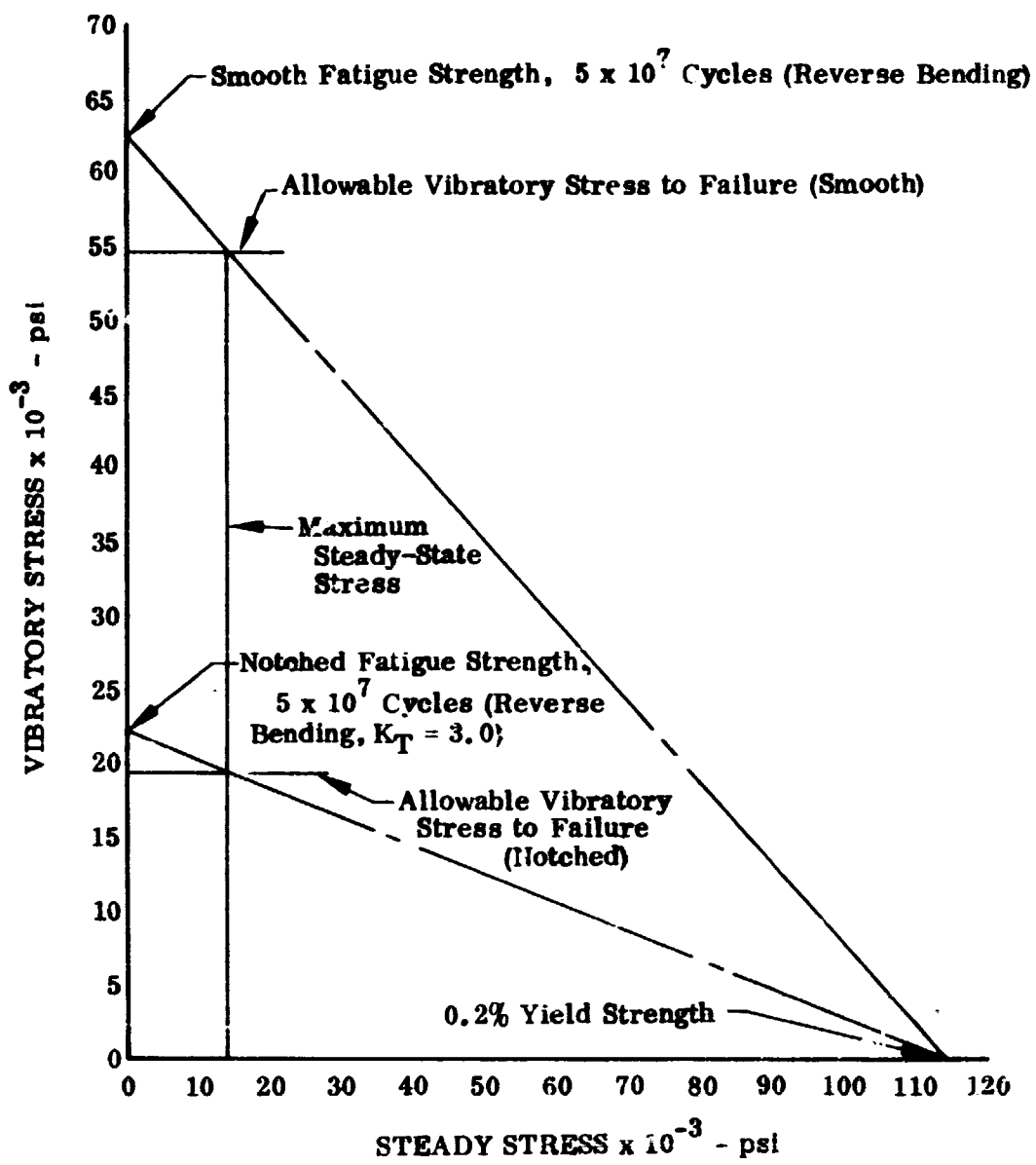
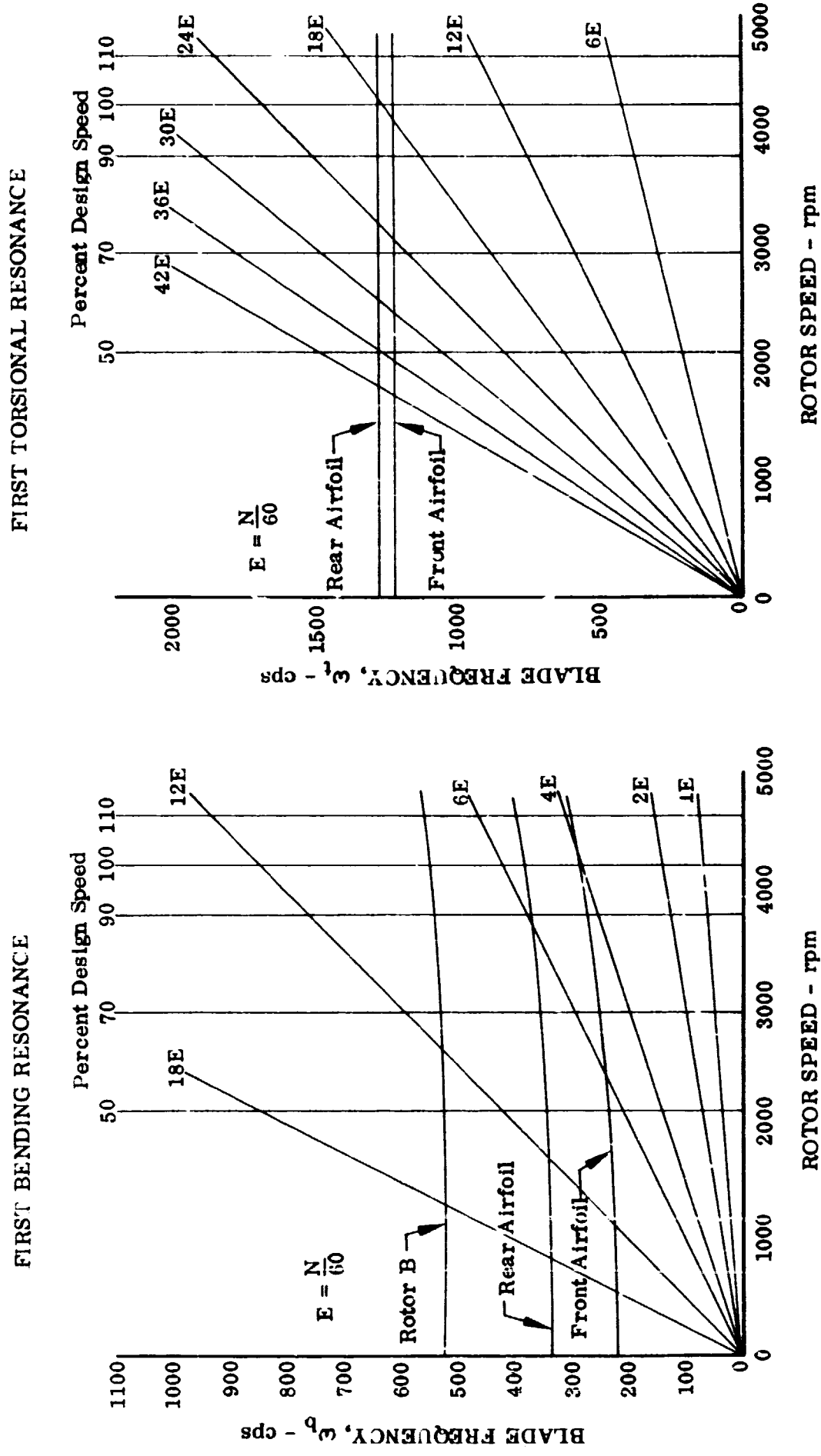


Figure 66. Rotor A Goodman Diagram

DF 90617



29 Figure 67. Rotor B Resonance Diagram for First Bending and First Torsional Mode Vibration DF 90618

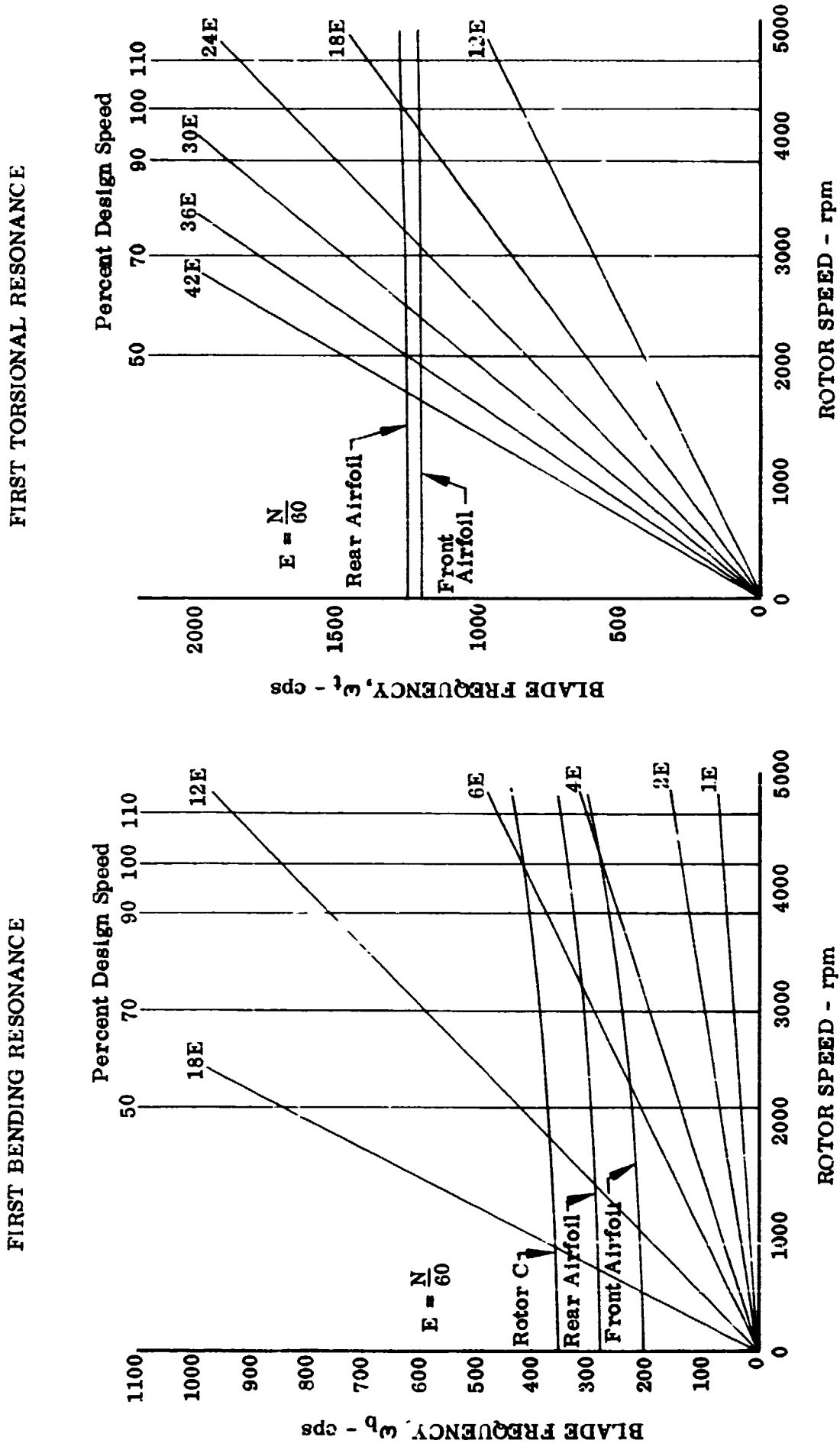


Figure 68. Rotor C Resonance Diagram for First Bending and First Torsional Mode Vibration DF 90619

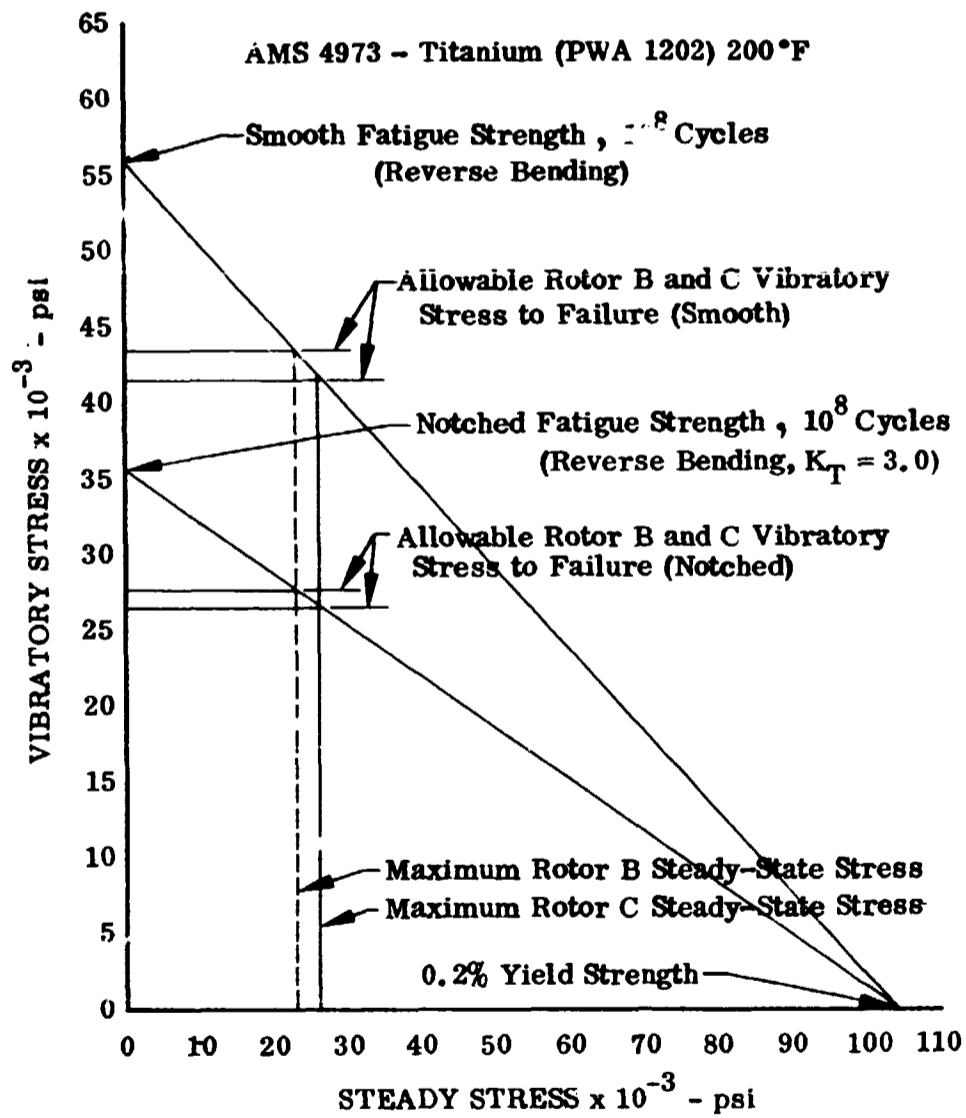


Figure 69. Rotors B and C Goodman Diagram

DF 90620

Rotor Speed = 4210 rpm
 Location = 25% Span From Tip

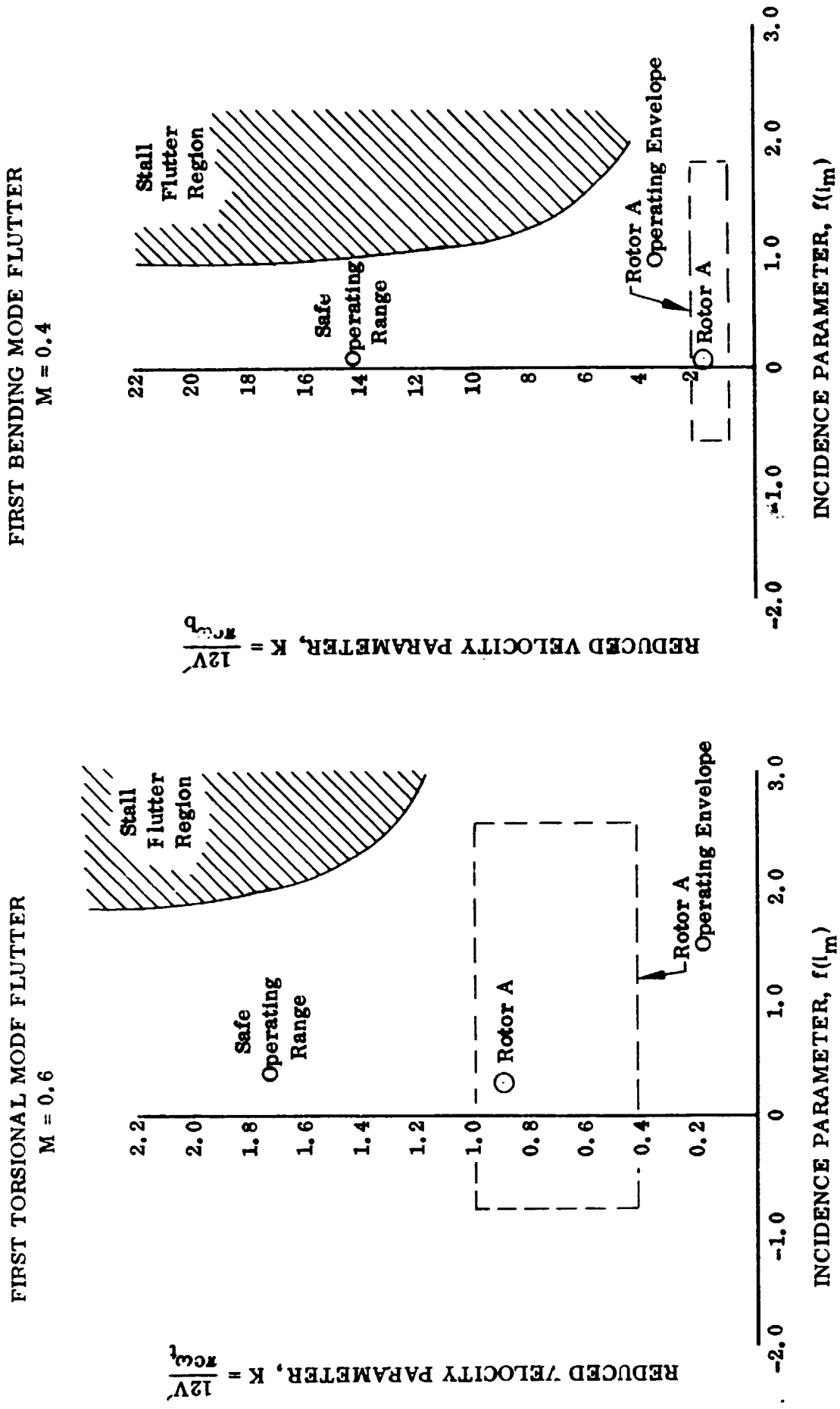


Figure 70. Calculated Rotor A First Bending and First Torsional Mode Flutter Characteristics DF 90621

Rotor Speed = 4210 rpm
 Location = 25% Span From Tip

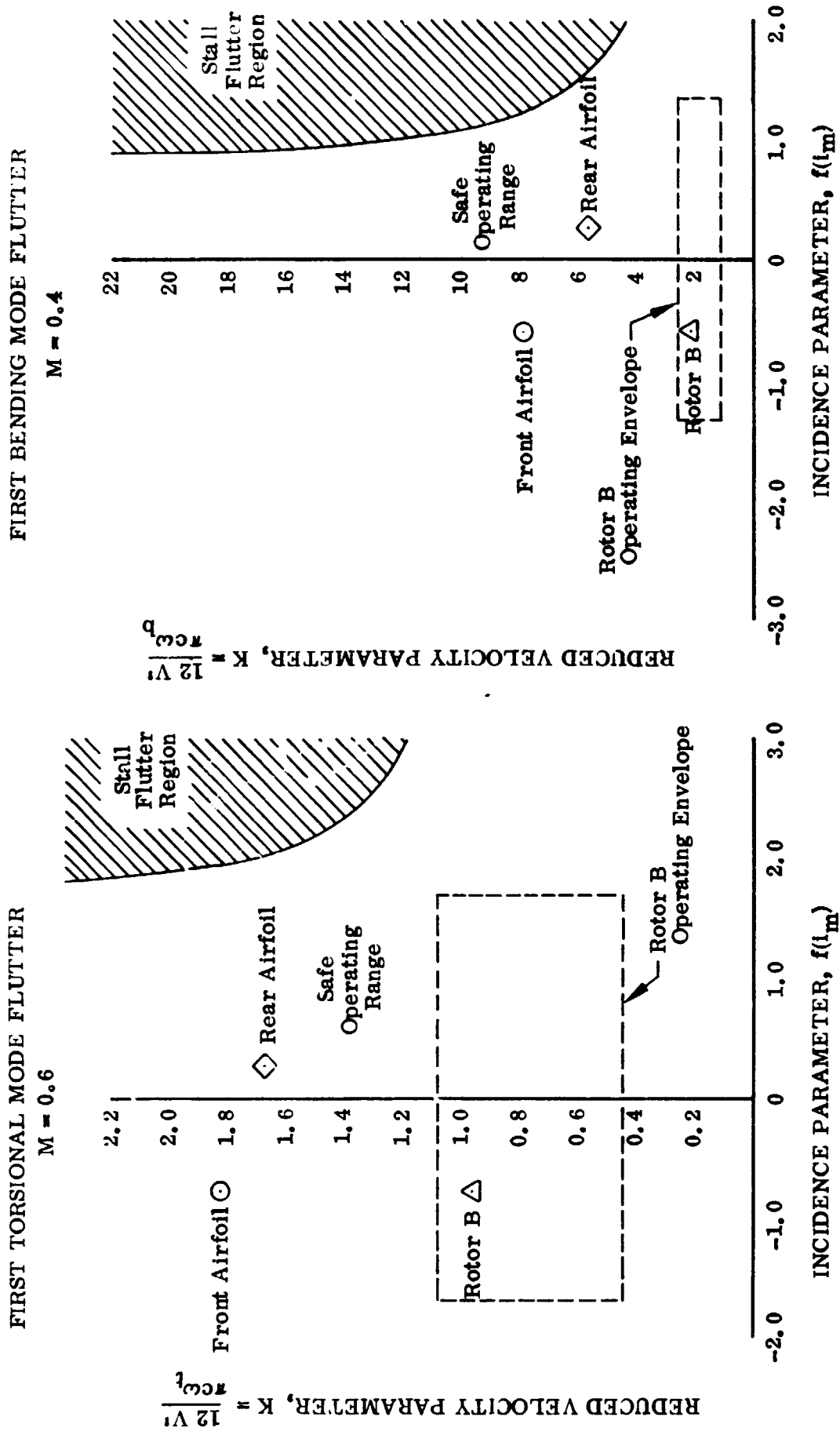
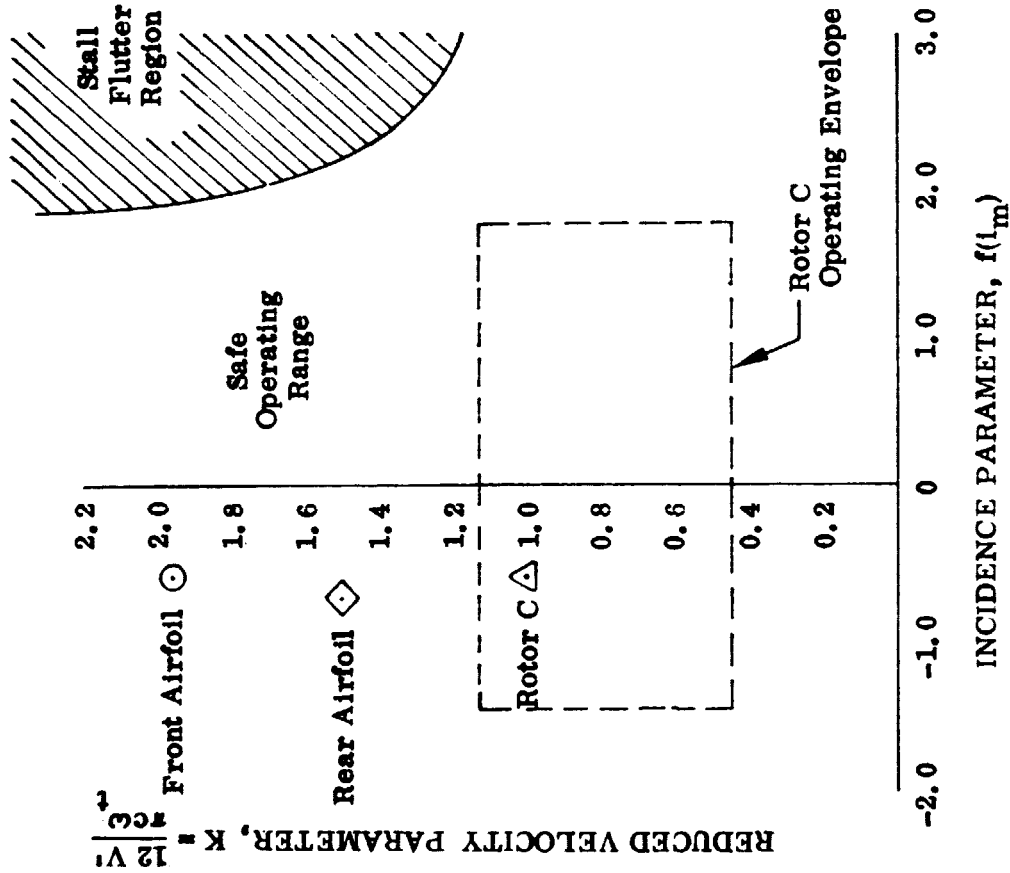


Figure 71. Calculated Rotor B First Bending and First Torsional Mode Flutter Characteristics DF 90622

Rotor Speed = 4210 rpm
 Location = 25% Span From Tip

FIRST TORSIONAL MODE FLUTTER

M = 0.6



FIRST BENDING MODE FLUTTER

M = 0.4

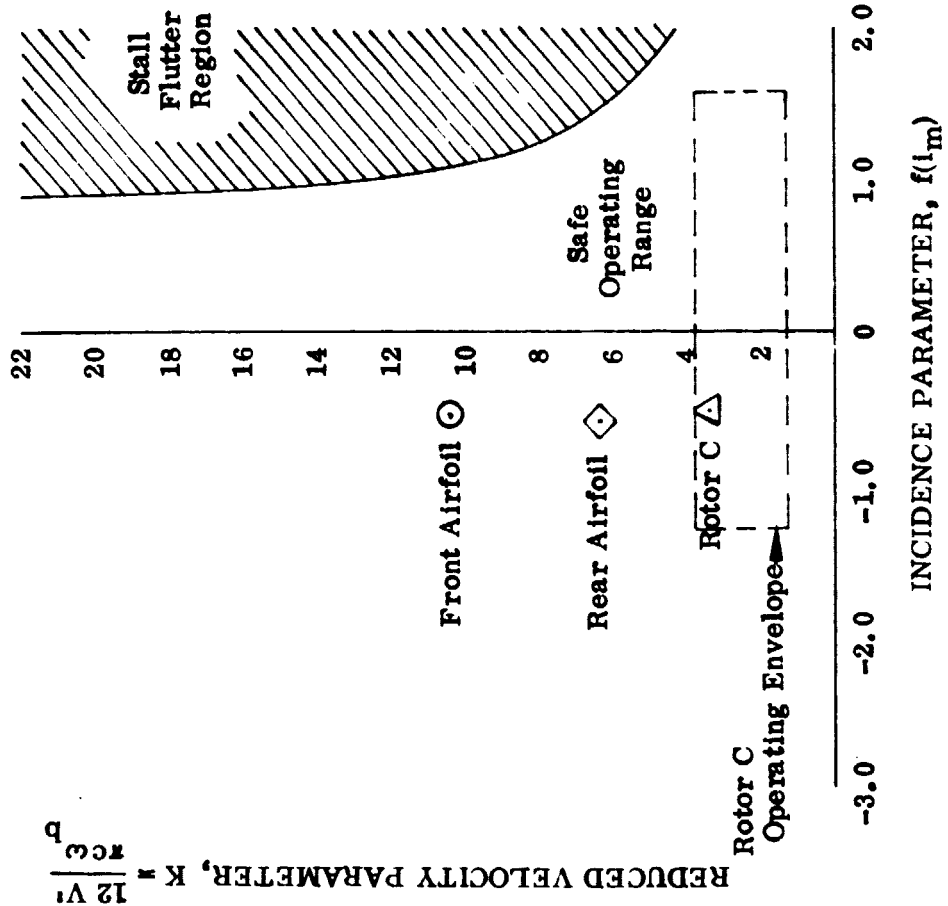


Figure 72. Calculated Rotor C First Bending and First Torsional Mode Flutter Characteristics DF 90623

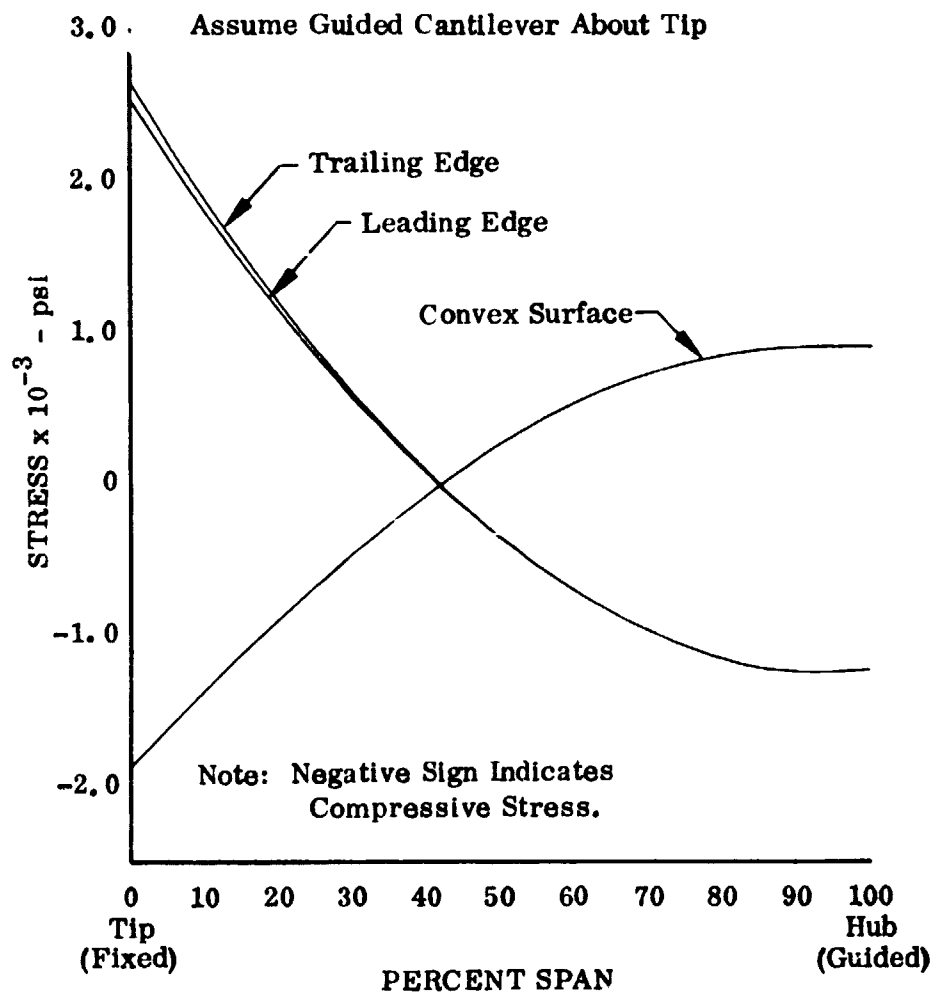


Figure 73. Calculated Stator A Stress Distribution

DF 90634

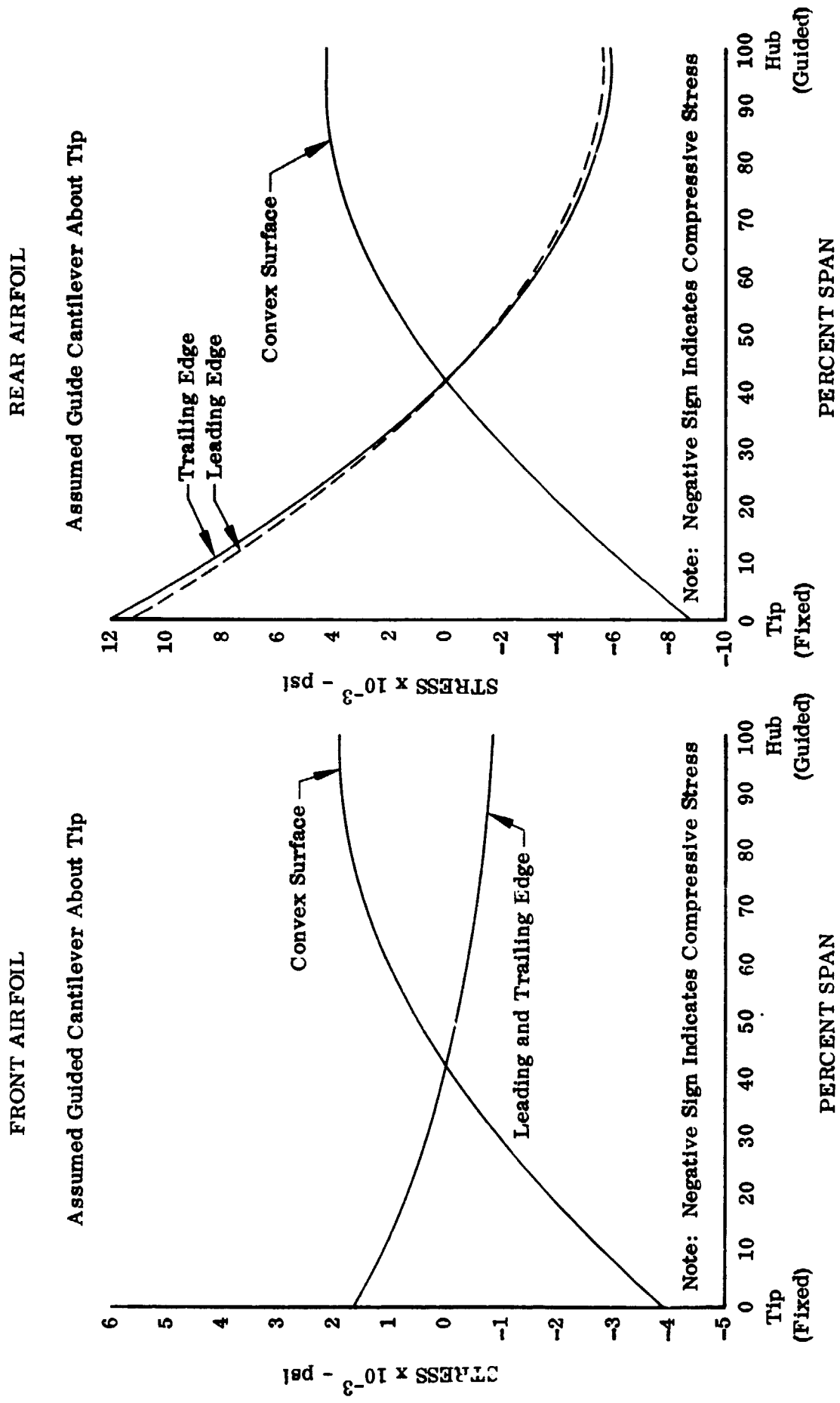
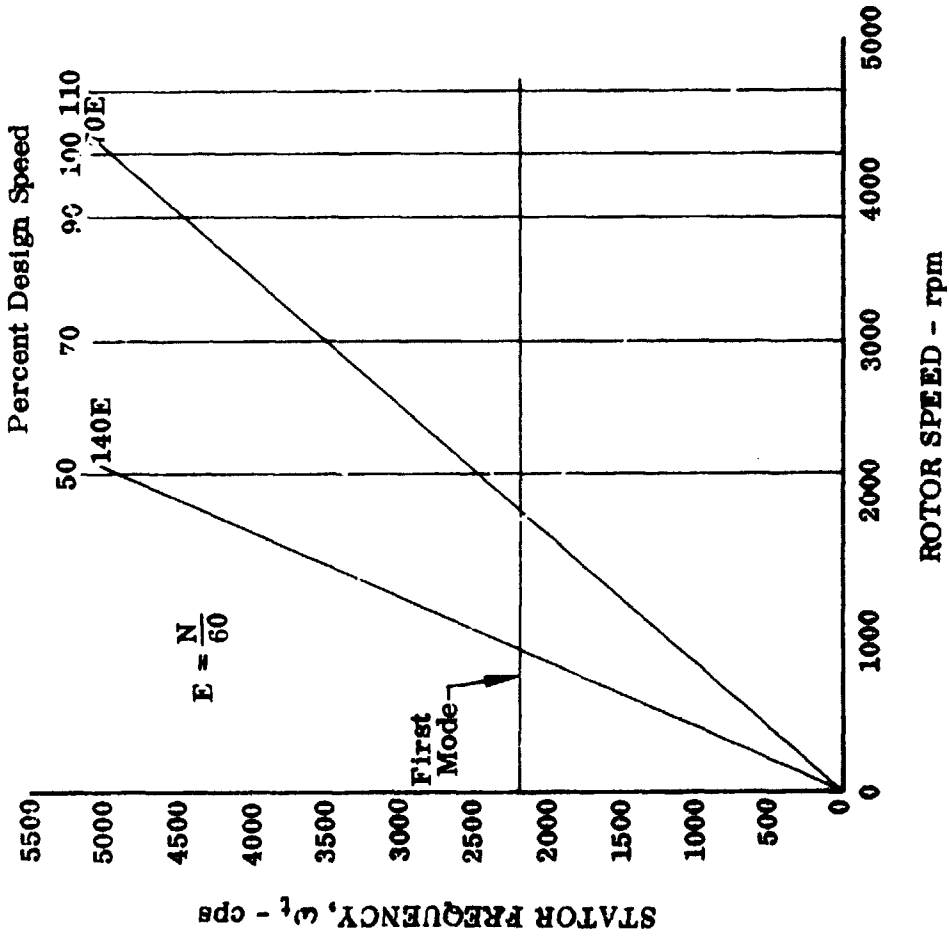


Figure 74. Calculated Stator B Stress Distribution

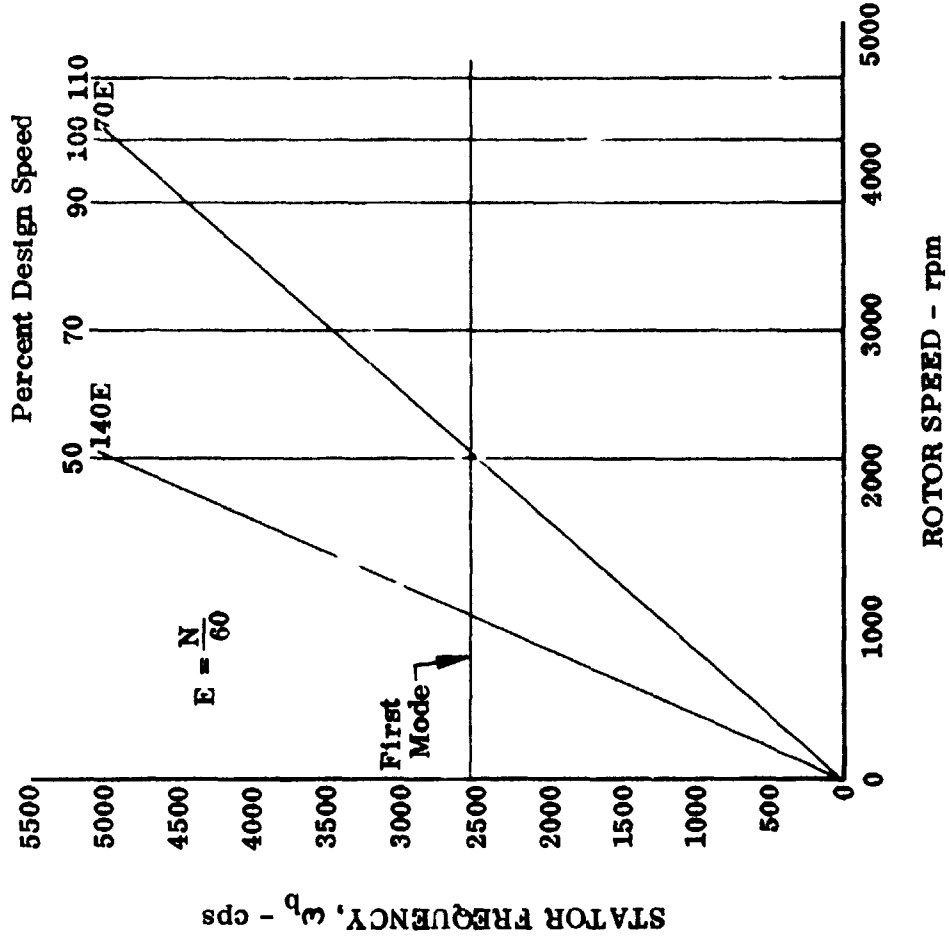
FIRST BENDING RESONANCE

Fixed-Fixed Configuration



FIRST TORSIONAL RESONANCE

Fixed-Fixed Configuration



52 Figure 75. Stator A Resonance Diagram for First Bending and First Torsional Mode Vibration DF 90624

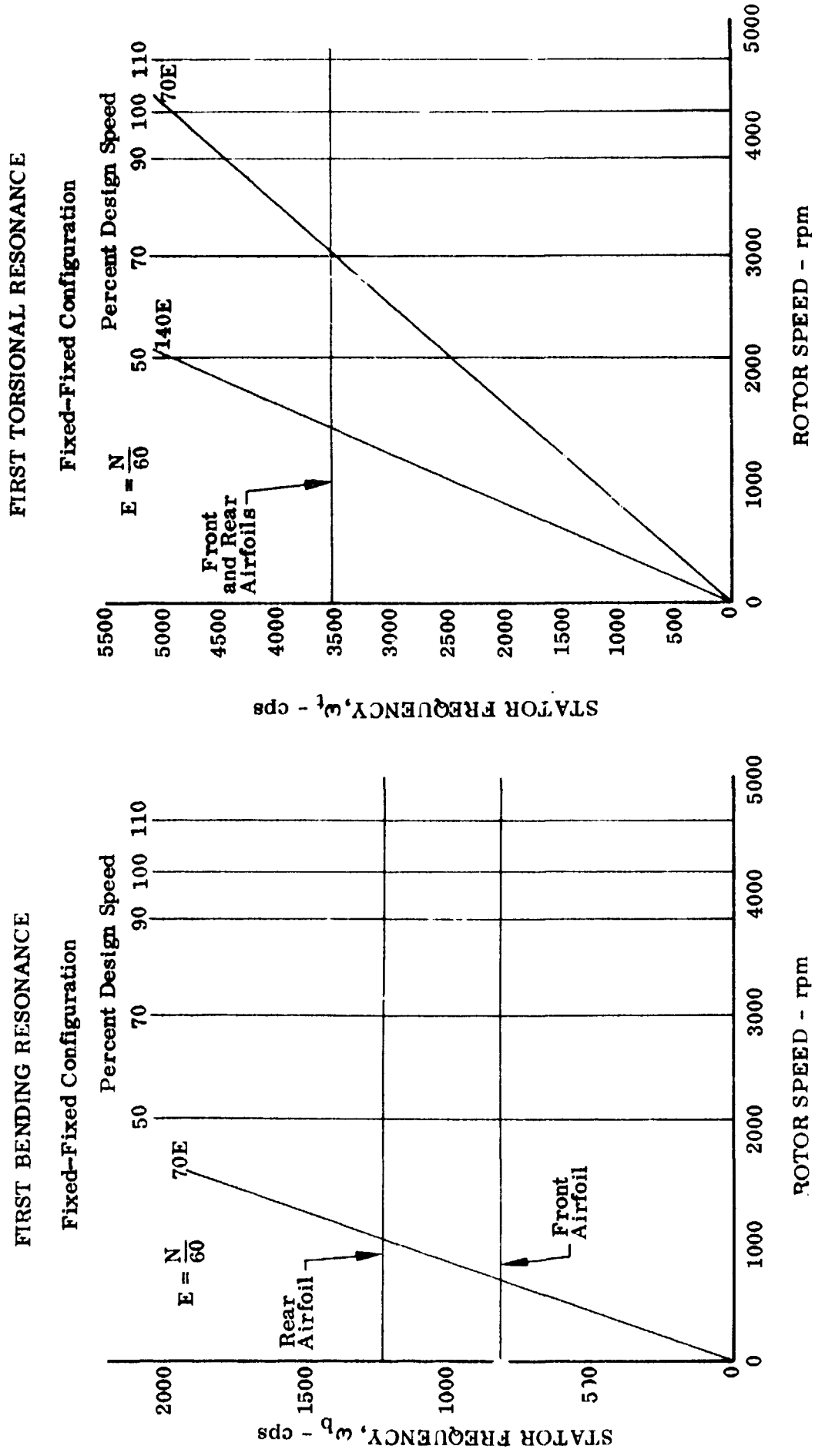


Figure 76. Stator B Resonance Diagram for First Bending and First Torsional Mode Vibration DF 90625

ASM 5613 - Stainless Steel 200°F

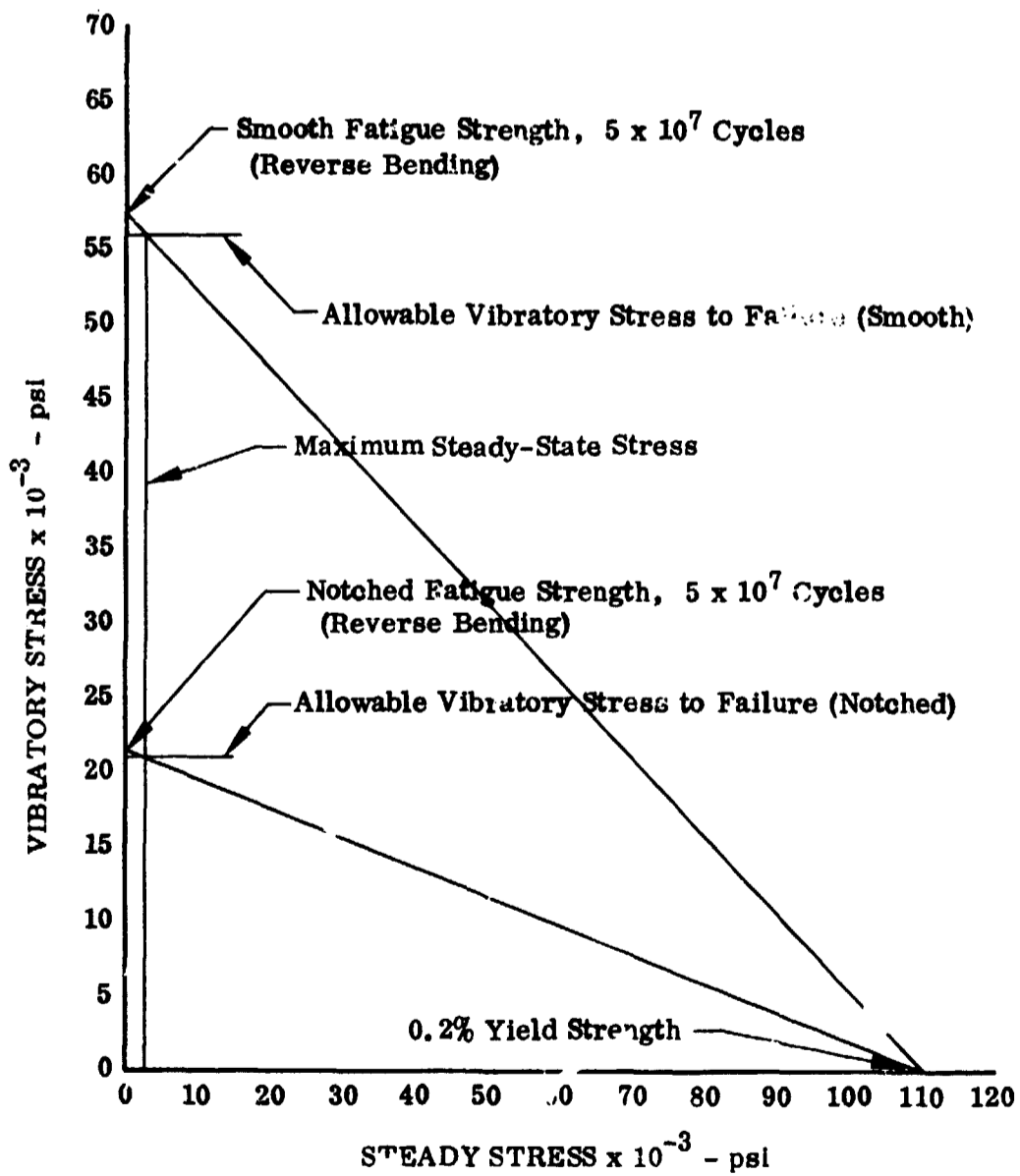


Figure 77. Stator A Goodman Diagram

DF 90626

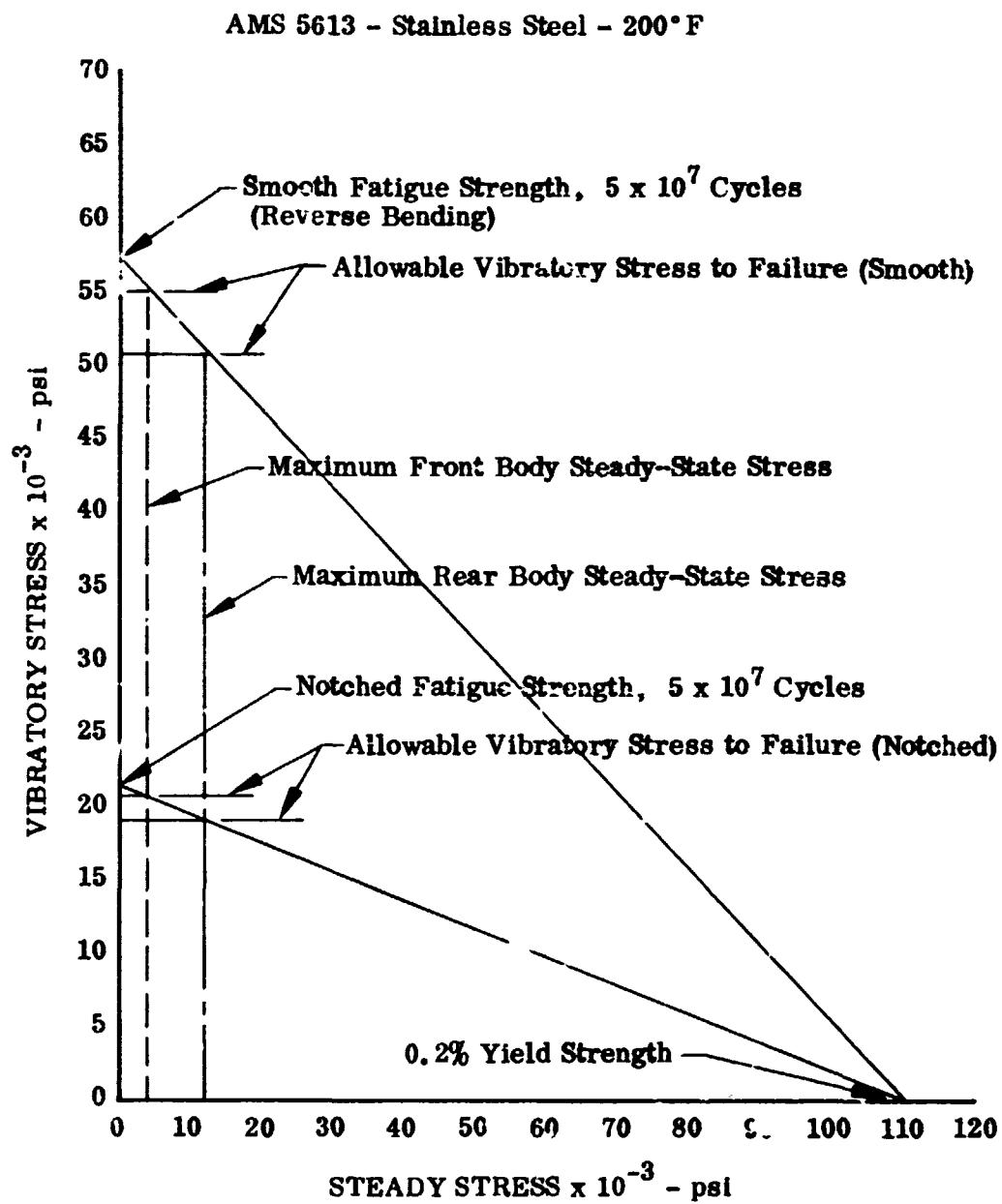


Figure 78. Static or B Goodman Diagram

DF 90627

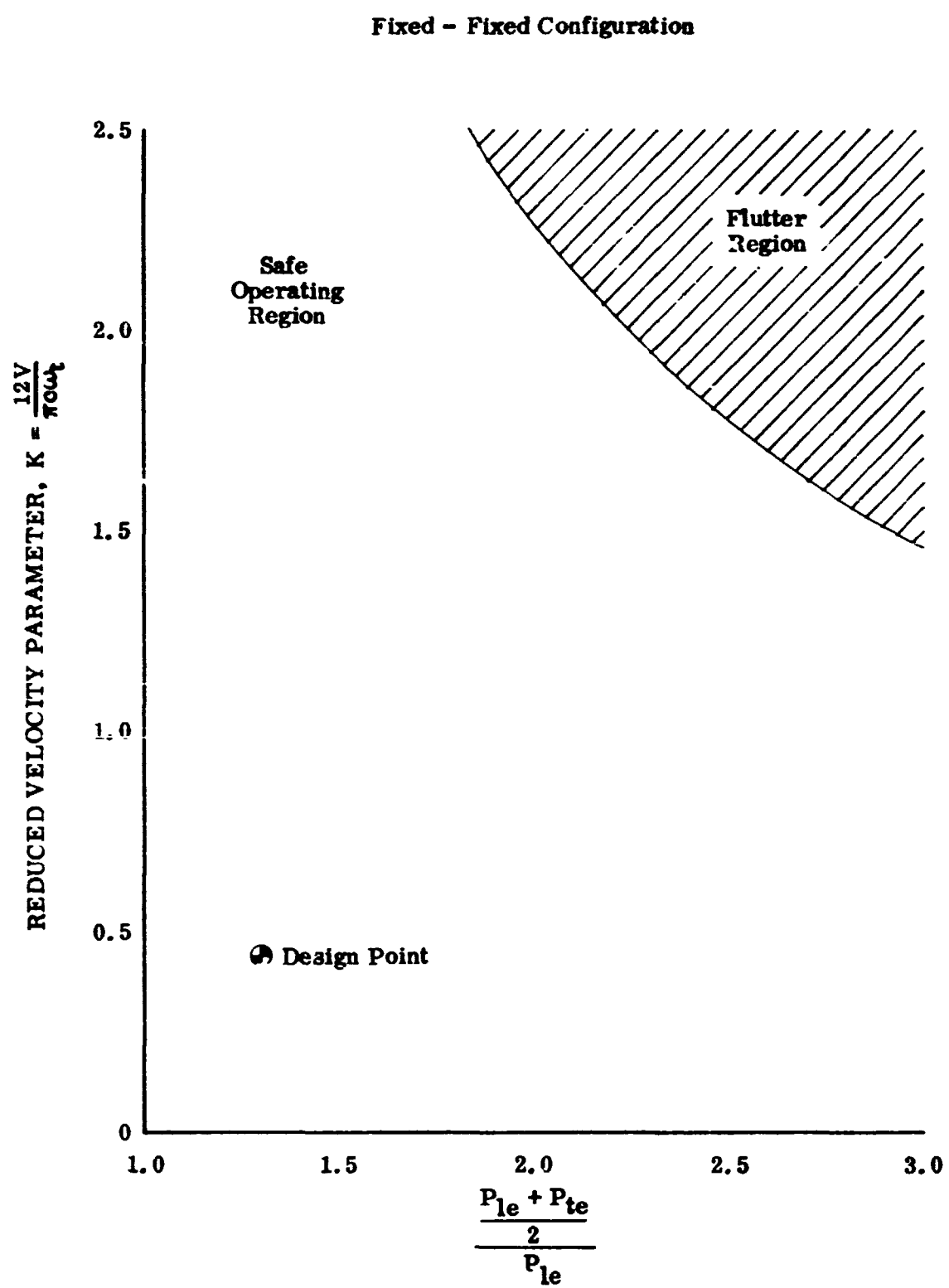


Figure 79. Calculated Stator A First Torsional Mode Flutter Characteristics DF 90623

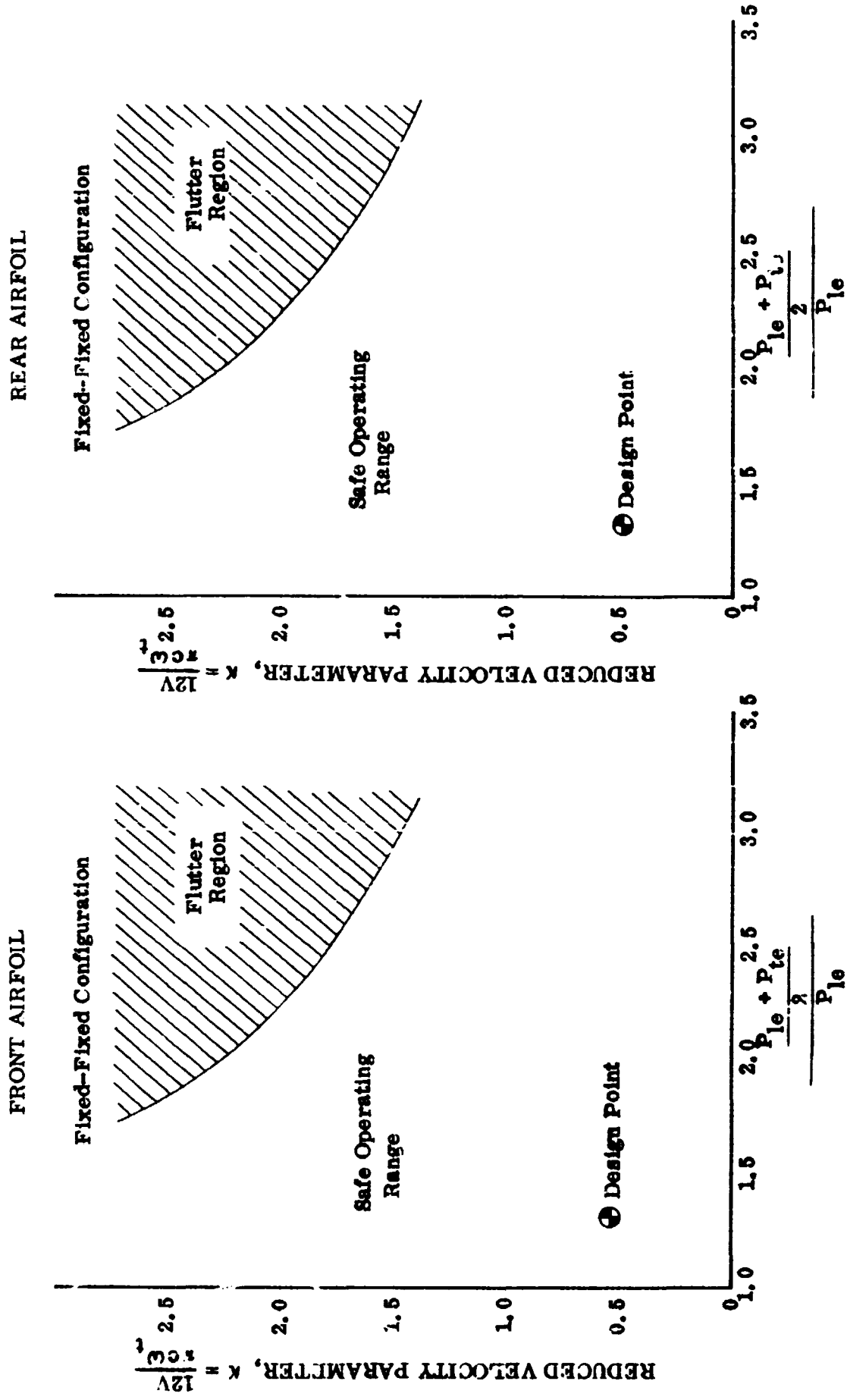


Figure 80. Calculated Stator B First Torsional Mode Flutter Characteristics

DF 90629

APPENDIX A
DEFINITION OF SYMBOLS AND DESIGN VARIABLES

Definition of Symbols

A_A	Flowpath annular area, ft ²
a_0	Inlet relative stagnation velocity of sound, ft/sec
c	Chord length, in.
C_p	Static pressure coefficient
d	Diameter, in.
D	Diffusion factor
E	Multiple of rotor frequency
F	Tandem airfoil passage convergence (See figure 25.)
$f(i_m)$	Incidence parameter
G	Tandem airfoil passage gap (t_e), in. (See figure 25.)
H	Tandem airfoil passage gap (l_e), in. (See figure 25.)
i_m	Incidence angle, deg
K	Reduced velocity parameter
K_T	Notch factor
L	Tandem airfoil passage overlap, in. (See figure 25.)
LC	Local correction for suction surface velocity (See figure 19.)
M	Mach number
N	Rotor speed, rpm
P	Total pressure, psia
PR	Pressure ratio
p	Static pressure, psia
S	Blade spacing, in.
t	Blade maximum thickness, in.
T	Total temperature, °R
U	Rotor speed, ft/sec

V	Velocity, ft/sec
W	Actual flowrate, lb _m /sec
α	Cone angle (angle of plane tangent to conic surface that approximates the design streamline of revolution), deg
β	Air angle, degrees from axial direction
$\Delta\beta$	Flow turning angle, deg
γ	Ratio of specific heats
γ°	Blade-chord angle, degrees from axial direction
δ	Ratio of total pressure to NASA standard sea level pressure of 14.694 psia
δ°	Deviation angle, deg
θ	Ratio of total temperature to NASA standard sea level temperature of 518.7°R
κ	Blade metal angle, degrees from axial direction
ρ	Density, lb _f -sec ² /ft ⁴
σ	Solidity
ϕ	Blade camber angle, deg
ω	Frequency, Hertz
$\bar{\omega}$	Loss coefficient
$\frac{\bar{\omega}\cos\beta te}{2\sigma}$	Loss parameter

Subscripts:

b	Bending
c	Combined or overall
cx	Overall axial
fs	Free stream value
id	Isentropic condition
le	Leading edge
L	Local

max	Maximum
ref	Minimum loss
te	Trailing edge
t	Torsional
z	Axial component
θ	Tangential component
1	Front airfoil of tandem blade or vane
2	Rear airfoil of tandem blade or vane

Superscripts:

'	Related to rotor blade
-	Mass average value

Definition of Design Variables

Incidence Angle:

$$\text{Rotor: } i_m = \beta'_{le} - \kappa_{le} \qquad \text{Stator: } i_m = \beta_{le} - \kappa_{le}$$

Diffusion Factor:

$$\text{Rotor: } D = 1 - \frac{V'_{te}}{V'_{le}} + \frac{d_{te} V_{\theta te} - d_{le} V_{\theta le}}{(d_{le} + d_{te}) \sigma V'_{le}}$$

$$\text{Stator: } D = 1 - \frac{V_{te}}{V_{le}} - \frac{d_{te} V_{\theta te} - d_{le} V_{\theta le}}{(d_{le} + d_{te}) \sigma V_{le}}$$

Deviation Angle:

$$\text{Rotor: } \delta^o = \beta'_{te} - \kappa_{te} \qquad \text{Stator: } \delta^o = \beta_{te} - \kappa_{te}$$

Loss Coefficient:

$$\text{Rotor: } \bar{\omega}' = \frac{(P'_{te})_{id} - P'_{te}}{\bar{P}'_{le} - P_{le}}$$

where:

$$(P'_{te})_{id} = P'_{le} \left\{ 1 + \frac{\gamma - 1}{2} \left(\frac{U_{te}^2}{a_{ole}^2} \right) \left[1 - \left(\frac{d_{le}}{d_{te}} \right)^2 \right] \right\}^{\frac{\gamma}{\gamma - 1}}$$

$$P' \text{ is found from } p/P' = \left[1 + \frac{\gamma - 1}{2} M'^2 \right]^{\frac{\gamma}{1 - \gamma}}$$

$$\text{Stator: } \omega = \frac{P_{fs} - P_{te}}{P_{fs} - P_{le}}$$

Static Pressure Coefficient:

$$C_p = \frac{P_L - P_{fs}}{1/2 \rho_{fs} V_{fs}^2}$$

Pressure Ratio:

$$\text{Rotor: } \frac{\bar{P}_{rotor te}}{\bar{P}_{rotor le}}$$

$$\text{Stage: } \frac{\bar{P}_{stator te}}{\bar{P}_{rotor le}}$$

Equivalent Flow:

$$\frac{W\sqrt{\theta}}{\delta}$$

Equivalent Rotor Speed:

$$N/\sqrt{\theta}$$

Adiabatic Efficiency:

$$\text{Rotor: } \frac{(PR)^{\frac{\gamma - 1}{\gamma}} - 1}{T_{te}/518.7 - 1}$$

$$\text{Stage: } \frac{(PR)^{\frac{\gamma - 1}{\gamma}} - 1}{T_{te}/518.7 - 1}$$

APPENDIX B
REFERENCES

1. Sheets, H. E., "The Slotted-Blade Axial-Flow Blower," Transactions of the ASME, November, 1956.
2. Linnemann, H., "Tandem Grid in a Single-Stage Axial Blower," Translated from Konstruktion by Redstone Scientific Information Center, No. 276, 21 September 1964.
3. "Single-Stage Experimental Evaluation of Compressor Blading With Slots and Wall Vortex Generators, Part III - Data and Performance for Stage 1," NASA CR-72741, 1970.
4. "Single-Stage Experimental Evaluation of Slotted Rotor and Stator Blading, Part III - Data and Performance for Slotted Rotor 1," NASA CR-54546, 1967.
5. "Single-Stage Experimental Evaluation of Slotted Rotor and Stator Blading, Part IV - Data and Performance for Slotted Rotor 2," NASA CR-54547, 1967.
6. "Single-Stage Experimental Evaluation of Slotted Rotor and Stator Blading, Part VI - Data and Performance for Slotted Stator 1 and Flow Generator Rotor," NASA CR-54549, 1967.
7. "Single-Stage Experimental Evaluation of Slotted Rotor and Stator Blading, Part VII - Data and Performance for Slotted Stator 2," NASA CR-54550, 1967.
8. "Single-Stage Experimental Evaluation of Variable Geometry Guide Vanes and Stator Blading, Part III - Data and Performance for Variable Camber Guide Vane and Stator A," NASA CR-54556, 1968.
9. "Single-Stage Experimental Evaluation of Variable Geometry Guide Vanes and Stator Blading, Part IV - Data and Performance for Variable Camber Guide Vane and Stator B," NASA CR-54557, 1968.
10. Miller, M. L. and T. E. Beck, "Single-Stage Experimental Evaluation of Boundary Layer Blowing Techniques for High Lift Stator Blades, Part II - Data and Performance of Flow Generator Rotor and Single Slotted 0.75 Hub Diffusion Factor Stator," NASA CR-54565, 1968.
11. "Aerodynamic Design of Axial Flow Compressors (Revised)," NASA SP-36, 1965.
12. Lieblein, S. "Loss and Stall Analysis of Compressor Cascades," Journal of Basic Engineering, September, 1969, pages 387-400.
13. Giesing, J. P., "Extension of the Douglas Newmann Program to Problems of Lifting Infinite Cascades (Revised)," Douglas Aircraft Report No. LB 21653, 2 July 1964.

14. Katsanis, Theodore and William D. McNally, "FORTRAN Program for Calculating Velocities on a Blade-to-Blade Stream Surface of a Tandem Blade Turbomachine," NASA TND-5044, 1969.
15. Sanger, N. L., "Analytical Study of the Effects of Geometric Changes on the Flow Characteristics of Tandem-Bladed Compressor Stators," NASA TND-6264, March 1971.
16. Raily, J. W., and M. E. El-Sarha, "Ackeret Method for the Design of Tandem Cascades," The Engineer, 25 June 1965, pages 1085-1089.